THREE DIMENSIONAL MAGNETOHYDRODYNAMIC TURBULENCE IN SOLAR CORONAL LOOPS

A Thesis Submitted to the

Bangalore University

for the Award of Degree of

DOCTOR OF PHILOSOPHY

in the Faculty of Science

BY

T.D. SREEDHARAN

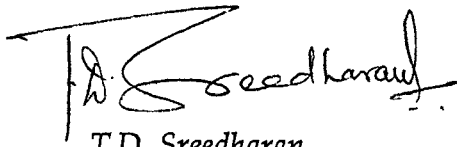Indian Institute of Astrophysics
Bangalore 560 034

Dedicated to

T.S.D. Chari
&
Lakshmi Ammal

My Parents

Certificate

Certified that the thesis submitted is a record of research work done by the candidate during the period of study under me and that it has not previously formed the basis for the award of any degree, diploma, associateship or fellowship.

T.D. Sreedharan
Candidate

Dr. Vinod Krishan
Guide
Professor
Indian Instiute of Astrophysics
Bangalore 560 034

Bangalore
Date: 1st May 1995

ACKNOWLEDGEMENT

CONTENTS

THE BEAUTY OF THE SUN !

A photograph of the sun taken during the eclipse of December 9,1929. The narrow ring of luminosity is the chromosphere. Prominences rise into the corona to heights of as much as 150,000 kilometers at several places on the limb. The striking feature at bottom is a loop prominence originating in a disturbed region of the sun containinga strong localized magnetic field. It shape traces lines of magnetic force that curve upward intothe corona and down again.

1 INTRODUCTION

1.1 THE SUN:

The sun formed 4.6 billion years ago, is nearly halfway through its life, and will not change its properties appreciably until it moves off the main sequence in five or six billion years to become a red giant. It is an ordinary body in the cosmic hierarchy, similar to countless other G2 stars on the main sequence in its general characteristics; but it has one unique feature: it is 300,000 times closer to earth than the next nearest star. This closeness of the sun gives it a considerable astrophysical importance. The sun also provides us with our only opportunity to take a close look at a stellar atmosphere.

1.2 THE SUN'S INTERIOR:

Theoretical studies of stars of one solar mass have been

1

carried out by many astrophysicists under a variety of assumptions, and agreement has been reached regarding the general conditions that exist in the interior of the sun. The temperature of the sun decreases from a central value of approximately 15 million degrees to a value of 5800 ^{o}K at the surface(Fig.1.1)and the outer regions, the corona is about million degrees hot!

The density within the sun falls off very sharply with increasing distance from the center (Fig.1.1). The central density is about 150 gm cm^{-3}, which is about 13 times the density of lead. As a result of the rapid fall off in the density of the sun, most of its mass is concentrated in a relatively small volume, approximately 90 percent of the sun's mass being contained in the inner half of its radius. The average density of the sun is 1.4 gm cm^{-3}.

1.3 THE ZONE OF CONVECTION:

In the deep interior of the sun the temperature rises up to many millions of degrees. ·In this range of temperatures, the collisions between atoms are sufficiently violent to eject many electrons from their orbits. Light atoms are completely ionized,
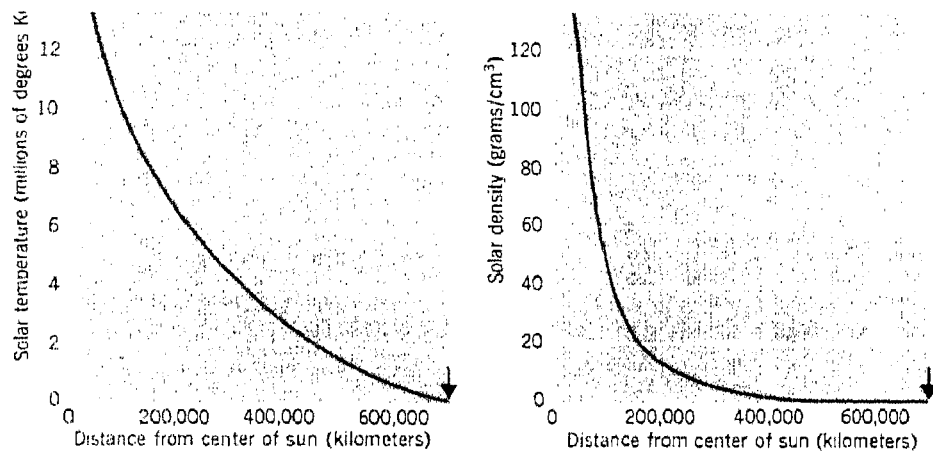
Fig.1.1. Temperature and density at various depths in the Sun's interior. The arrow indicates the surface.

3

while the heavy atoms loose their outer electrons, retaining the tightly bound inner electrons. These cannot be easily dislodged by absorption of a photon. Consequently photons pass readily through the inner part of the sun. Close to the surface of the sun the temperature falls, and the heavier atoms recapture their outer electrons. Such atoms below the sun surface tend to block the flow of photons coming from the interior. If photons are the only means of carrying energy up to the surface of the sun, the blocking of these photons will cause the temperature to drop sharply at some depth below the surface. Thus, layer of relatively cool gas is formed on the hotter interior and a convection zone is set up.

At depths greater than 1,50,000kilometers, energy is transported within the sun by radiation (i.e., by flow of photons). At this height the outward flow of radiant energy is blocked to a great degree by absorption of photons, and convection sets in. From that depth out to the surface, energy is transported partly by convection and partly by radiation. Above the surface, radiation again becomes the sole means of energy transport.

1.4 THE PHOTOSPHERE:

The visible surface of the sun is called the photosphere.

4

It is the sun's disk as observed visually or with a telescope. It has a uniform appearance when viewed with the eye or through a small telescope, but through a larger telescope and under good observation conditions it reveals a granulated texture. The effective temperature of the photosphere is estimated to be about 6000^0K.

1.5 THE SOLAR ATMOSPHERE:

The region of tenuous and essentially transparent solar gas lying above the photosphere is called the **solar atmosphere**. The outer boundary of the solar atmosphere is not clearly defined. The atmosphere extends out to a distance of 5 million kilometers from the sun, if its limit is considered to be a point at which the density of the solar gas has decreased to the density of the gas in the space between the planets.

The solar atmosphere is divided into two regions called the 'Chromosphere' and the 'Corona'. Both regions are invisible under ordinary conditions because their faint luminosity is masked by photospheric light that has been scattered in the earth's atmosphere or in the telescope itself. From 6000^0K at the

photosphere the temperature, falls to a minimum of approximately 4000^{0}K, and stays at this value approximately up to 2000 kilometers. This thin region is called the 'Chromosphere'. Above that height the temperature begins to rise very steeply, reaching the million degree level at an altitude of about 5000 kilometers and remaining at that level throughout the inner corona(Fig.1.2). At the high temperature that prevail in the upper chromosphere all the hydrogen and helium atoms are ionized, and the 6563A^0 line and other emission lines of neutral hydrogen and helium disappear. Elements heavier than H and He also loose several electrons at this temperature, although they are not completely ionized. Thus, the lines of all these elements, which are prominent in the spectrum in the lower chromosphere disappear gradually as the altitude increases and are entirely missing from the spectrum of corona.

1.6 THE CORONA:

The chromosphere consists of countless gas jets called spicules which rise to a height of about 5000 kilometers. This altitude can be referred to as the upper boundary of the chromosphere. Surrounding the chromosphere is the corona. Under ordinary circumstances the flow of light from the photosphere

6
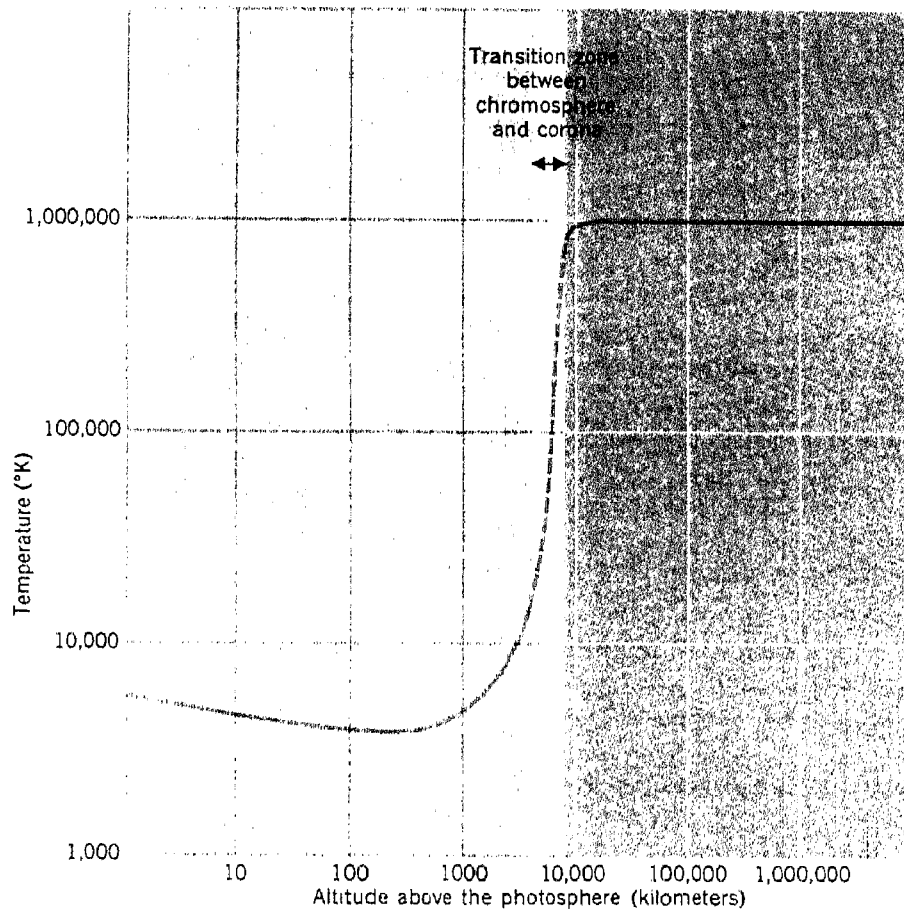
Fig.1.2 Temperatures in the chromosphere. The transition zone is highly variable and inhomogeneous, with spicules and interspicular matter.

overwhelms the very weak emission from the higher layers of the atmosphere which therefore remain hidden from the direct view. At the time of solar eclipse, however, the moon passes in front of the sun and blocks out the light from the photosphere. When the disk of the moon completely masks the solar disk a white halo (Fig.1.3)of tenuous gas appears beyond the edge of the moon, stretching a vast distance out into space. This is termed as Corona.

As seen during an eclipse, the visible corona extends out from the edge of the solar disk many millions of kilometers. When viewed from the ground, the luminosity of the corona fades into the background of scattered light from the sky at a distance of roughly 10 million Kilometers from the sun. But the photographs taken from a balloon at high altitudes, where the sky is darker, show a visible corona out to 30 solar radii. Other measurements made from satellites and space probes suggest that the corona has no outer boundary. A stream of wind called the solar wind flows out of the corona and into the solar system at all times, continuously immersing the earth and the planets in the tenuous gases of the solar atmosphere.

The morphology of the corona undergoes dramatic changes during the course of solar cycle but similar basic elements can be
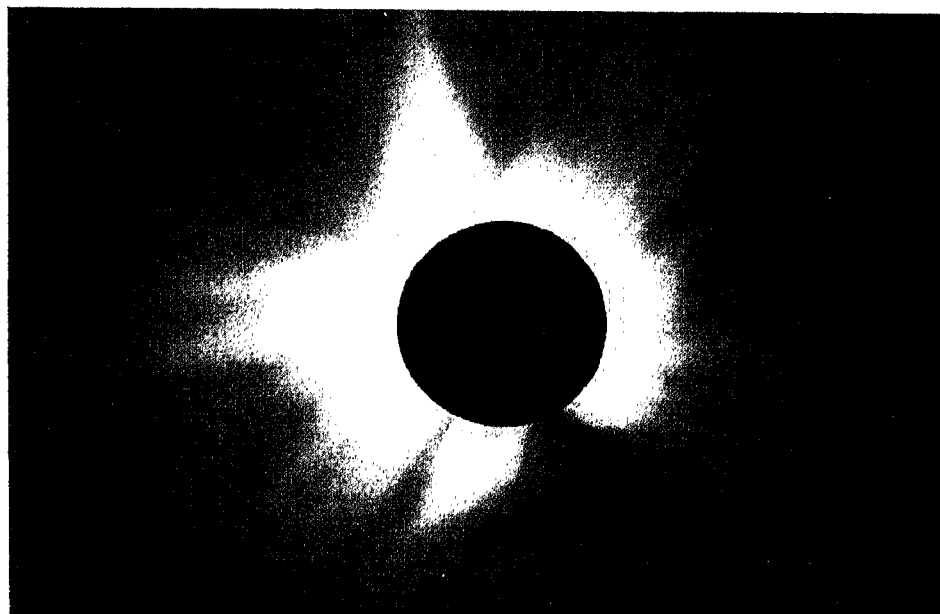
Fig.1.3 The Solar corona 30 seconds after the start of totality during the eclipse of March, 1970. Features are visible at a distance of 4.5 solar radii or 3 million kilometers.

distinguished throughout. The most distinctive coronal features are the radial plumes generally appearing in polar regions, and the low, bright, domed structure called condensations. Above the condensation the dome is often pulled out into a ray or into a set of rays, which are longer lived than the polar plumes and are known as streamers. Coronal material flows outward along the streamers into the wind.

The magnetic field in the solar corona where the magnetic forces greatly outweigh the thermal forces, is assumed to be relatively uniform.. The solar corona is highly structured. Well. away from the active regions are formed more or less radial rays. These occur over extended regions of the sun where the field in the underlying photosphere is scattered and predominantly unipolar. These regions are called coronal holes and are found usually at the solar poles. Over the rest of the solar surface, the basic structural component of the solar corona is the coronal loop. Some loops are vast features linking different active regions. These typically have temperatures 2-3 x 10^6 K and density of about 10^{-12}Kg m^{-3}. Loops of similar scale but somewhat lower temperatures arch across quiet regions and presumably link the dispersed fragments of active regions. The corona above active regions themselves is characterised by coronal condensations,which is now thought to represent the collective effect of a complex loop

system linking areas of opposite polarity. The properties, physical conditions existing in the loops, the morphology of the cool loops, hot loops and flare loops are discussed in chapter 2.

Little can be said about the most important physical quantity of the corona, the magnetic field. The field strength as inferred from the observations of radio waves emitted by hot coronal gas suggests a value of 30 mT at an height of 15000 kilometer dropping to 1mT - 0.3mt at 70000 Kilometer. However these values are subject to a considerable uncertainty. Th(alignment of the fine structures of corona indicates the direction of the field, i.e., loops trace the magnetic field linking regions of opposite polarity whilst coronal rays delineate 'open'field lines which stretch outward from the corona and close in the interplanetary medium. Coronal magnetic field models and model equations for coronal plasma are discussed in Chapter 3.

1.7 PRESSURE STRUCTURE IN SOLAR CORONAL LOOPS:

The loop or arch like configurations of the solar active regions have been seen in the emissions at UV, EUV and X-ray wavelengths (Foukal, 1978). The current carrying plasma in the loop

supports a helical form of magnetic fluid.

Typically, magnetohydrodynamic stability theory has been perturbation theoretic, proceeding from linearized equations of motion around quiescent (velocity V=0)equilibria. One either follows the evolution of small perturbations or attempts to find exponentially growing normal modes by variational methods (the energy principle). Some advantages of linear stability analysis are (i) the knowledge of growth rates of instabilities and (2) insight into the nature of whatever growing modes may exist. Some disadvantages are (1) the difficulty of treating realistic spatial profiles, and an almost infinite variety of these profiles. One can keep on calculating stability by changing the profile, and (2) the impossibility of determining the effects of instabilities once they have outgrown the linear regime.

The turbulence literature emphasizes the important role of the quadratic integral invariants of the nondissipative, ideal magnetohydrodynamic model: total energy, magnetic helicity and cross helicity. Because the value of these invariants cannot be directly modified by nonlinear effects, their wave number spectra give valuable information about the state and dynamics of the turbulent magneto fluid.

12

In the statistical theory of MHD turbulence, from scalar numbers, the average total energy, the average magnetic helicity and the toroidal and poloidal magnetic fluxes suffice to determine the level of excitation of every mode in the system for an initially quiescent system. The quiescent limit is one in which all of the excitation is locked into the extremal helicity state by the simultaneous constancy of the magnetic helicity and total energy. It is the state of minimum energy for given magnetic helicity. It is a single Chandrasekhar-Kendall mode and so is a force- free state, (Montgomery et. al,1978).

The steady state pressure structure of a solar coronal loop can be studied using the theory of MHD turbulence in cylindrical geometry. The magnetic and velocity fields are expanded in terms of Chndrasekhar-Kendall functions using the MHD equations, the pressure profile is then calculated as a function of the velocity and magnetic fields. The radial and axial variations of the pressure in a constant density loop are calculated. These variations are found to conform to the observed features of cool core and hot sheath of the loops as well as to the location of the temperature maximum at the apex of the loop. It is found that these features are not present uniformly all along either the length of the loop or across the radius. The possible oscillatory nature of these pressure variations and the associated time periods

13

have been explored.

In order to study the temporal behavior of the fields and the pressure one has to put in the dynamics, which is described by a set of infinite, coupled, nonlinear ordinary differential equations which are first order in time for the expansion coefficients of the velocity and magnetic field. Since obtaining the full solution of these equations is a formidable task, we plan to represent the loop behavior by a superposition of the three lowest order C-K functions. One justification for doing so is that these functions represent the largest spatial scales and therefore they may be the most suitable states for comparison with the observed phenomena. This system reduces to a set of six equations, three for velocity and three for magnetic field. Numerical methods will be needed to solve these equations. However analytical progress can be made in two simplified cases:

(i) When the system is disturbed linearly from its state of equilibrium and

(ii) when one of the three modes has an amplitude much larger than the other two, known as the Pump approximation.

Preliminary work indicates that the three mode system exhibits sinusoidal oscillations when perturbed linearly. This work is to be perused in more detail, checking the response of the

14

system under different initial conditions. This will help us to determine the temperature, the velocity field and the magnetic field in the loop plasma of constant density. The knowledge of these parameters and their variation with space and time enables the explanation of varying emission in other electromagnetic bands at which the loop plasma emits. The description of small scale variations in terms of the global invariants of the MHD system gives a very important handle on the dynamics of plasma. The transformation of linear to nonlinearity needs to be studied. The spatial evolution of three dimensional solar coronal loops is dicussed in Chapter 4 and temporal evolution in Chapter 5.

The fluid theory description of a plasma is sufficiently accurate to describe the majority of the observed phenomena. However, there are some phenomena for which the fluid treatment is in adequate. For such cases we need to consider the velocity distribution function $f(v)$ for each species. This treatment is called Kinetic theory. The Vlasov description admits the investigation of kinetic process like heating and radiation, and unlike a fluid description it does not require an equation of state to determine the individual variations of temperature and density. A Vlasov-Maxwell description of the ubiquitous solar coronal structures is discussed in Chapter 6.

Future work shall include four-mode interacting system. One could then generalize to the case of many modes with initial amplitudes chosen to fit Kolmogoroff spectrum. Finally it is hoped that it will be possible to compare the theoretical studies with the observations on coronal loops. A knowledge of ordinary and partial differential equations, numerical methods to solve them and basics of magnetohydrodynamics are required to pursue these objectives. Suitable programs have to be developed to solve the multi mode equations.

2 SOLAR CORONAL LOOPS

2.1 INTRODUCTION:

Visual observations of prominences were the first to reveal the existence of well defined loop structures arching upwards from the surface of the sun high into the overlying corona. Regular visual observation of prominences obtained during total eclipses of the sun have revealed more information about the coronal loops. Young and Seechi have concluded from a number of observations that prominences could be classified into two main types, 'quiescent' and 'active'. They are also called as 'cloud' and 'flame' prominences respectively. An active prominence is what is referred to as a loop prominence. They assumed the shapes to be parabolic, since they supposed that the material was ejected from the surface and was then subjected to purely gravitational forces. The true shapes of the loops have however been known only recently.

With the invention of spectroheliograph, spectrohelioscope birefringent filter, observations were obtained in H and K lines of

17

the singly ionized calcium and latter in the H_α line of hydrogen. These observations reveal structures in the chromospheric region which are termed as 'cool' loops. The temperature of the loop plasma in this region is in the range of 20,000 to 10^6K while plasma loops with temperature greater than 10^6 are termed as 'hot loops'. Based on the film of the corona taken in the λ 5303A^0 line Dun (1971) arrived at this general conclusion: 'some coronal' scenes look "open"...and some look to be all loops and arches or "closed". The differences are presumed to be due to the magnetic field structure. The coronal structures are related to the magnetic field i.e., they are said to map the magnetic field. This is in contradiction with the force free calculations according to which the field should uniformly permeate the entire area and not merely lie in the loops. It is therefore apt to say that the corona defines particular flux tubes. The arches and loops can be considered as very basic coronal structures, since many scenes appear to contain nothing else. Satellite observations in the Extreme ultraviolet (EUV) and X-ray region of the spectrum provide a wealth of information on the loop structure of the corna. Though there has been substantial achievements from the ground based observations in the visible coronal lines, there has been very little scope for further elucidating the structure of the active corona. The overwhelming brightness of the photosphere at these wavelengths makes it impossible to observe the corona against the

18

solar disk. It is reasonably assumed that the observations in the

EUV and X-ray regions could reveal the structure of the low corona

of the disk as well at the limb, because in this region the

contribution of the photospheric layer virtually vanishes and the

radiation comes from the overlying material at the chromospheric

and coronal temperatures. This region of the spectrum has a number

of strong resonance lines emitted by many of the abundant ions of

various elements in various stages of ionisation which are formed

in the temperature range of 10^4 to 10^7K. The soft x-ray region

below 10nm is dominated by emission lines of very highly ionised

stages of a number of elements superimposed over a weak continuum

of coronal origin.

2.2 COOL CORONAL LOOPS:

Coronal loops are a phenomenon of active regions and they

are believed to be dominant structures in the higher levels of

(inner corona) the sun's atmosphere. As already mentioned, loop

plasmas which are in the range of 20,000 to 10^6K are referred to as

'cool loops'. Some properties and physical conditions in cool loops

based on the observations in H_α and other visible and near visible

lines, as well as in the EUV region are mentioned briefly for

19

better understanding.

Limb observations in the H_α has established that the individual loops were anchored to underlying sunspots, though this aspect is brought out well in disk observations. Figure **2.1** is an example of an active region loop system in which most or all of the loops are anchored to sunspots (Bumba and Kleczek;1961). Other photographs of interest of the active region loops are of Lategan and Jarrett(1982,Fig2a) and Foukal (1978,Fig2). The number of loops in a single system may range from just one up to perhaps ten or so, an upper limit is hard to establish from limb observations. Though various observers have given projected height to the loop, true heights cannot be determined from the limb observations unless the loop geometry is known.

Generally three types of motion are associated with active region loops (1) flow down both legs starting at the top of the loop (Kleczek; 1963) (2) a flow up one leg and down the other (Martin; 1973) and (3) a mainly horizontal back and forth motion of the whole loop (oscillations) (Vrsnak;1984). Two methods are generally adopted to measure the velocity and acceleration of the material observed at the limb. The first method is to determine the Doppler shift of a suitable line like H_α which will give the line of sight velocity and can be converted into true velocity
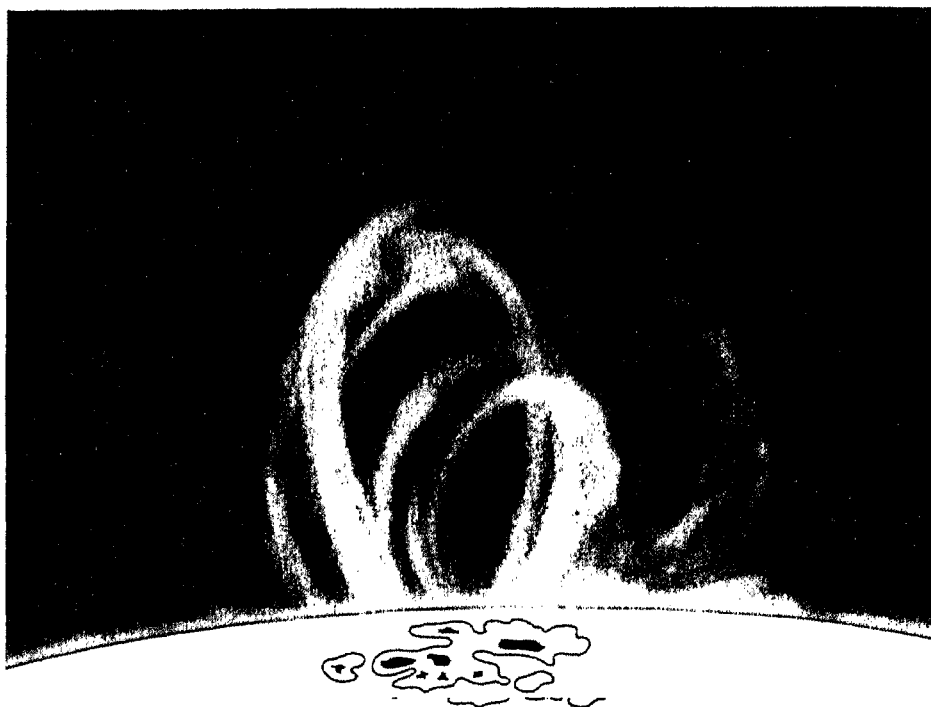
Fig.2.1 H_α active region loop system (Bumba & Kleczek, 1961). Most or all of the loops are anchored to sunspots whose locations were established with the aid of auxiliary data.

along the loop if a suitable geometry is assumed. The second method is to measure the projected motion in the plane of the sky using condensations or knots which are prominent features of the loop photographs. The true velocity is determined from the geometry of the loop, with the assumption that the apparent motions of the knots represent the genuine motion of the loop material and not changing conditions of excitation. Measurements of the velocities of the loops observed on the disk vary from 20 - 150 Kms^{-1}. The acceleration measurements both in the limb and disk observations reveal that accelerating and decelerating forces other than the gravity operate on the material in the loops.

2.3 MAGNETIC FIELD IN CORONAL LOOPS:

A measure of the magnetic field of prominences has been most difficult. However a number of concordant results have been obtained using Zeeman or Hanle effect. Athay et al (1983),measured the linear polarization in two resolved components of the He I D_3 line and obtained complete Stoke's profiles for thirteen prominences, mostly quiescent ones. They used the Hanle effect to interpret the results, obtaining the vector magnetic field at a number of locations. From the observations and analysis, they found

that one of the prominences (prominence N)had two arches extending

down from the main body to the chromosphere. In this prominence,

the total field B in the loop ranged from 4 to 46 Gauss. Since the

polarization depends on the scattering angle, the Hanle method is

found to be sensitive to the assumed geometry of the prominence. The

Zeeman method has been more widely used than the Hanle method even

though it yields only the longitudinal component of the field $B_{\parallel}$.

Vrsnak(1984) has estimated the total field B in H_α loop, by

measuring its bodily oscillations (mainly horizontal)in the plane

of the sky. He found the period to be 8 minutes. Assuming that the

motion was controlled by the magnetic field he showed that the

observed period was consistent with a value of B = 45 Gauss.

2.4 DISK OBSERVATIONS OF CORONAL LOOPS:

On the disk, an active region loop appears in the H_α line

as thin, curved dark feature linking a sun spot with another spot or

area of opposite magnetic polarity. Observations of H_α active

region loops on the disk indicate that loops occur only during the

most active stages of complex groups (Ellison; 1944). Though loops

and small flares tend to occur in active regions at times of high

activity, it does not imply a direct association between a

23

particular loop and a particular small flare. H_α loops terminate in or near sunspots at one or both ends(Ellison; 1944, Tandberg-Hanssen; 1974, Bray and Loughheed; 1983) Two types of flow are observed: (1) a unidirectional flow along the axis of a loop i.e.,ascent in one leg and a descent in the other; according to Ellison, the direction of the flow is independent of the magnetic polarities of the spot(s)involved; this type of flow is a commonly observed characteristic of loops in new and complex active regions: (2) a down flow from the top towards both foot points. The appearance of single or double loops is quite common while, the appearance of a complex loop is rare.

The motion along a loop may continue up to several hours (Ellison,1944)which is roughly the same interval over which loop systems are observed to persist. However, Tandberg-Hanssen (1977) give 15 minutes as a representative figure for the life time of a single loop, while Martin (1973), has shown evolutionary changes in a long lived loop over a period of one hour.

The diameter of the cross section of a loop, i.e., its thickness,is typically only a few seconds of arc and may be much smaller (Loughhead and Bray; 1984). If the cross section is circular, measurements of loop thickness are carried out on the (projected) image of loop recorded on a high resolution filtergram.

The thickness varies from 930 to 2100 Km (Loughhead,Bray and wang 1985).

Measurements of velocities and acceleration indicate that ascending material in the loop is subject to a force which accelerates it to highly supersonic velocities,while the descending material suffers a retarding force.

2.5 OBSERVATIONS OF CORONAL LOOPS IN EUV LINES:

Below $1500A^{0}$, up to about $100A^{0}$, the spectral region is called EUV. In this region, the contribution of the photospheric layers to the solar spectrum vanishes and the radiation comes from the overlying material at chromospheric or coronal temperatures. The solar EUV spectrum is dominated by emission from resonance lines of H I, He I,and He II, of intermediate stages of ionization of C,N,O,Si and S of highly ionised stages of Si,Ne,Mg and Fe. It is also characterized by the Lymann continuum and He I and He II continua. Under the conditions of formation normally assumed to apply, the intensity of any given line is a sensitive function of the electron temperature T_e peaking at some particular value $\bar{T}_e$ (referred to as formation temperature) and falling of sharply on

either side.

The observation of warmer lines than He II reveal the full three dimensional structure of the active regions. An active region is seen to consist of a complex system of bright loops arching between areas of opposite magnetic polarity. Photographs of active regions near the limb help identify these structures as loops in the geometrical sense. The individual loops are oriented in many different directions and frequently overlap one another. The clarity and sharpness with which a loop is seen depend both on the temperature of the line used in the observation and on the spatial resolution achieved.

Foukal(1976), after a thorough analysis of EUV emissions over 22 large sunspots, found that the emission is often brighter there than elsewhere in the active region (Brueckner and Bartoe, 1974; Sheely et al., 1975 and Dere, 1982). However, the intensity and distribution of radiation above the spots change markedly with time and as a consequence a large umbra can remain invisible in the cool EUV for as long as several days. Figure 2.2 is an illustration of the three dimensional structure of active regions seen in the EUV. This is a photograph of McMath region 12628 at the west limb taken in the line O VI λ 1032 A^0 ($\bar{T}_e$ = 3.2 10^5K). From the photographs, it is evident that the region is composed
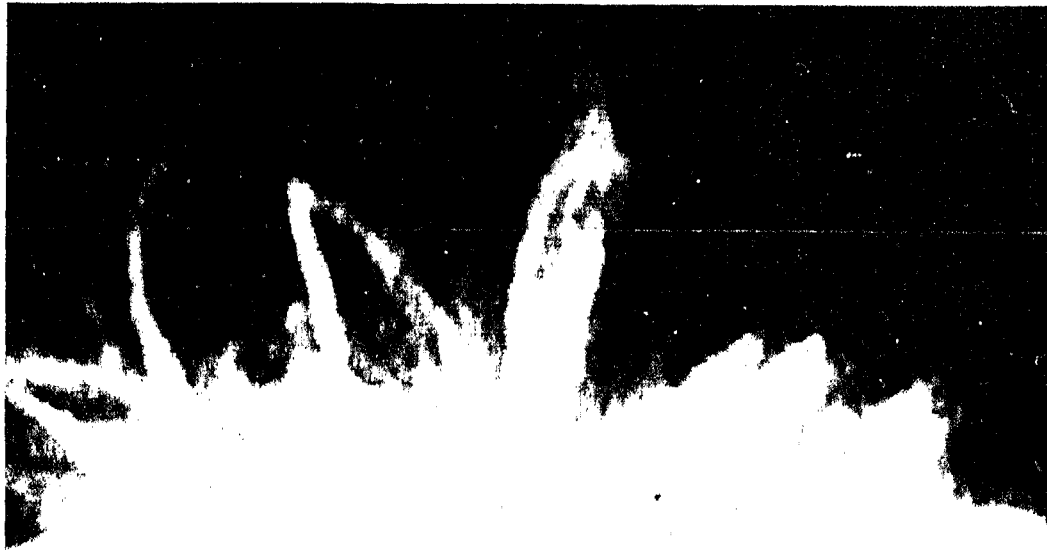
Fig.2.2 A photograph of McMath region 12628 at the west limb taken in the line O VI λ1032. The region consists basically of a number of separate loops lying in planes inclined at widely differing angles to the Solar vertical.

basically of a large number of separate loops lying in planes inclined at widely varying angles to the solar vertical. Some loops are nearly vertical, while others are almost horizontal.

2.6 PROPERTIES CORONAL LOOPS:

Due to an inadequate spatial resolution of the available EUV observation and paucity of systematic analysis of these data, little information is available about the morphological and dynamical properties of individual loops, yet the following properties can be associated.

Like all other solar features; cool EUV loops are always observed in projection of the plane of the solar disk or of the sky beyond. Limb observations indicate that most loops are essentially planar. The inclination of the planes containing the loop may vary from nearly vertical to nearly horizontal. The estimates of the heights attained by well defined loop prominence are typically of the order of tens of thousands of kilometers. Cheng(1980),has given a value ranging from 57,000 Km in Ne VII to 67,000 Km in Mg IX indicating increase of loop height with temperature. The width of

28

the cool EUV loops increase only slowly with height, Foukal (1976); Cheng (1980). On the other hand, loop width increases with temperature. The foot points of cool EUV loops are observed to be generally located on the peripheries of the two areas of opposite magnetic polarities in a bipolar active region as shown in figure 2.3. (Sheely, 1980). Loops observed in cool EUV lines, beyond the limb, show a strong contrast with respect to their surroundings. The intensity of the background emission is weak but increases with temperature. Loops observed in cool lines evolve appreciably in just a few hours (Levine and Withbroe; 1977, Cheng et al 1980). Spot associated loops are found to be more stable than other cool EUV loops (Foukal; 1976 has published photographs of a large spot loop near the limb whose basic form remained relatively unchanged over a period of 27 hours.) The pattern of flow is analogous to that observed in the H_α active region loop.

2.7 SPATIAL RELATIONSHIP BETWEEN LOOPS SEEN IN DIFFERENT LINES:

Though an inspection of the EUV spectroheliogram gives the idea that the same coronal loops in lines of widely dissimilar formation temperature are seen, Foukal (1975) has concluded that these loops are coincident and has hypothesized that a loop

Ne VII 465   100 000 km   Mg IX 368

Magnetogram   Nov. 28, '73   14:50   Fe XV 284
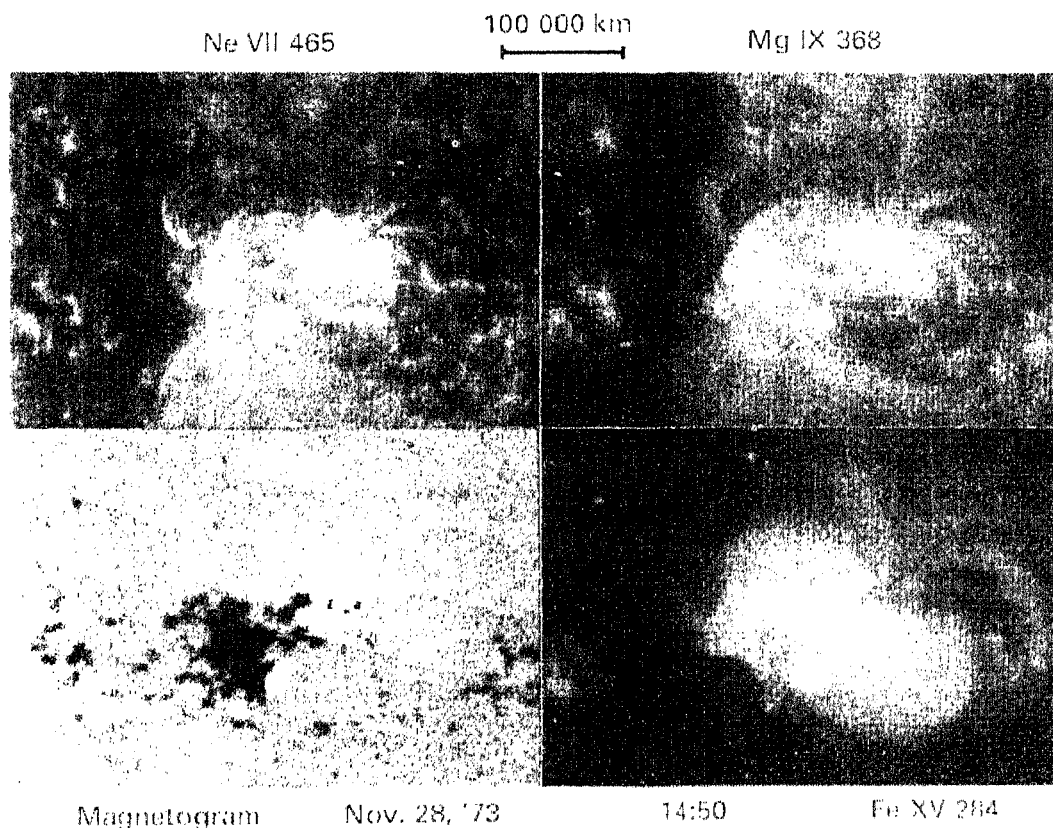
Fig.2.3 Bipolar active region on the disk observed almost
simultaneously in the two cool EUV lines Ne VII
$\lambda465A^O$ and Mg IX $\lambda368A^O$, as well as in in the hot
EUV line Fe XV $\lambda284A^O$ (Sheely, 1980). White and black
patches on the kitt Peak Magnetogram delineate
areas of positive and negative polarity respectively
in the underlying photospheric magnetic field.
The elongated bright features radiating outwards
from the central areas of bright emission represent
the lower ends of coronal loops.

consists of a cool core surrounded by a concentric sheath each one filled with material hotter than that in the adjacent inner sheath. This does not describe the relation between cool and hot EUV loops. They are not known to be coincident.

2.8 PHYSICAL CONDITIONS IN COOL LOOPS:

Loughhead, Bray and Wang (1985) have given a complete description of the physical conditions in a loop observed on the disk in H_α. From observations, it is possible to determine the electron temperature T_e and electron density N_e, the gas mass density ρ and pressure P, the Mach number M if the axial flow speed along the loop V_0 is known.

The observations reveal a striking variation in density: there is distinct compression near the top of the loop and rarefactions in both the ascending and descending legs. The variations in the pressure is even more marked. If these variations point to the evidence for the presence of a wave in the loop, then, the wavelength will roughly be equal to one half of the length of the loop. The variations in ρ, P, T_e and V_0 plotted against the distance along the loop indicates the presence of node

31

at the highest point of the loop. These conditions in the loop inferred from EUV data are in very good agreement with observation in visible and near visible regions.

Roussel-Dupre et al(1984) on the basis of their results concluded that the EUV emission from the loop originates in very thin sheaths of materials surrounding an(assumed) cool core. Each sheath is isolated from the others by the magnetic field in the loop and radiates at the temperature giving the maximum abundance of the particular ion involved. The observations in the cool loops both in the visible and EUV regions indicate that the electron density extends over a wide range of several orders of magnitude while the gas pressure is restricted to a much smaller range (single order of magnitude). This indicates that the stability of a loop, whatever its temperature depends on the maintenance of approximate pressure equilibrium with the surrounding coronal medium. Further it is evident that all cool loops appear to have similar properties with exception of temperature and can be regarded as manifestations of the same basic physical structure.

2.9 PHYSICAL CONDITIONS IN HOT LOOPS:

Observations made in the visible and EUV lines provide

extensive information on the large scale systems of loops which dominate the structure of the lower corona above the active regions. These lops are assumed to trace out closed magnetic field lines which emerge from beneath the photosphere and expand to fill the whole coronal volume above an active region. Though the loop system gives some insight into the three dimensional configuration of the magnetic field ; the picture is not complete. Hence, observations of hot loops which are filled with material at coronal temperature of a million degrees or more, seem to be more pertinent.

Loops observed in the visible region of the spectrum have generally been observed in the FeXIV $\lambda5303A^0$ line. The following is the summary of the properties associated with the active region loops from the descriptions of Kleczek(1963) and Dunn(1971).These refer to both flare and non-flare loops.

2.10 PROPERTIES OF HOT LOOPS:

Loops in λ 5303A^0 region occur as systems of loops in a single active region, with typical heights of up to 50,000 - 100,000 Km. Larger loops may connect two active regions and the

system appears to be rooted in the sunspot groups or in plage areas. The larger loops are generally more uniform in intensity along their widths and lengths and smaller loops are less uniform. Loops are more active when they are small, they tend to grow in *situ*, then fade, and others grow at higher elevation. Larger loops are very stable. Loops are found to be planar structures. The smaller loops last for hours while larger loops last for days. The high temperature EUV emission from the sun is confined very largely to the active regions and the loops emanating from them. Individual hot EUV loops are distinguished by their broad and irregular and less loop like appearance as compared to those visible in the cool EUV loops. Unlike cool EUV loops the hot loops are never observed to brighten progressively along their length but appear to brighten and fade in *situ*. All hot loops appear to be basically similar in their properties regardless of the wavelength region in which they are observed. All loops extending outwards from an active region necessarily return to the same vicinity. The spectrum of the core is harder than that of the rest of the active region, implying, that, if the emission is thermal in origin, the core is hotter. The X-ray loops associated with an active region are similar in general appearance to those seen in hot EUV lines. Hot loops, especially some of those observed in the X-rays, can attain much greater heights than cool ones. Both hot and cool loops exhibit a wide range of lengths but certain classes of X-ray loops

are much longer than cool loops observed in H_α or cool EUV lines. Hot and cool EUV loops have the same diameter but cool H_α and L_α loops appear to be much thinner than any other class. In general hot loops last longer than cool ones. It is difficult to compare the electron densities in hot and cool loops since, both cover a large range, with undesirable overlap. The gas pressures have a smaller range and the values for both hot and cool loops are of the same order. In general hot loops tend to be thicker, longer, higher and longer lived than cool loops. Other morphological and physical properties except temperature are also similar.

2.11 SPATIAL RELATIONSHIP BETWEEN HOT AND COOL EUV LOOPS:

Foukal (1975) inferred that the peak emission from a cool loop coincides with a drop in the level of the hot EUV emission, which then rises to a low peak on either side. Foukal interpreted the observation as implying the existence of concentric sheaths of increasingly hotter material around a cool core; so that what is seen as a hot EUV loop is really a sheath of hot gas surrounding a cool EUV loop. This idea was subsequently elaborated by Levine and Withbroe (1977) by studying the variation in the physical conditions in a loop as a function of distance from the axis. Hot

35

and cool EUV loops, although obviously related, are regarded as separate physical structures (Dere;1982, Cheng et al;1980).

2.12 FLARE LOOPS:

Much of the knowledge of flare loops is from the photographs obtained on the disk and beyond the limb in the H_α line. Disk observations throw light on their relationship with flares,while the .limb observations yield information on the structure,dynamics,life time and evolution (Bruzek,1964). **Figure 2.4** shows a typical well developed loop system photographed simultaneously in H_α and $\lambda 5303 A^O$ at the Mees Solar Observatory, Haleakala (McCabe,1973). A number of loops is seen to be present, although it is not possible to count them.

Solar flares are remarkedly diverse and complicated phenomena involving transient heating of the localized regions of the corona and underlying chromosphere within an active region. The sudden release of energy is accompanied by the emission of electromagnetic radiation over a very wide span of the spectrum, ranging in extreme cases from γ-rays to kilometric radio waves. In almost all cases,flares seen in the chromospheric H_α line also

Fig.2.4. Loop prominence system photographed simultaneously in H_α(upper) and $\lambda 5303A^\circ$of Fe XIV(lower) at the Mess Solar Observatory,Haleakala(McCabe,1973). The loop details appear sharper in H_α than in $\lambda 5303A^\circ$.

produce an increase in the flux of soft X-rays. Both H_α and soft X-ray emission pertain to what is called the 'thermal' or 'quasithermal' component of the flare; i.e. they originate in plasmas where the distribution of electron velocities is believed to be Maxwellian. All flares pass through at least three phases: rise, maximum and decay (Moore et al., 1980). These phases are easily recognizable in curves showing the variation of the H_α intensity and soft X-ray flux over the life time of a flare. The physical properties of a flare change markedly over its lifetime.

The morphological and dynamical properties of H_α loops of both flare and non-flare loops are the same or nearly the same. However, compared with non-flare loops, H_α flare loop system appear to be slightly higher and lasts longer, as do the individual flare loops. EUV flare loops are also similar to those of EUV non-flare loops. EUV flare loops appear to lie some what lower, but the ranges of values overlap. In the microwave region, data are inadequate to make comparison between flare and non-flare loops. In the soft X-ray region, both flare and non-flare loops reach very great heights, but the non flare ones appear to reach greater heights. Comparison of the physical conditions of the flare loops with hot non-flare loops indicate, that independent of the wavelength region, the flare loops are approximately an order of

magnitude hotter compared with non-flare loops. Further, except in
the EUV region, the electron density of the flare loops is also an
order of magnitude greater. Thus, it is reasonable to arrive at
the conclusion that the gas pressures in flare loops is
approximately two orders of magnitude greater than in non-flare
loops. The value of the total magnetic field B in the microwave
region is bigger for flare loops than for non-flare loops. Unlike
hot flare loops the value of T_e for cool flare loops in H_α and
other visible region lines is similar to that of cool non-flare
loops.

Thus, hot flare loops are distinguished from hot non-flare
loops by their different physical conditions rather than by
morphological differences. On the other hand, cool flare loops can be
distinguished from non flare cool loops only by characteristics
other than their morphological and physical properties.

2.13 SUMMARY:

Though, there is a storehouse of information on the
observed properties of coronal loop structures, in different regions

of the electromagnetic spectrum, there is no physical model which is valid for all types of loops. One of the reasons for this situation is the insufficiency of data on coronal magnetic fields, which govern the morphological and dynamical properties of all types of loops. Coronal magnetic field models are discussed in Chapter 3. A three dimensional modeling of the spatial and temporal evolution of coronal loops is discussed in chapters 4 and 5 respectively.

3 CORONAL MAGNETIC FIELD MODELS

3.1 INTRODUCTION:

In the previous chapter the observed properties of coronal loops were described. To interpret the observed properties and to provide an account of the physics of coronal loops, some of the models that have been established are discussed in this chapter. There is very little empirical knowledge of the strength of the coronal magnetic field and almost none of its topology. Hence, a relationship between the plasma loop properties, physical conditions in them and the coronal magnetic field is based on theoretical models. The models governing the structure of magnetic fields are inferred from measurements of the magnetic field made in the solar photosphere, the only region where such measurements are at all reliable. This method provides a basis for comparing the structure of the observed plasma morphology with that of the extrapolated and inferred fields.

Despite the inability to measure the field in the corona

with any precision a simple calculation establishs its importance. The spatially averaged magnetic flux density in the solar photosphere ranges from about 0.4mT in the quietest regions to over 30mT in the active regions. The minimum mean square field strength can be obtained by assuming the field to be uniform; hence the magnetic pressure B^2/μ_0ranges upwards from about 0.1Pa in quiet regions to well over 400Pa in active regions. In the low corona which are at heights of 2000Km or so, these estimates will not be significantly different since this distance is small compared to the radius of the sun $(7 \times 10^5 Km)$. On the other hand, empirical estimates of the gas pressure in coronal active regions lie in the range of 0.1- 1Pa. Hence, the magnetic pressure greatly exceeds the gas pressure.

The magnetic field in the corona cannot be measured with precision, however, by calculations as mentioned above it is found that the magnetic pressure greatly exceeds the gas pressure. The solar corona is a low β gas (β is the ratio of gas pressure to the magnetic pressure) while the sub surface region is a high β gas. In a low β system the field controls the gas, while for a high β gas, the gas dynamics controls the field. In low β systems, the field either can simply expand in response to unbalanced magnetic pressures or can adopt a static configuration in which magnetic stresses balance one another- a situation in which the field is

42

said to be force free every where. A field which is force free throughout a given volume must experience stresses on some bounding surface in order to maintain it. In the case of the solar corona, the field cannot simply expand away because it is anchored by the gas dynamical stresses exerted on the sub surface portion of the field. These stresses are, of course, continually varying and produce in the corona a state of constant evolution. However, the observed changes to the overall structure of the coronal loop systems are generally slow, which suggests that as a first approximation the variations can be ignored and a static magnetic structure can be assumed.

3.2 FORCE FREE FIELD:

In order to focus on the geometric properties of the magnetic field, a model in which the field is static and is determined solely by the distribution of its own stresses, free from any considerations of the gas that must be present is adopted. This assumption reduces the problem to that of finding solutions of the Maxwell's equation for which the Lorentz force vanishes everywhere with in the coronal volume. i.e.,

$$j \times B = 0 \tag{3.1}$$

subject to the appropriate conditions at the lower bounding surface that reflect the determining influence of the sub surface field and current distributions. Equation (3.1) to be true, requires that either current density j should be parallel to the magnetic induction or it should vanish. Hence,

$$\mu_0 \mathbf{j} = \alpha(\mathbf{x}, t)\mathbf{B} \tag{3.2}$$

μ_0 is the permeability of free space. Current free case corresponds to $\alpha = 0$. If the field is assumed to have attained a static configuration, the parameter α becomes a function of position alone. Hence, using Maxwell's equation for a stationary system

$$\bar{\nabla} \times \mathbf{B} = \mu_0 \mathbf{j} \tag{3.3}$$

$$\text{or, } \bar{\nabla} \times \mathbf{B} = \alpha(x)\mathbf{B} \tag{3.4}$$

In the integral form equation (3.4) can be written as

$$\int_s (\nabla \times B) \cdot dS = \int_s \alpha \, B \cdot dS \tag{3.5}$$

where, s is any surface within the volume

44

By Stokes theorem the surface integral can be transformed to

$$\int_s (\bar{\nabla} \times B) . dS = \oint_c B . dl \qquad (3.6)$$

where, c is the curve bounding the surface s and dl is a line element of the curve c. If s is assumed to be a flat disk c will be its perimeter. The RHS of the equation (3.6) represents the component of the field around the circle and the RHS of equation (3.5) the component of the field normal to the disk. Thus, α determines a measure of the degree of twist of the field. When $\alpha=0$ there is no current and no twist. Such a field configuration is known as a potential field.

Taking the divergence of equation (3.3), it is found, that in the steady state

$$\bar{\nabla} . j = 0 \qquad (3.7)$$

Equation (3.7) indicates that like a magnetic field, a steady current cannot end in space.

Taking the divergence of equation (3.2),

$$(B. \bar{\nabla})\alpha + \alpha \bar{\nabla}. B = (B. \bar{\nabla})\alpha = 0 \qquad (3.8)$$

45

which implies that the value of α does not change in the direction of the field and so remains constant along a field line. If the field line crosses the boundary into a force free region, it maintains the value of α set by the boundary condition throughout the volume.

The solution to the equation,

$$(\bar{\nabla}\times B)\times B = 0 \qquad\qquad (3.9)$$

is non linear. The equation may not have a guaranteed solution and if it has, it may not be necessarily unique. Construction of general force free models for the coronal magnetic fields is a mathematically intractable problem.

The difficulty associated with general models (existence and uniqueness of the solution) is overcome if, α is deemed to be a constant within the volume under consideration. This will ensure the invariance of α between foot points. The solution of equation (3.4) when α is a constant are the eigenfunctions of the curl operator. Instead of solving this equation directly, Chandrasekhar and Kendall (1975) took curl of both sides to produce the Helmholtz equation for each cartesian component of B

$$(\bar{\nabla}^2 + \alpha^2)B = 0 \qquad\qquad (3.10)$$

This equation is linear in B for a given α so that the solution will describe a **linear force free field.**

Seehafer(1978); Alissandrakis(1981); Chen & Chen(1989) have adopted linear force free fields to the modeling of the regions of the finite horizontal extent, such as an active region. The solutions are not however unique if normal component of the magnetic field B_n is specified only on the lower boundary (Chiu & Hilton,1977). Most observations furnish only the normal component of the field at the photospheric surface. Comparison of the structure with observations of the morphology of active regions are arbitrary because they are based upon models in which the value of α is adjusted to provide the best agreement between the observed morphology and the field. Since, observations give no indication whether this procedure is justified, the validity of the constant α model for coronal field is doubtful.

Heyvaerts and Priest(1984), provide a justification for an approximately constant α force free field in the solar corona. Since, it is assumed that the coronal magnetic field evolves through quasi-static equilibrium structures as the field at the photospheric boundary changes slowly. During the time interval over which equilibrium is achieved, the changes in the boundary condition may be neglected and it may be supposed that the field

47

structure changes only within the volume where the field must be force free. Under these circumstances Woltjer(1958) has proved that in the limit of infinite electrical conductivity (ideal MHD), magnetic helicity is conserved for each field line as the field evolves within the volume V. Magnetic helicity is defined as $\mathbf{A.B}$ where $\mathbf{A}$ is the vector magnetic potential ($\mathbf{B} = \bar{\nabla} \times \mathbf{A}$). Like α, the magnetic helicity is also a measure of the twist of the field, but unlike α, the helicity of a potential field does not necessarily vanish. If helicity is conserved for each field line, the total helicity in the volume

$$K = \int_{v} \mathbf{A.B}\ dV \qquad (3.11)$$

will be constant throughout. The total magnetic energy

$$E_{m} = \int_{v} (B^{2}/2\mu_{0})\ dV \qquad (3.12)$$

will however change. The lowest possible value occurs when the field adopts precisely that constant α force free configuration having the prescribed normal component B_{n} on the boundary (Sakurai,1979).

48

Although a minimum energy state exists, the system has no means of evolving to this state when there is no dissipation, i.e. when electrical conductivity is infinite. If dissipation is allowed by introducing the conductivity to be finite, helicity will no longer be conserved on each field line

3.3 MODEL EQUATIONS FOR THE CORONAL PLASMA:

3.3.1 MHD APPROXIMATION:

At the high temperatures and low densities, characteristic of the corona, the atoms of the coronal gas are almost all ionized. The long range electrostatic forces between the charges govern the small scale motion of the particles. Any medium in which this is the case is said to be a plasma. It is the basic property of plasma that the strength of the electrostatic interaction precludes any permanent large scale separation of opposite charges. The average charge density is effectively zero everywhere, so that large scale dynamics of a plasma is controlled by the magnetic field. Magnetohydrodynamics and plasma physics both deal with the behavior of the combined system of electromagnetic fields and a

conducting liquid or gas. Conduction occurs when there are free or quasi free electrons which can move under the action of applied fields. Unlike a solid in the case of a fluid the field acts on both electrons and ionized atoms to produce dynamical effects, including bulk motion of the medium itself. This mass motion in turn produces modifications in the electromagnetic fields. The distinction between plasma and magnetohydrodynamics can be established by considering the relation $J = \sigma E$. In conducting liquids or dense ionised gases the collision frequency is sufficiently high even for very good conductors that there is a wide frequency range over which Ohm's law in its simple form is valid. Under the action of applied fields the electrons and ions move in such a way that, apart from the high frequency jitter, there is no charge separation. Electric field arises from the motion of the fluid which causes a current flow, or as a result of time varying magnetic fields or charge distributions external to the fluid. The mechanical motion of the system can then be described in terms of a single conducting fluid. At low frequencies the displacement current is neglected in Ampere's law. This approximation is called magnetohydrodynamics.

In a less ionised gas the collision frequency is smaller. There may still be a low frequency domain where the magneto

50

hydrodynamic equations are applicable. Astrophysical applications fall in this category. At higher frequencies the charge separation and the displacement current cannot be neglected. The separate inertial effects of the electrons and ions must be included in the description of the motion. This domain is referred to as "plasma physics". At higher temperatures and lower densities, the electrostatic restoring forces become so weak that the length scale of charge separation becomes large compared to the size of the volume being considered. Under such circumstances the collective behavior implicit in a fluid model is gone completely. A plasma is an ionised gas in which the length that divides the small scale individual particle behavior from the large scale collective behavior is small compared to the characteristic lengths called the Debye length (which is numerically equal to $7.91(T/n)^{1/2}$cm, where T is the absolute temperature in degrees Kelvin and n is the number of electrons per cubic centimeter). For length and time scales larger than the charge separation scales the plasma may be treated as a fluid and the magnetohydrodynamic description is used. In a fluid, the transport processes of diffusion, viscosity, heat conduction and electrical resistance can all be modeled in terms of the local thermal and dynamical properties of the gas, the temperature T, the pressure P and bulk velocity V together with the macroscopic magnetic induction B.

3.3.2. MHD DESCRIPTION OF LOOPS:

Consider a nonpermeable conducting fluid in electromagnetic field. Let it be described by a matter density $\rho(x, t)$, a velocity $v(x, t)$, a pressure $p(x, t)$ (taken to be a sclar), and a real conductivity σ. The hydrodynamic equations are the continuity equation

$$\frac{\partial \rho}{\partial t} + \bar{\nabla}.(\rho v) = 0 \qquad (3.13)$$

and the force equation:

$$\rho \frac{dv}{dt} = -\bar{\nabla}p + \frac{1}{c}(J \times B) + F_v + \rho g \qquad (3.14)$$

In addition to the pressure and magnetic-force terms viscous and gravitational forces have been included. The time derivative on the LHS is the convetive derivative which gives the total time rate of change of a quantity moving instantaneously with the velocity v.

$$\frac{d}{dt} = \frac{\partial}{\partial t} + v.\bar{\nabla} \qquad (3.15)$$

For an incompressible fluid the viscous force can be written as:

$$F_v = \eta\bar{\nabla}^2 v \qquad\qquad (3.16)$$

where η is the coefficient of viscosity.

Neglecting the displacement current, the electromagnetic fields in the fluid are described by

$$\bar{\nabla} \times E + \frac{1}{c} \frac{\partial B}{\partial t} = 0 \qquad\qquad (3.17)$$

$$\bar{\nabla} \times B = \frac{4\pi}{c} J \qquad\qquad (3.18)$$

The condition $\bar{\nabla}.J = 0$, is equivalent to the neglect of displacement currents. From Faraday's law $(\partial/\partial t)$ $\bar{\nabla}.B = 0$ and the requirement $\bar{\nabla}.B = 0$ can be imposed as an initial condition. With the neglect of the displacement current, it is appropriate to ignore Coulomb's law as well. To complete the specifications of dynamical equations the relation between the current density J and the fields E and B are to be specified. For a one component conducting fluid, Ohms law can be written as:

$$J = \sigma \left(E + \frac{v}{c} \times B\right) \qquad\qquad (3.19)$$

The equations (3.13),(3.14),(3.17),(3.18)and (3.19) together with

an equation of state for the fluid, form the equations of magnetohydrodynamics.

3.4 STEADY STATE STRUCTURE OF LOOPS:

The model with the coronal plasma in magneto static configuration (V=0) is the simplest case for a theoretical discussion. This implies finding a solution for the equation

$$- \bar{\nabla}p + \rho \, \bar{\nabla}\Phi + JxB = 0 \qquad\qquad (3.20)$$

allowing a small Lorentz force to be balanced by equally small pressure and gravitational forces. Along with this, the following equations

$$\bar{\nabla}.B = 0, \qquad \bar{\nabla} \times B = \mu_0 j \qquad\qquad (3.21)$$

and, an energy equation are required.

In the steady state $\partial/\partial t \equiv 0$ and pressure balance condition is

$$\nabla (-p + \rho\Phi) + jxB = 0$$

When the density is treated as an independent scalar field, it is possible to find fully three dimensional solutions that have the geometry of the system of loops(Low,1982) or a large scale coronal structures (Bogdan & Low,1986). According to Priest(1978), the separate requirements of force and energy balance are incompatible, and that a system of loops cannot be in magneto static equilibrium. Staedy state structure can also be discussed without assuming the flows V to be = 0. This will be discussed in Chapter 5.

3.5 LOOP MODELING:

The historical development of modeling outer stellar atmosphere has followed two principal directions:emission measure (or empirical) analysis and energy-balance modeling. The former line-of-attack focuses directly upon the observations to generate the expected differential emission measure $Q(T) \equiv N_o^2 (dT/ds)^{-1}$ along the instrument line of sight in the atmosphere, and uses this result to deduce the parameters characterising the atmosphere,as well as the required mechanical heating to maintain energetic equilibrium(Withbroe,1975; the review by Gabriel,1976a;and the detailed analysis in Craig & Brown ,1976). The second approach is based upon the solution of a local energy balance equation,together

55

with relations specifying momentum and mass balance and an equation of state: these together with boundary conditions that are used as adjustable parameters and integration over the model atmosphere, yield expected radiative fluxes that are compared with observations, with parameters varied as to obtain a "best fit"(cf Kopp & Orrall, 1976; and Rosenner and Vaiana, 1977 for application to coronal hole modeling). The two analysis techniques generally adopted are 1)Emission measure analysis and 2)Energy balances analysis which are considered to be alternative means of modeling the solar atmosphere(cf Gabriel, 1976a; Orall & Kopp, 1976 and Withbroe & Noyes, 1977). Due to the strong coronal structuring provided by high-spatial-resolution observations, the two methods mentioned above become complementary, thus providing answers to somewhat different questions about the atmosphere. These modeling techniques have been most fully developed in the context of homogeneous atmospheres, particularly for the quiet sun.

By regarding coronal loops as plasma volumes relatively isolated by the magnetic field that defines them, each individual loop structure can be characterised by two coordinates specifying displacement along the length of the loop(s) and radial displacement from the loop axis(r). In general, the equations of motion of the plasma is solved within the loop subject to the boundary conditions at the foot points and at the "surface" of the

56

loop,with the additional constraints upon the internal transport process imposed by the magnetic field. A complete treatment then includes the effects of plasma upon the coronal magnetic field,providing a full MHD description of the coronal structures. Current modeling has attempted to lay the groundwork by investigating separately longitudinal and radial temperature and density structure of coronal loops. Since the magnetic field defines the longitudinal loop coordinate,these studies have further segregated themselves into; longitudinal analysis using energy balance arguments,while radial studies emphasises the emission measure analysis.

3.6 RADIAL STRUCTURE OF THE LOOPS:

Extensive studies of the radial structure of coronal loops by (Foukal, 1975, 1976, 1978) using EUV line intensity data from the HCOS-O55 spectroheliometer and emission measure analysis techniques have revealed that coronal loops undergoing dynamic change (such as post flare loops) are characterised by a non stationary,"inverted" temperature structure, in which the core is cool relative to a substantially hotter surrounding sheath. It has not been possible to correlate these EUV observations with simultaneous soft X-ray data;

for example the event studied by Levine and Withbroe in which case a small soft X-ray loop was observed to flare $\sim 10^4$ sec before the initiation of EUV observations at the location of the EUV event, but no temporaly overlapping data was obtained. A question that remains unanswered is whether such complex loop structures are a norm, or they reflect the consequences of occasional, significant departures from quiescent conditions. Foukal(1978) has studied long lived ($\geq 10^5$ sec) cool loops at least one of whose foot points emerges from sunspots, and has shown their observed size, low temperature and life time taken together, to be inconsistent with simple hydrostatic equilibrium. Therefore he has suggested that these structures are in dynamic stationary equilibrium, with observed downward mass flow along the loop axis(and field) balanced by mass inflow across the field, whose energy balance is largely controlled by the mass flow rate.

3.7 LONGITUDINAL STRUCTURE OF LOOPS:

Longitudinal loop structure due to the anisotropies introduced by the coronal magnetic field emphasizes energy balance arguments. Landini & Monsignori-Fossi(1975) have refined the work of Jordan(1975) and have given a detailed description of the

temperature and density structure of the individual coronal X-ray loop. Using the temperature as the independent variable, it has been possible to derive an analytical description of the variation of temperature and density within the loop, and a sequence of loop models by varying the base pressure and maximum coronal temperature, based on the hypothesis of acoustic heating. Such work based on the emission measure analysis techniques has led to the essential result that X-ray structures could be identified in a quantitative manner with regions of enhanced temperature and density and hence enhanced energy deposition. However, there is no details regarding the relation of the size of the loop structure to its other attributes in these works.

The technique of Landini and Monsignori-Fossi has been extended by Rosner, Tucker and Viana(1978) to show that stable quiescent X-ray loop structures must have their temperature maximum at their apex, resulting in scaling laws for the loop temperature and heating rate.

3.8 ONE DIMENSIONAL MODELS:

One dimensional models of coronal flux loops account only

for mass, momentum and energy balance along the field lines. Also the geometry of the field line is assumed, so that the dynamic and thermal properties of the loop can be analysed without reference to the field.

Steady state models have been classified into two classes, one which is truly static i.e., without any gas flows, and the other which allow a steady, time independent flow along the loop. The observations of the emission measure from loops and ensembles of loops are consistent with simple loop(static) models, though there is very little constraint on the free parameters of the model. However, the model allows insight to be gained into more complicated structures.

The assumption that loops are static is invalidated by their observed properties. The apparent life times of the loops suggest that they are maintained for times at least comparable to the time for a sound wave or Alfven wave to propagate along its length. Steady flows from one foot point of a loop to the other are inevitable if conditions of perfect symmetry on the geometry of the magnetic field are violated. In hot loops, the flows are relatively slow and cause little change to the overall structure. But as the maximum temperature of the loop decreases, the flow speeds tend to increase throughout the loop and the

asymmetry between the two legs becomes much more pronounced. In cool loops the emission characteristics models are more in line with observations.

One dimensional loop models appear to be stable not only to infinitesimal perturbations but also to very large finite amplitude disturbances. However, a one dimensional analysis allows only necessary conditions for stability. Sufficient conditions can be found only by examining all possible perturbations, including those that produce transverse disturbances of the loop. For this a MHD model of the coronal loop is needed. In the one dimensional model the thermodynamic structure and plasma motion in the direction of the field lines may be analysed without regard to the magnetic field. Since loops have transverse structure as well as longitudinal, the properties of the loops vary over their cross section and from one another.

3.9 SUMMARY:

The early view, which is still regarded as the appropriate one, considers the extended atmosphere, and corona in particular, as the simple, direct byproduct of convective "noise". Inspite of the

61

differences about the nature of coronal heating mechanism, there is a general agreement that the turbulent fluid motions at the photospheric level as the source of energy supply. The solar corona appears to correlate its intensity not with the level of local photospheric convective activity but rather with the topological nature of the magnetic field. These circumstances raise an interesting question as to whether the formation of corona as opposed to the extended atmosphere as a whole is at all related to the level of surface convective activity. The role of the magnetic field is a further correlate to this question.

4 THREE DIMENSIONAL STEADY STATE STRUCTURE OF SOLAR CORONAL LOOPS

4.1 INTRODUCTION:

Solar active regions are found to be magnetically, spatially as well as temporally complex, the complexity being manifested through emissions at optical UV, EUV and X-ray wavelengths. The solar corona is highly structured. The most common geometrical form observed in the active regions looks like a loop or an arcade of loops essentially outlining the local magnetic field configuration. These loops are believed to contain current carrying plasma and therefore have a helical form of the magnetic field (Levine and Altschuler,1974;Poletto et al.,1975; Krieger et al.,1976; Priest,1978; Hood and Priest, 1979.). The MHD equilibria of coronal loops have been investigated by Tsinganos (1982). Inspite of the continuous pumping of magnetic and velocity field fluctuations into the coronal plasma, the loops exhibit a fairly stable and well configured geometry. The steady state pressure structure is the result of various manifestations of the balance of inertial and magnetic forces. High spatial resolution

observations of lines of C II,C III,O IV,Ne VII and Mg x indicate that in the steady state, a typical loop consists of a cool central core with temperature increasing towards the surface which merges with the hot corona outside.

From purely statistical treatment of the magneto-hydrodynamics of an incompressible fluid subject to the invariance of total energy, magnetic helicity and magnetic flux, a steady state configuration of the magnetoplasma including turbulence has been derived by Krishan (1982). Krishan (1983a,b) have also discussed a steady state model of active region coronal loops using statistical theory of incompressible magnetohydrodynamic turbulence described by Montgomery et al (1978). The method adopted follows that of Montgomery et al (1978), wherein the steady state is described by the superposition of Chandrasekhar-Kendall(C-K) functions which are eigenfunctions of the curl operator. The force free magnetic fields ($\bar{\nabla} \times \bar{B} = \alpha\bar{B}$) and the Beltrami flows ($\bar{\nabla} \times \bar{V} = \alpha\bar{V}$) represent the minimum energy state of a magneto-fluid. A single C-K function represents these configurations of the magnetic and velocity fields. The magneto-fluid in the coronal loop is believed to be in an approximate state of the force free fields with small departures from the current free fields of the photospheric fluid. Though a single C-K function represents a force free state, superposition of these functions is not force free. By

representing the fields as the superposition of the C-K functions, we can maneuver these departures in a systematic and quantitative manner. Thus, in general the steady state may have small departures from a force free state and it is possible to account for the discrepancies in the observed and the model force free state by the addition of more than one such states. This approach differs from the usual MHD stability theory in the sense that it does not involve small perturbation expansion and therefore is fully nonlinear. The main features of the theory consists of using the MHD equations for an incompressible fluid. The magnetic and velocity fields are expanded in terms of C-K functions. The completeness of these functions has been proved by Yoshida and Giga(1990). The pressure profile of the plasma is obtained from a poisson equation for the mechanical pressure as a function of velocity and magnetic fields.

Further, following Montgomery et al (1978), the toroidal and poloidal magnetic fluxes are introduced as additional invariants. This results in several states being accessible for a fixed value of the ratio of toroidal and poloidal fluxes and for a fixed value of the axial and azimuthal mode numbers (n, m) respectively. The lowest mode state (m=n=0) has accounted for the radial temperature profile of a cool core with a hot sheath loop. This has been extended to the study of the statistical distribution of the

velocity and magnetic fields in the state m=n=0 by Krishan (1985). The results of this method sets the trend for studying the nature of magnetic field and velocity field fluctuations, their interrelationship, their correlations and the temporal behavior in the solar coronal loops. The superposition of the two C-K functions brings in the three dimensional spatial variations (r, θ, z) in the plasma parameters and the state does not correspond to a force free state. The study has been restricted to two dimensional variations (r, z) of the plasma temperature as observational results on the azimuthal variations are not available. The results indicate that the radial variation of pressure corresponding to the larger spatial widths of the hotter lines does not exist all along the length of the loop. A twisted configuration of plasma is obtained. The pressure or temperature is maximum at the top of the loop but only near the axis. On smaller spatial scales, the radial pressure variation exhibits oscillations.

It is evident from the above discussion that there has been no attempt made so far to study the three dimensional spatial profile of the coronal loops. The constraints have been due to difficulties in observation and whatever has been known is only in a two dimensional plane. Hence, the present study, is an extension of the earlier work of Krishan (1987). The earlier work has been

66

extended to include the three dimensional variations of pressure in coronal loops by representing the velocity and magnetic fields as the superposition of three C-K functions. This brings in the three dimensional spatial variation (r, θ, z) in the plasma pressure. Though the individual C-K functions represent a force free state the super position does not. The three mode representation, besides exhibiting a chaotic behavior admits temporal behavior of the fields in its most basic form. A truncated three mode configuration has been explored by Chen, Shan and Montgomery (1990) and their results qualitatively agree with the predictions as well as with computations obtained using the numerical code (Dahlburg et al 1986, 1987, 1988 and Theobald et al 1989.).

4.2 DERIVATION OF THE PRESSURE PROFILE :

The coronal loop plasma is represented by a cylindrical column of length 'L' and radius 'R'. The equations describing an incompressible ideal MHD turbulent plasma in terms of fluid velocity V and the magnetic field B are

$$\frac{\overline{\nabla} P}{\rho} = \frac{(\overline{\nabla} \times B) \times B}{\rho} - (V.\overline{\nabla})V - \frac{\partial V}{\partial t} \qquad (4.1)$$

$$\overline{\nabla}\mathrm{x}(\overline{\nabla} \times B) - \frac{\partial B}{\partial t} = 0 \qquad\qquad (4.2)$$

where P is the mechanical pressure and ρ is the mass density. The force due to gravity has been neglected. Equations **(4.1)** and **(4.2)** preserve in time the constraints

$$\nabla \cdot V = 0 \qquad \text{and} \qquad\qquad (4.3)$$

$$\nabla \cdot B = 0 \qquad\qquad (4.4)$$

Using the identity

$$(V.\nabla) \; V = (\nabla \times V) \times V + 1/2 \; \nabla V^2 \; ,$$

equation **(4.1)** reduces to

$$\overline{\nabla}\Big[P/\rho + (1/2)V^2 \Big] = \left[\frac{(\overline{\nabla}\mathrm{x}B)\mathrm{x}B}{\rho} - (\overline{\nabla}\mathrm{x}V \;)\mathrm{x}V \right] - \frac{\partial V}{\partial t} \qquad\qquad (4.5)$$

In the steady state $\partial V/\partial t = 0$ and for a force free representation of the magnetic field and for a Beltrami flow i.e., for $\overline{\nabla}\mathrm{x}B = \alpha B$ and $\nabla\mathrm{x}V = \alpha V$, we find,

68

$$\bar{\nabla} \, [\, P/\rho + 1/2 \ V^2] = 0 \qquad\qquad\qquad (4.6)$$

Equation (4.6) also holds good where there is equipartition of energy between velocity and magnetic fields.is i.e.,when $|V|$ = $|B|/\rho$.

In cylindrical geometry, with a rigid perfectly conducting, impenetrable wall at a radius r =R, the boundary conditions on B and V at r= R are $V_r(r =R)=0$ and $B_r(r= R)=0$. A periodic boundary condition with period L in the z direction is assumed. Identifying L with the major circumference of a torus enables to include the case of a toroidal boundary with curvature neglected.. The z or the axial direction is referred to as the "toroidal" direction and the θ direction as the "poloidal" direction.

Following the procedure adopted by Montgomery et al(1978), the velocity field V and magnetic field B in the loop plasma are represented by the superposition of Chandrasekhar-Kendall functions. They are eigenfunctions of the curl operator. They are the solutions of the eigenvalue problem $\bar{\nabla} \times \mathbf{a} = \lambda \mathbf{a}$, where λ is real. Individually they are force free fields although the sum of two or more of them is not, in general, force free. The

69

complete dynamics can be described by a set of infinite coupled nonlinear ordinary differential equations which are of first order in time for the expansion coefficients of velocity and magnetic fields and it is a formidable task to find solutions to these equations. Hence, the fields are represented by the superposition of the three lowest order C-K functions. Another justification for doing so is that these functions represent the largest spatial scales and therefore may be the most suitable states for comparison with observed phenomena.

The eigen functions of the curl operator can be written as:

$$\mathbf{a}_{(n,m,q)} = \overline{\nabla}\psi_{(n,m,q)} \times \hat{e}_z + \overline{\nabla} \times \left[\overline{\nabla} \times \left(\hat{e}_z \psi_{(n,m,q)} \right) \right] / \lambda_{(n,m,q)}$$

(4.7)

where $\psi_{(n,m,q)}$ is a solution of the scalar wave equation

$$[\nabla^2 + \lambda^2_{(n,m,q)}]\psi_{(n,m,q)} = 0 \qquad (4..8)$$

$$\psi_{(n,m,q)} = J_m(\gamma_{nmq} r) \exp(im\theta + ik_n z) \qquad (4.8a)$$

where $\lambda_{(n,m,q)} = \pm (\gamma^2_{nmq} + k^2_n)^{1/2}$ \qquad (4.8b)

70

Here, $k_n = 2\pi n/L$, where $n = 0, \pm 1, \pm 2, \ldots$.

The integer m takes on the values $m = 0, \pm 1, \pm 2, \ldots \ldots$,

$\gamma_{nmq} > 0$ and is determined as that solution which makes equation (4.7) satisfy the boundary conditions at $r=R$. $J_m(\gamma_{nmq} r)$ is the Bessel function.

Written in detail equation (4.7) is

$$\bar{a}_{(n,m,q)} = \hat{e}_r\left[\frac{im}{r} + \frac{ik_n}{\lambda_{(n,m,q)}}\frac{\partial}{\partial r}\right]\psi_{(n,m,q)}$$
$$+ \hat{e}_\theta\left[-\frac{\partial}{\partial r} - \frac{mk_n}{r\lambda_{(n,m,q)}}\right]\psi_{(n,m,q)}$$
$$+ \hat{e}_z\left[\frac{\lambda_{(n,m,q)}^2 - k_n^2}{\lambda_{(n,m,q)}}\right]\psi_{(n,m,q)} \qquad (4.9)$$

For the inequality $m^2+n^2>0$, the condition $R_r = 0$ at $r= R$, requires

$$Rk_n\gamma_{nmq} J'_m(\gamma_{nmq}R) + m\lambda_{(n,m,q)}J_m(\gamma_{nmq}R) = 0 \qquad (4.10)$$

The eigenvalues for $m=n=0$ are not determined by the radial boundary condition, since $R_r=0$ for $n=m=0$. $\lambda_{(0,0,q)}$ is determined using the fact that for each individual $(0,0,q)$ mode the ratio of the toroidal magnetic flux ψ_t to the poloidal flux ψ_p is

71

$$\frac{\psi_t}{\psi_p} = - \frac{R}{L} \frac{|\lambda(0,0,q)|}{\lambda(0,0,q)} \frac{J'_0(\gamma_{00q}R)}{J_0(\gamma_{00q}R)}$$

(4.11)

Where ψ_t and ψ_p are defined as follows:

Using the vector potential A, for which $B = \bar{\nabla} \times A$, and it obeys $\partial A / \partial t = \nabla \times (\bar{\nabla} \times A) + \bar{\nabla} \phi$. Writing the z and θ components at $r=R$ and integrating over one period(As there is no contribution from the $\cdot \nabla \times (\bar{\nabla} \times A$ term). ψ_t and ψ_p have the dimensions of magnetic fluxes.

$$\psi_p = \int_0^L dz \int_0^{2\pi} d\theta\, A_z = \text{Constant}, \quad r = R,$$

$$\psi_t = \frac{R}{L} \int_0^L dz \int_0^{2\pi} d\theta\, A_\theta = \text{Constant}, \quad r = R$$

$$\psi_t = - 2\pi R \sum_q \xi_{(0,0,q)} \gamma_{00q} C_{(0,0,q)} J'_0(\gamma_{00q}r)$$

$$\psi_p = 2\pi L \sum_q \xi_{(0,0,q)} \lambda_{(0,0,q)} C_{(0,0,q)} J_0(\gamma_{00q}r)$$

Since both ψ_t and ψ_p are constants of the motion, it is natural to determine $\lambda(0,0,q)$ from equation (4.11) as:

72

$$\frac{J'_0(\gamma_{00q}R)}{J_0(\gamma_{00q}R)} = -\frac{L}{R} \frac{\lambda_{(0,0,q)}}{|\lambda_{(0,0,q)}|} \frac{\psi_t}{\psi_p} \qquad (4\ 12)$$

for all $q = 1,2,3,\ldots$ $q=1$ is the eigenmode corresponding to the lowest $|\lambda(0,0,0)|$ The choice of equation **(4.12)** guarantees the orthogonality of all pairs of modes. For $n^2+m^2>0$, the modes occur in pairs, so that if λ is an eigen value $-\lambda$ is also one, corresponding to the opposite sign of m or n.

$A_{(n,m,q)}$ is the normalized $a_{(n,m,q)}$ such that

$$\int d^3x\ A^*_{(n,m,q)} \cdot A_{(n',m'q')} = \delta_{nn'}\delta_{mm'}\delta_{qq'} \qquad (4.13)$$

$\delta_{nn'} = \delta_{mm'} = \delta_{qq'} = 1$ if, $n = n', m = m'$ and $q = q'$ and $=0$, if

n, m, q are not equal to n', m' and q' respectively.

The normalizing constant that relates $A_{(n,m,q)}$ to $a_{(n,m,q)}$ is given

by $A_{(n,m,q)} = C_{(n,m,q)} a_{(n,m,q)}$ \qquad (4.14)

Using equation **(4.13)** in **(4.14)**

$$\int C_{nm}^2 \, a_{nm} \cdot a_{nm}^* \, d^3x = 1 \qquad (4.15)$$

In cylindrical coordinates,

$$C_{nm}^2 = 1/\int a_{nm} \cdot a_{nm}^* \, rdr \, d\theta \, dz \qquad (4.16)$$

The limits of integration are: $r = 0$ to R, $\theta = 0$ to 2π and $z = 0$ to L
Eigen values of λ_{nm} for $n = m$ not equal to zero are obtained from equation (4.10). For the mode $n = 1$, $m = 1$, equation (4.10) yields:

$$\frac{2\pi R}{L} \gamma_{11} J_1'(\gamma_{11}R) + \lambda_{11} J_1(\gamma_{11}R) = 0 , \quad \text{or}$$

$$(\gamma_{11}R) \, J_1'(\gamma_{11}R) = -\frac{\lambda_{11}L}{2\pi} J_1(\gamma_{11}R) = -\frac{(\lambda_{11}R) \, J_1(\gamma_{11}R)}{2\pi(R/L)}$$

$$\lambda_{11}R = \pm \left[\gamma_{11}^2 R^2 + \left(\frac{2\pi R}{L}\right)^2 \right]^{1/2} \qquad (4.17)$$

where the ratio of the radius R to the length L of the cylindrical loop has been taken to be : $R/L = 0.1$

The value of $\gamma_{11}R$ satisfying equation (4.17) is $\sim$ <u>3.23</u>

Similarly for the mode n = 1, m = 0, from equation (4.10),

$$\frac{2\pi R}{L} \gamma_{10} J_0'(\gamma_{10}R) = 0, \text{ or}$$

$$J_0'(\gamma_{10}R) = 0 = - J_1(\gamma_{10}R) \tag{4.18}$$

The value of $\gamma_{10}R$ satisfying the equation (4.18) is <u>3.85</u>

For the mode n = 0   m = 1, from equation (4.10),

$$\lambda_{01} J_1(\gamma_{01}R) = 0 \text{ or } J_1(\gamma_{01}R) = 0 \tag{4.19}$$

The value of $\gamma_{01}R$ satisfying equation (4.19) is <u>3.85</u>

The corresponding values of λ's are

$$\lambda_{11}R = \underline{3.29}, \quad \lambda_{10}R = \underline{3.85} \quad \text{and} \quad \lambda_{01}R = \underline{3.85} \tag{4.20}$$

The values of normalisation constants are found to be:

$C_{11} = 2.922 \, L$

$C_{01} = 1.0198238 \, L$ $\qquad\qquad$ (4.21)

$C_{10} = 0.1278097 \, L$

The magnetic field B and velocity field V can be expanded in terms

C-K functions as:

$$B = \sum_{nmq} \xi_{(n,m,q)} \, \lambda_{(n,m,q)} \, A_{(n,m,q)} \qquad\qquad (4.22)$$

$$V = \sum_{nmq} \eta_{(n,m,q)} \, \lambda_{(n,m,q)} \, A_{(n,m,q)} \qquad\qquad (4.23)$$

where η's and ξ's are the expansion coefficients and are functions

of time.

Since, B and V are real, by symmetry condition the expansion

coefficients $\xi_{(n,m,q)}$ and $\eta_{(n,m,q)}$ must be such that

$\xi_{(n,m,q)} = \xi_{(-n,-m,-q)}$ so that $\xi_{(0,0,q)}$ and $\eta_{(0,0,q)}$ are real

for all values of q. In the truncated triple mode representation:

$$V = \lambda_a \eta_a(t) A_a + \lambda_b \eta_b(t) A_b + \lambda_c \eta_c(t) A_c \qquad\qquad (4.24)$$

$$B = \lambda_a \xi_a(t) A_a + \lambda_b \xi_b(t) A_b + \lambda_c \xi_c(t) A_c \qquad\qquad (4.25)$$

η's and ξ's are in general complex.

The functions a_{nm} satisfy $\nabla \times a_{nm} = \lambda_{nm} a_{nm}$.

γ_{nm} have been determined from the boundary conditions for a perfectly conducting and rigid boundary since the observations do show very well defined loop structures aligned with the magnetic field across which there is little or no transport. Thus the radial component of the velocity and the magnetic field vanish at the surface $r = R$.

In this chapter the study is confined to the steady state solution to the pressure For the steady state $\partial/\partial t \; [\eta, \xi] = 0$, and $\eta = \xi$. From equation (4.6),

$\nabla(P/\rho + 1/2V^2) = 0$,   which   implies

$P/\rho + 1/2V^2$ = constant   (4.26)

At the origin where $r = 0$ and $z = 0$, let the pressure be P0. Then, the constant of integration comes out as $= P_0/\rho + 1/2V_0^2$, where V_0 is the velocity at the origin. Hence, equation **4.6** reduces to

$$\frac{P}{\rho} = \frac{Po}{\rho} + \frac{1}{2} V_0^2 - \frac{1}{2} V^2 \qquad (4.27)$$

In this   configuration the total energy E of the loop plasma is given by

$$E = \sum_{i=a,b,c} \lambda_i^2 \, (\eta_i^2 + \xi_i^2) \tag{4.28}$$

Though there is some estimate of the total energy of a typical plasma loop, there is no obvious way of fixing the relative magnitudes of the three modes.   Two considerations which are generally used to fix the relative strengths of the three modes whenever such three mode interactions are involved are :

(1)Pump approximation, in which one of the three modes is considered as the strongest as compared to the other two.

(2) The mode strength is assumed to vary in proportion to their spatial scales. Equation (4.27) will be discussed in the light of these two considerations.

4.3 PUMP APPROXIMATION:

The spatial variation of pressure as already mentioned earlier is discussed for a cylindrical column of plasma for which the R/L ratio is assumed to be 0.1, and the ratio of the toroidal

to poloidal flux ψ_t / ψ_p as 0.1. Two triads $(a_1 b_1 c_1)$ and $(a_2 b_2 c_2)$ are chosen such that they represent the largest possible spatial scales, as well as satisfy the condition $a = b + c$. (as will be evident in time dependent case discussed in Chapter 5). The two triads chosen are,

$$a_1 = (1,1), \; b_1 = (1,0) \text{ and } c_1 = (0,1)$$

$$a_2 = (0,0), \; b_2 = (1,1) \text{ and } c_2 = (-1,-1)$$

The corresponding values of γ's and λ's are obtained from equation (4.10) as explained earlier. The values are

$$\gamma_a R = 3.23 \; , \; \gamma_b R = 3.85 \; , \; \gamma_c R = 3.85$$

$$\lambda_a R = 3.29 \; , \; \lambda_b R = 3.9 \; , \; \lambda_c R = 3.85$$

for the triads a_1, b_1, c_1 and,

$$\gamma_a R = 1.44 \; , \; \gamma_b R = 3.23 \; , \; \gamma_c R = 3.23$$

$$\lambda_a R = 1.44 \; , \; \lambda_b R = 3.29 \; , \; \lambda_c R = 3.29$$

for the triads a_2, b_2, c_2.

CASE 1 PRESSURE STRUCTURE P1 FOR THE TRIAD a1 = (1,1), b1 = (1,0),

and c1 = (0,1):

4.3.1 RADIAL VARIATION:

The mode 'a' is assumed to be the dominant or the strongest mode and it is called the pump. Since the conservation condition requires a = b+c the pump is assumed to share its energy with the other two modes. Therefore, let

$$\lambda_a^2 \eta_a^2 > \lambda_b^2 \eta_b^2 \qquad \text{and} \qquad \lambda_a^2 \eta_a^2 > \lambda_c^2 \eta_c^2 \qquad (4.29)$$

For the triads (a_1, b_1, c_1) i.e. for modes $(1,1),(1,0)$ and $(0,1)$

$$\frac{\eta_{b1}^2}{\eta_{a1}^2} < \frac{\lambda_{a1}^2}{\lambda_{b1}^2} = 0.8435 \qquad \text{and} \qquad \frac{\eta_{c1}^2}{\eta_{a1}^2} < \frac{\lambda_{a1}^2}{\lambda_{c1}^2} = 0.8659$$

We choose $|\eta_{a1}| = 10^7$ and $|\eta_{b1}| = |\eta_{c1}| = 8 \times 10^6$, so that the pump approximation is valid. The expression on the RHS of equation(4.27) has been averaged over a full cycle of θ. Figure 4.1 is a plot of pressure $(P_1 - P_0)$ as a function of $\gamma_a r$ for different
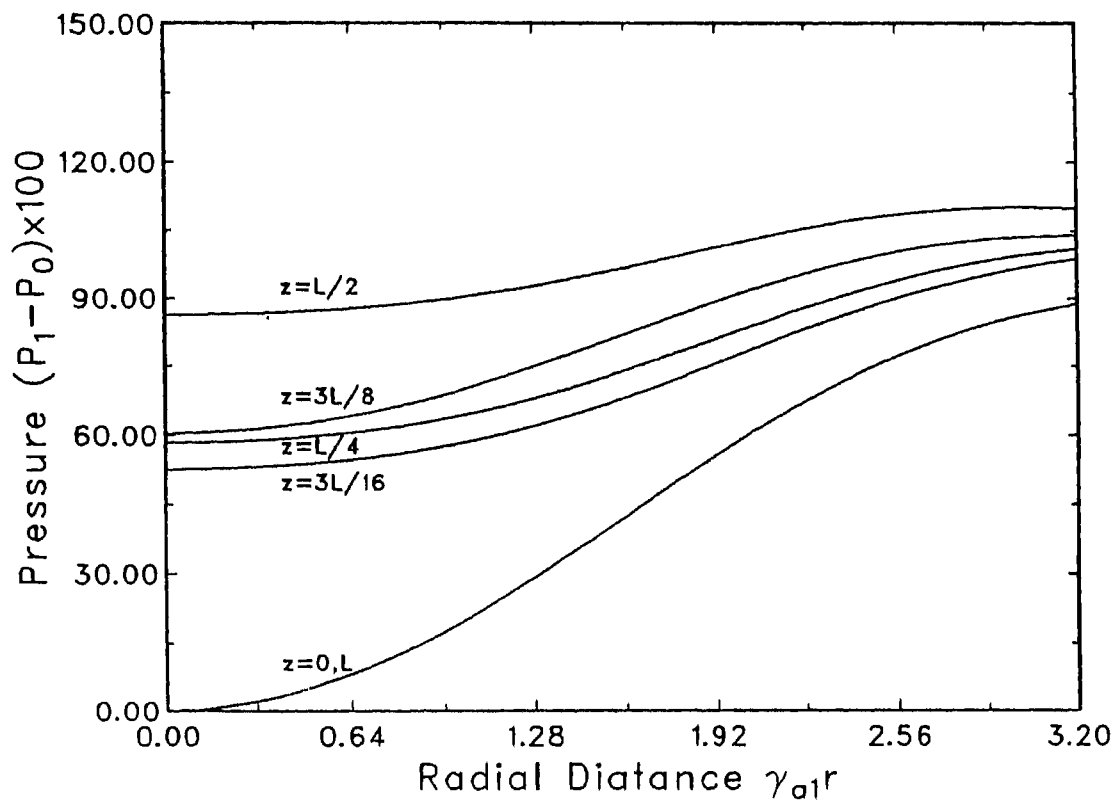
Fig.4.1 Radial Variation of the pressure P_1 for different axial distances Z.

values of axial distance z' [$z'=(z/L) \times 10$]. P_0 is the value of pressure at the origin. The plot indicates that the pressure or temperature at any height increases along the radius towards the surface. The radial variation of pressure is the maximum at the foot points of the loop and it is minimum at the apex. This is in conformity with the result of Levine and Withbroe(1977), who have established that the coronal loops undergoing dynamic changes are characterized by a temperature structure in which there is a cool core relative to the substantially hot surrounding sheath.

4.3.2 AXIAL VARIATION OF PRESSURE:

Figure 4.2 is a plot of pressure (P_1-P_0) against the axial distance z' for various values of $(\gamma_a r)$. The plot indicates that the axial variation, of the pressure is maximum at the axis and minimum at the surface. The maximum value of the pressure is attained near the apex for all values of $(\gamma_a r)$. This is in agreement with the results of Rosner et al.(1978).

4.3.3 RADIAL VARIATION OF PRESSURE AT DIFFERENT AZIMUTHAL ANGLES:

Figure 4.3 is the plot of radial variation of pressure for
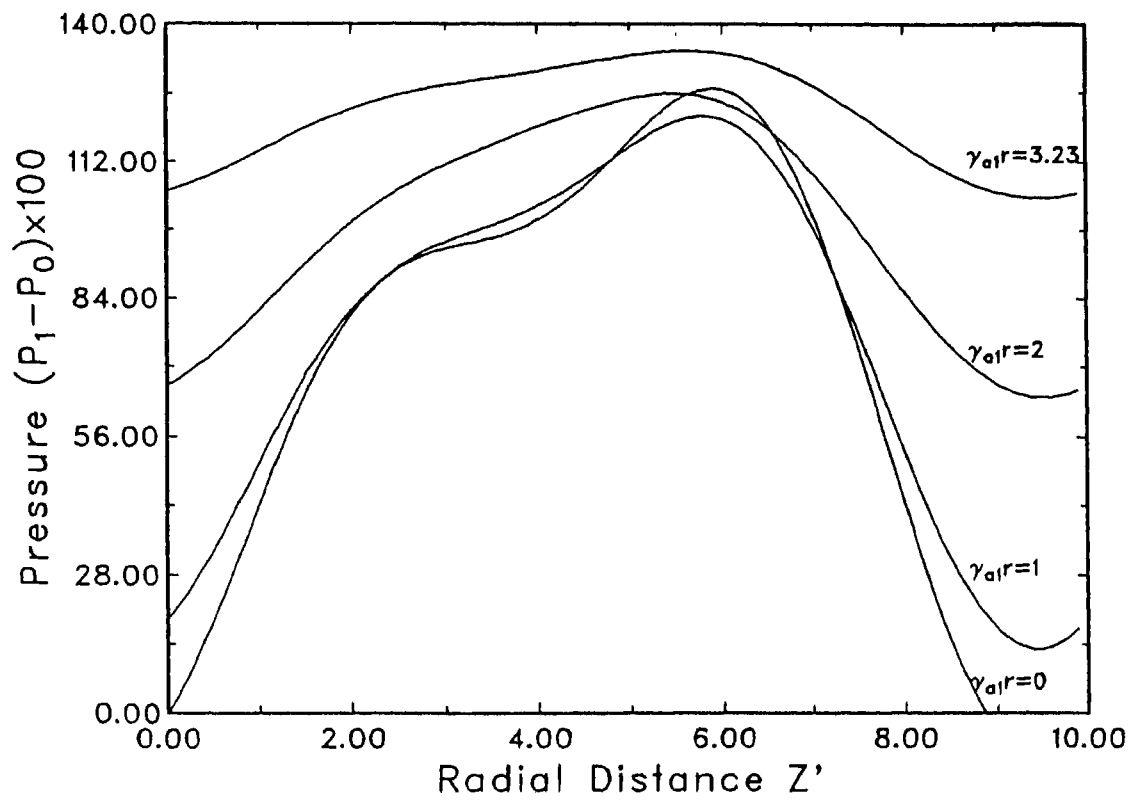
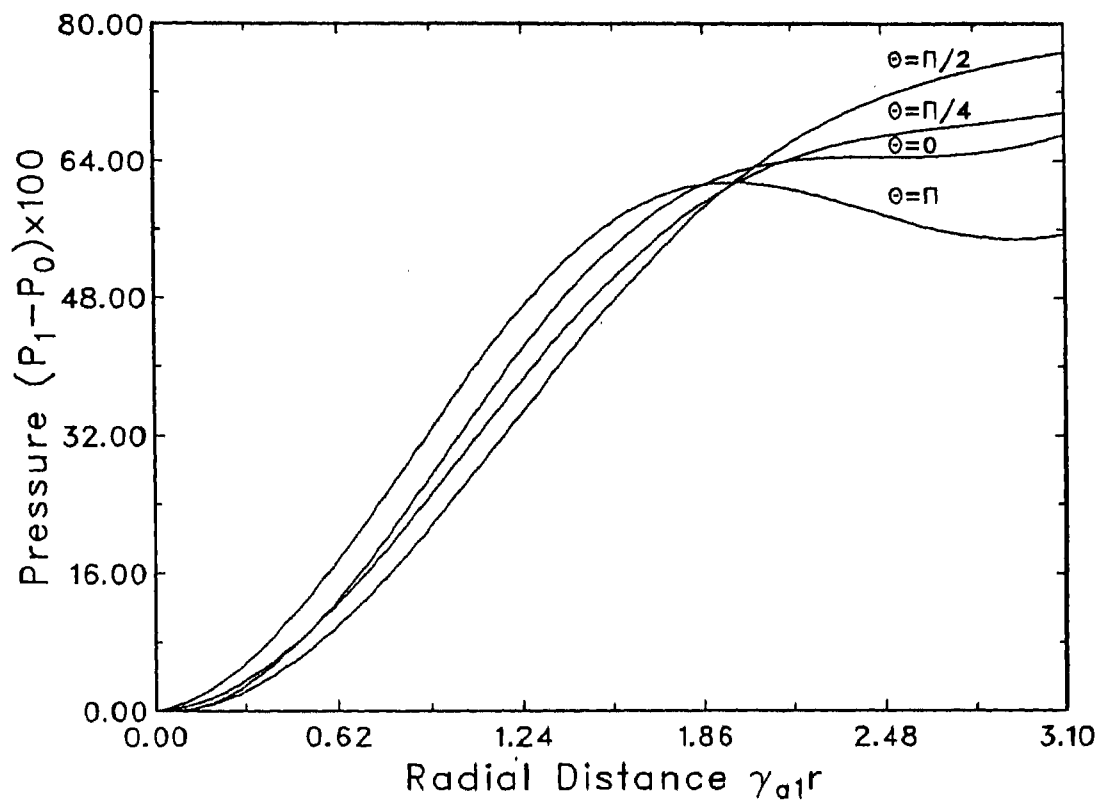**Fig.4.2.** Axial variation of pressure P_1 for different radial distances γ_{ar}.

Fig. 4.3. Radial variation of pressure P_1 for different azimuthal angles θ.

different azimuthal angles $\theta = 0, \pi/4, \pi/2,$ and π when the pressure is averaged over z. The pressure is found to increase uniformly for all values of $\gamma_a r \leq 2.0$. The dependence of the pressure on the azimuthal angle is significant for $\gamma_a r > 2$.

4.3.4 AZIMUTHAL VARIATION OF PRESSURE AT DIFFERENT RADIAL DISTANCES:

Figure **4.4** is a plot of the azimuthal variation of the pressure for different values of $\gamma_a r > 2.0$. The plot indicates that the pressure exhibits an oscillatory behavior which is predominant near the surface.

4..3.5 CONTOUR AND DENSITY PLOT:

Figure 4.5 is a contour plot of pressure as a function of the radial distance $\gamma_a r$ and azimuthal distance z' when the pressure is averaged over θ..

Figure **4.6a** and **4.6b** are the density plots of the pressure as a function of radial distance $\gamma_a r$ and azimuthal distance z' when θ is averaged over a full cycle. In the plot the darker shade squares correspond to minimum pressure regions, while
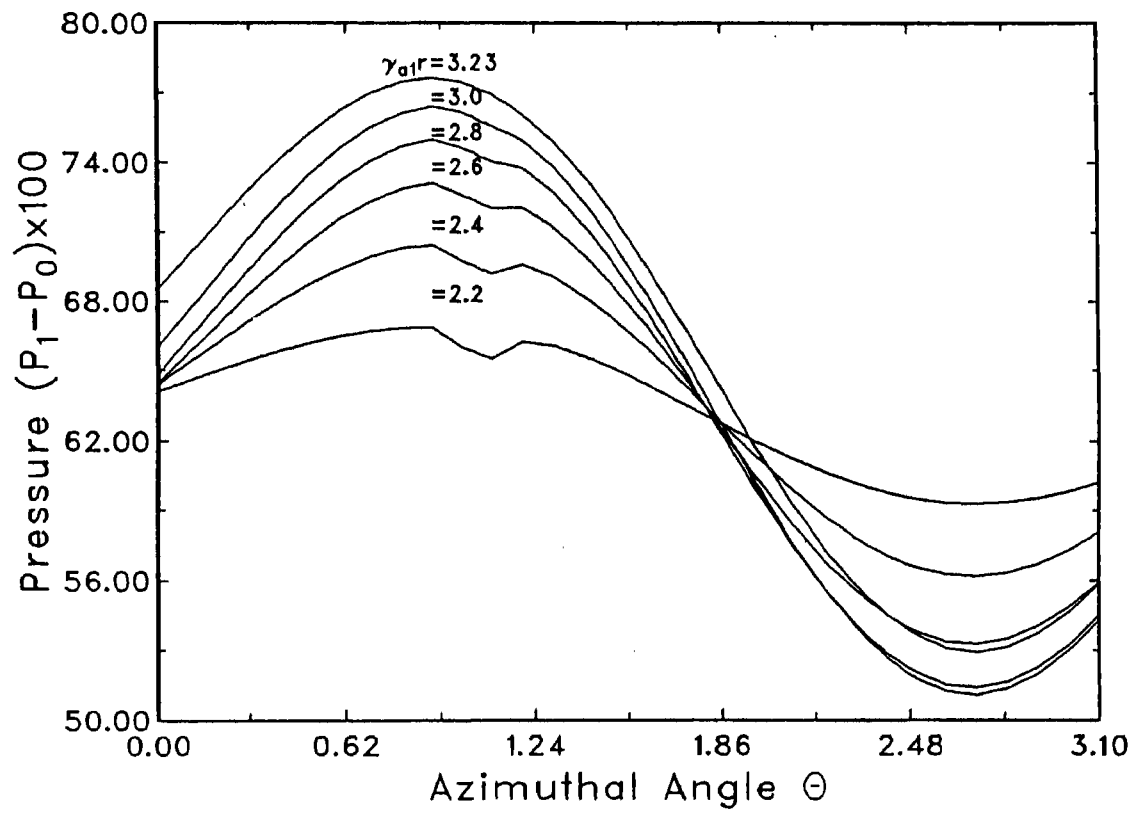
Fig. 4.4. Azimuthal variation of pressure P_1 for different $\gamma_{a1} r$ values.
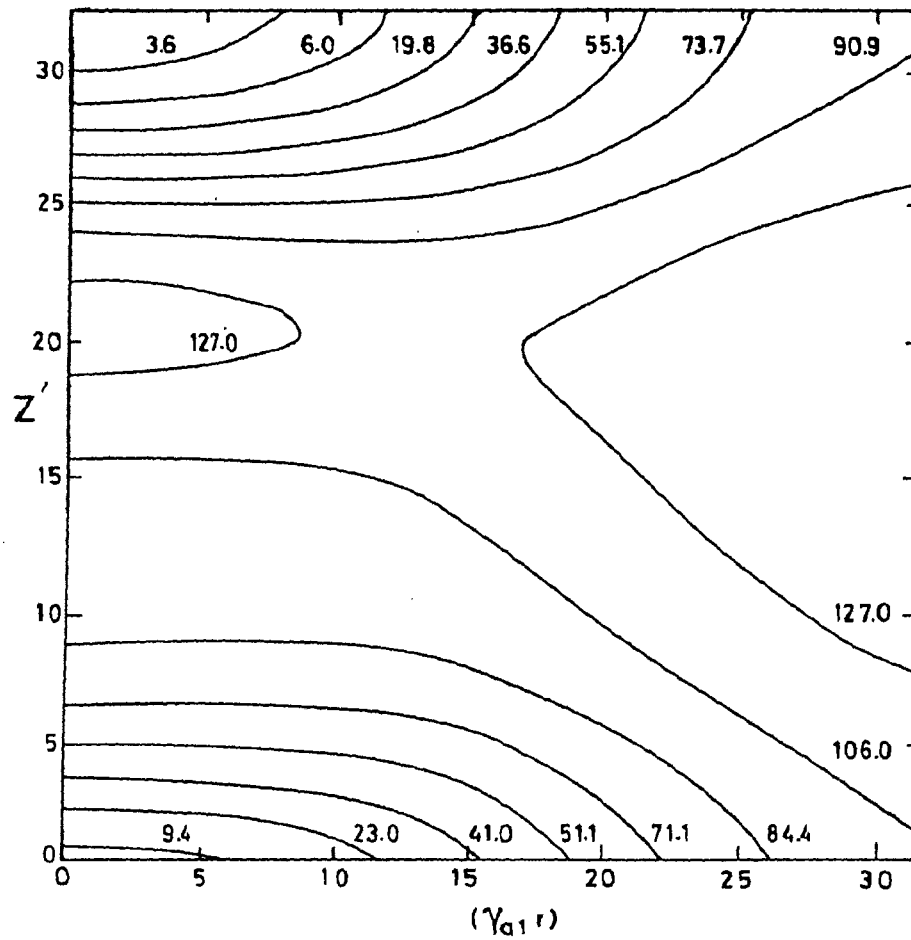
86

Fig.4.5. Contour plot of the pressure P_1 as a function of $\gamma_{a1} r$ and z' when θ is averaged. Each unit on the axis corresponds to $\gamma_{a1} r = 0.1$ and $z' = 0.3$.
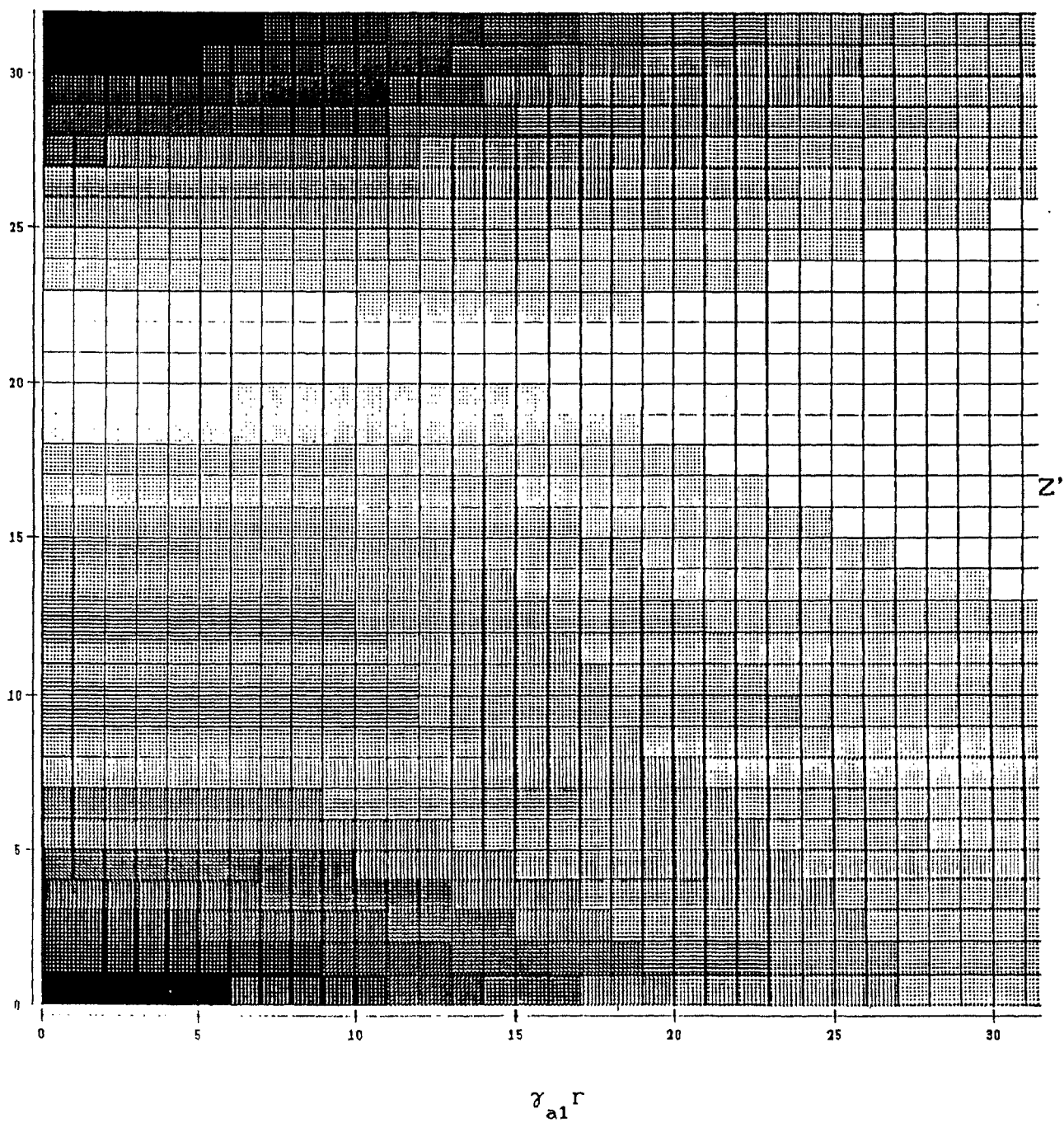
87

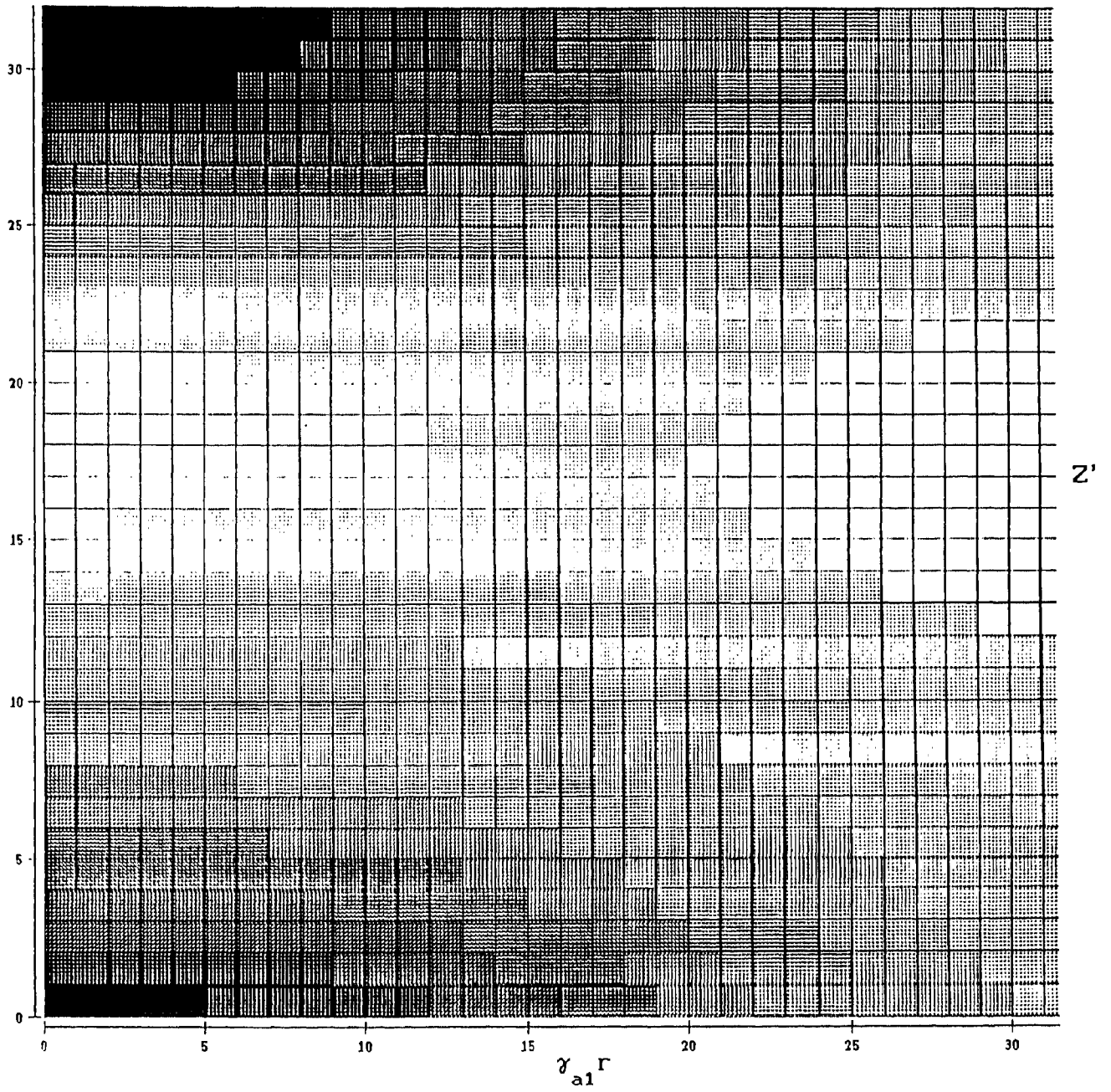**Fig. 4.6a.** Density plot of the pressure P_1 as a function of $\gamma_{a1} r$ & Z'

Fig. 4.6b. Density plot as in fig. 4.6a. but for $\eta_{b1} > \eta_{c1}$.

89

the lighter shade regions correspond to maximum pressure. Figure **4.6a** corresponds to the case of $\eta_{c1} > \eta_{b1}$. It is further observed that the shades become lighter on nearing the apex indicating that the region of maximum pressure exists there.

Figure **4.6b** is the density plot of the pressure as a function of $\gamma_a r$ and z' when $\eta_{b1} > \eta_{c1}$. As compared with the previous case of $\eta_{c1} > \eta_{b1}$ the region of maximum pressure is found to have moved up. The density plot indicates that the region of maximum pressure need not necessarily be at the apex.

CASE 2 PRESSURE STRUCTURE P_2 FOR THE TRIADS $a_2 = (0,0), b_2 = (1,1),$

and $c_2 = (-1,-1)$:

Consider the pair of triads $a_2 \equiv (0,0)$, $b_2 \equiv (1,1)$, $c_2 \equiv (-1,-1)$, which represent the largest spatial scale and satisfy the condition $a = b + c$. The values $|\eta_{a2}| = 2 \times 10^7$, $|\eta_{b2}| = 8 \times 10^6 = |\eta_{c2}|$ obtained from the inequality **(4.29)** satisfy the condition for pump approximation

90

4.4.1 RADIAL VARIATION:

Figure **4.7a** is the plot of radial variation of pressure P_2 for $\theta = \pi/4$ at different axial positions. Unlike the case of P_1 (Figure **4.1**)where the maximum pressure was noticed at the foot points, in this case the maximum pressure as well as the maximum variation in pressure both are at $z=L/4$.

Figure **4.7b** is the plot of radial variation of pressure P_2 for $\theta = 3\pi/4$and for different axial distances z= 0, L/4, L/2 and L. The maximum pressure as well as the maximum variation in pressure is found to be at the foot points,in sharp contrast to the case for $\theta = \pi/4$.where it was found to be at one fourth the height of the cylinder i.e.at z = L/4

4.4.2 AXIAL VARIATION:

Figure **4.8** is a plot of the axial variation of pressure P_2 for the azimuthal angle $\theta=\pi/4$ and for different radial distances $\gamma_a r = 0,\ 0.72,$ and 1.44 . The pressure shows an oscillatory behavior at the axis of the loop more predominantly than near the surface.

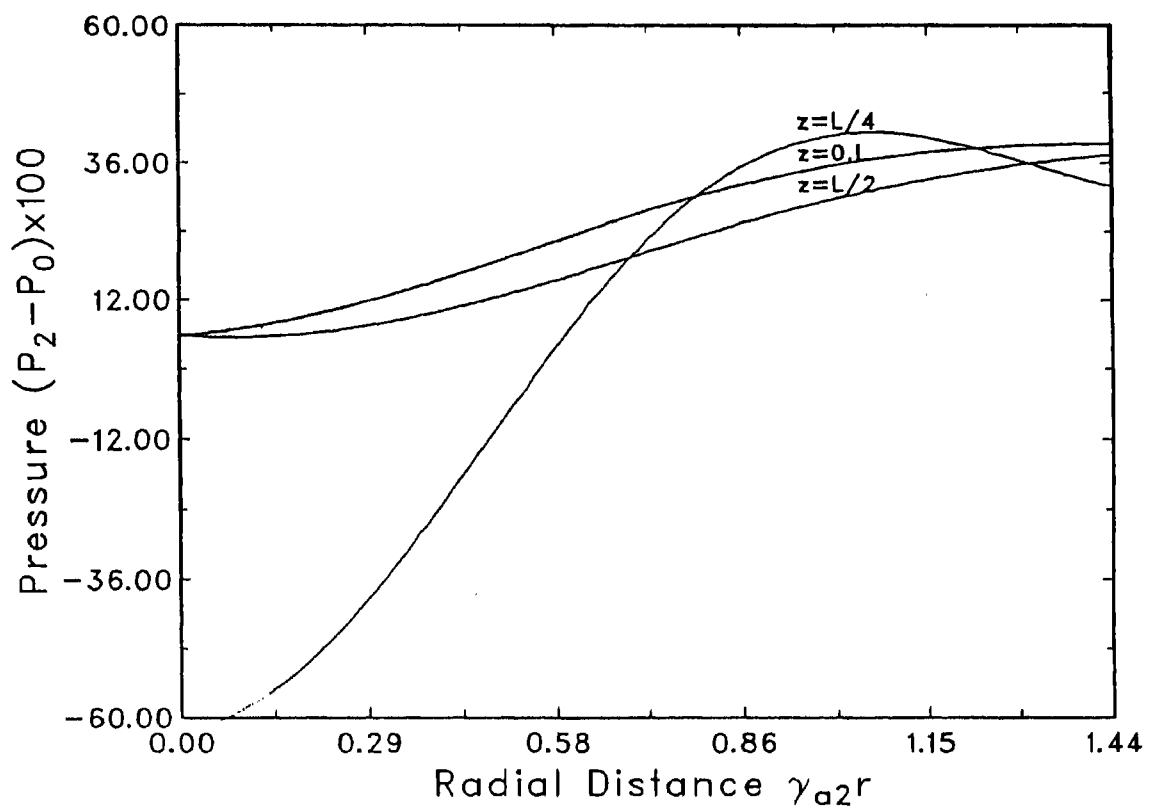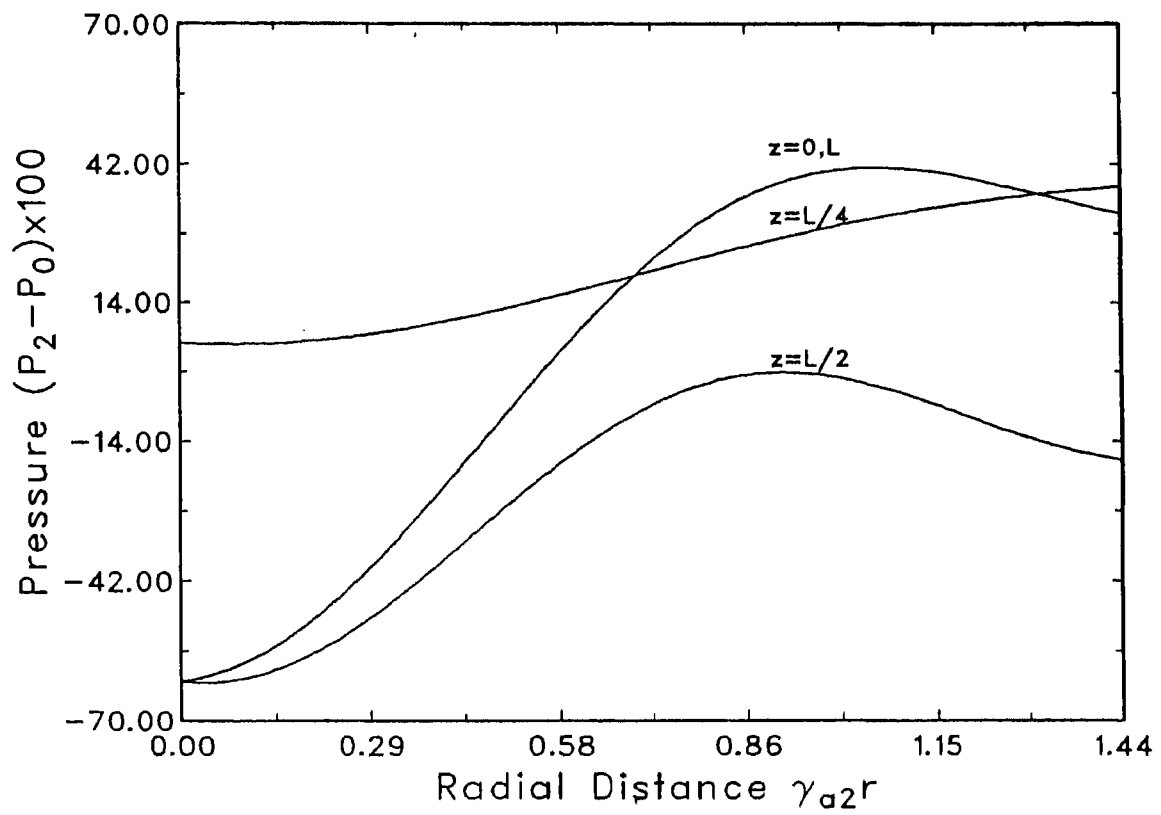**Fig. 4.7a.** Radial variation of pressure P_2 for $\theta=\pi/4$ at different axial distances.

Fig. 4.7b. Radial variation of pressure P_2 for $\theta = 3\pi/4$ at different axial distances.
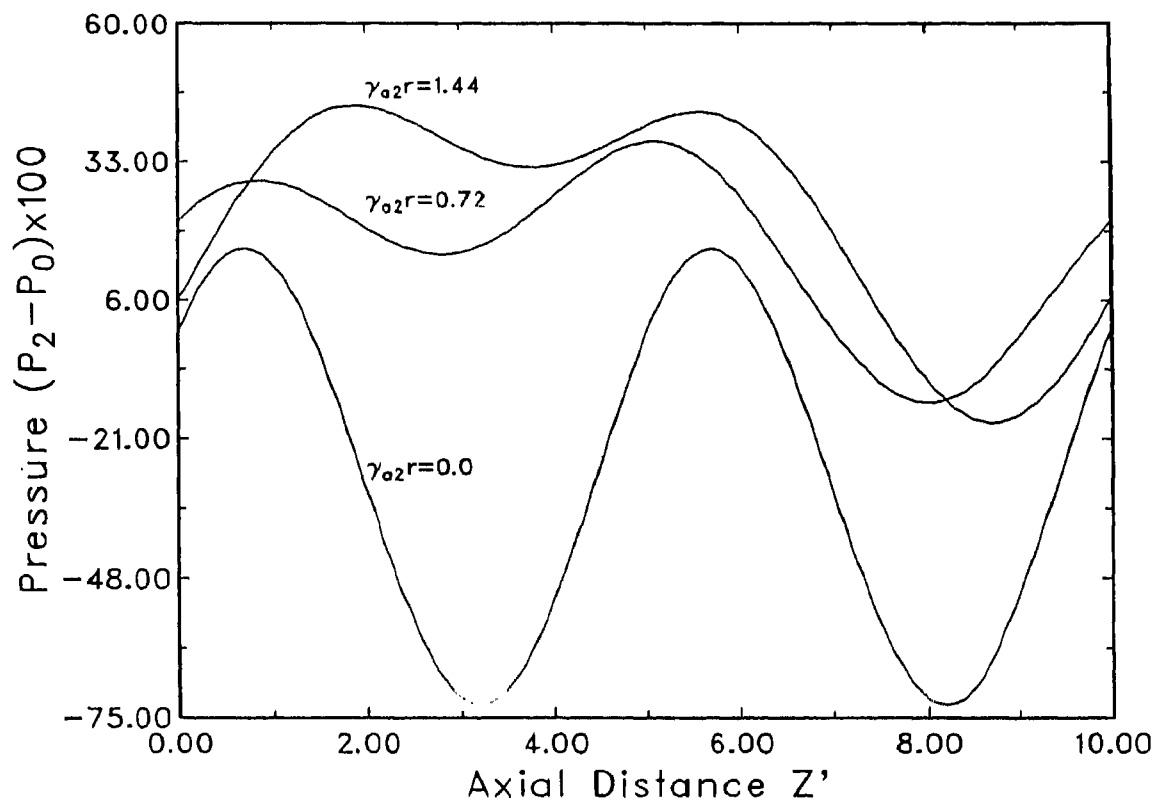
Fig.4.8. Axial variation of pressure P_2 for $\theta = \pi/4$ at different radial distances.

94

4.4.3 AZIMUTHAL VARIATION:

Figure **4**.9 is the azimuthal variation of the pressure P_2 at the apex of the loop for different radial distances from the axis. The behavior of pressure is oscillatory and the maximum value is attained at the boundary.

4.5 MODE STRENGTHS VARYING IN PROPORTION TO THEIR SPATIAL SCALES:

CASE 1: PRESSURE STRUCTURE P_1 FOR THE TRIADS $a_1 = (1,1)$, $b_1 = (1,0)$ and $c_1 = (0,1)$:

This is the second of the physical considerations in which the mode strengths are assumed to vary in proportion to their spatial scales. It is assumed that the mode with the largest spatial scale may be the strongest. For the set of triads chosen a $=(1,1)$, b $=(1,0)$ the spatial scale in the z' direction is same and is smaller than that of the mode c $= (0,1)$. In this case 'a' and 'b' are assumed to be of equal strength and less than the strength of 'c'. So that

$$\lambda_a^2 \eta_a^2 = \lambda_b^2 \eta_b^2 \quad \text{and} \quad \lambda_a^2 \eta_a^2 < \lambda_c^2 \eta_c^2$$
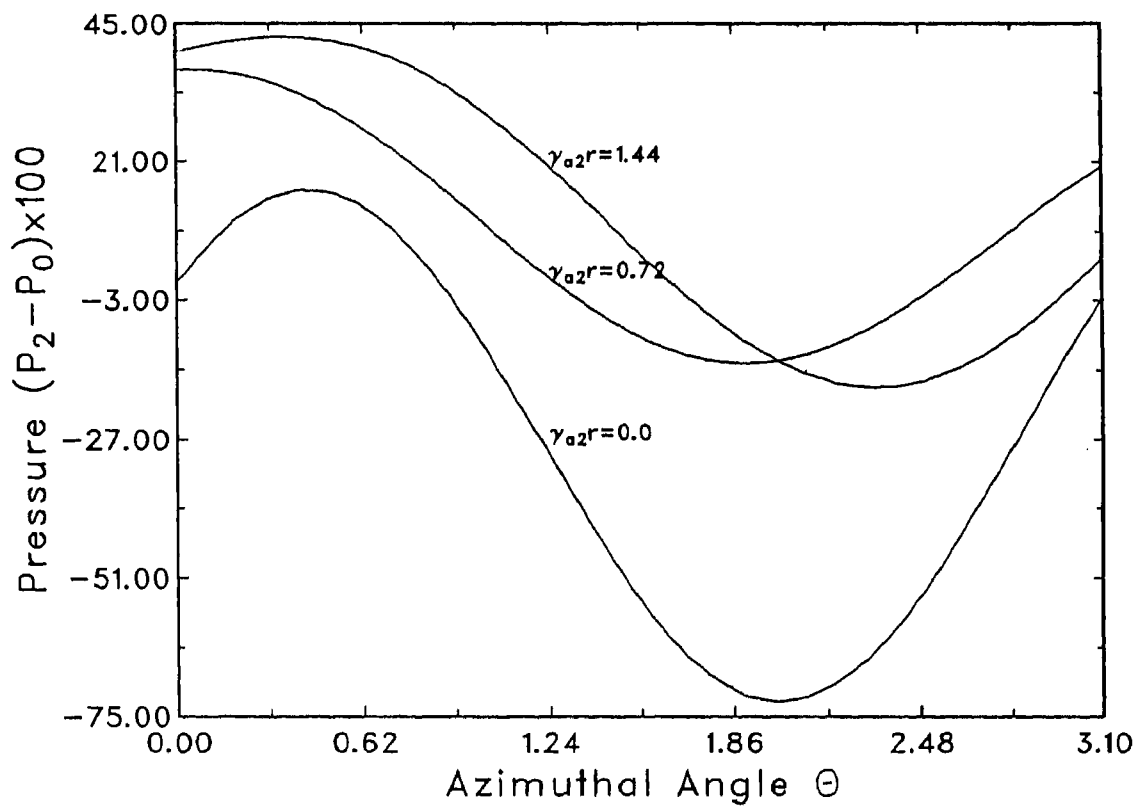
95

Fig.4.9. Azimuthal variation of the pressure P_2 for different radial distances.

Choose $|\eta_a| = 10^7$, $|\eta_b| = 8.4 \times 10^6$ and $|\eta_c| = 1.6 \times 10^7$,

so that the conditions prescribed in equation (4.29) are satisfied.

4.5.1 RADIAL VARIATION:

Figure **4.10** is the radial variation of pressure for different axial positions. The pressure and hence the temperature at any height increases along the radius towards the surface. The radial variation of. pressure is maximum at the foot points of the loop and is minimum at the apex, for z=0 and L. This result is similar to the pump approximation case for the same triads, (Ref. Figure4.1). However, for other values of Z', the pressure tends to decrease initially and after a certain radial distance, increases monotonically. This is contrary to the pressure profile indicated in Figure4.1, where there is a monotonic increase of pressure for all values of Z'.

4.5.2 AXIAL AND AZIMUTHAL VARIATION:

Figure **4.11** is a plot of the axial variation of pressure. with axial distances at different radial positions, and **4.12** is the

250.00

Pressure $(P_1-P_0)\times100$

200.00

z=0.58L

z=L/2

z=3L/8

150.00

z=L/4

z=3L/16

100.00

50.00

z=0,L

0.00

0.00   0.64   1.28   1.92   2.56   3.20
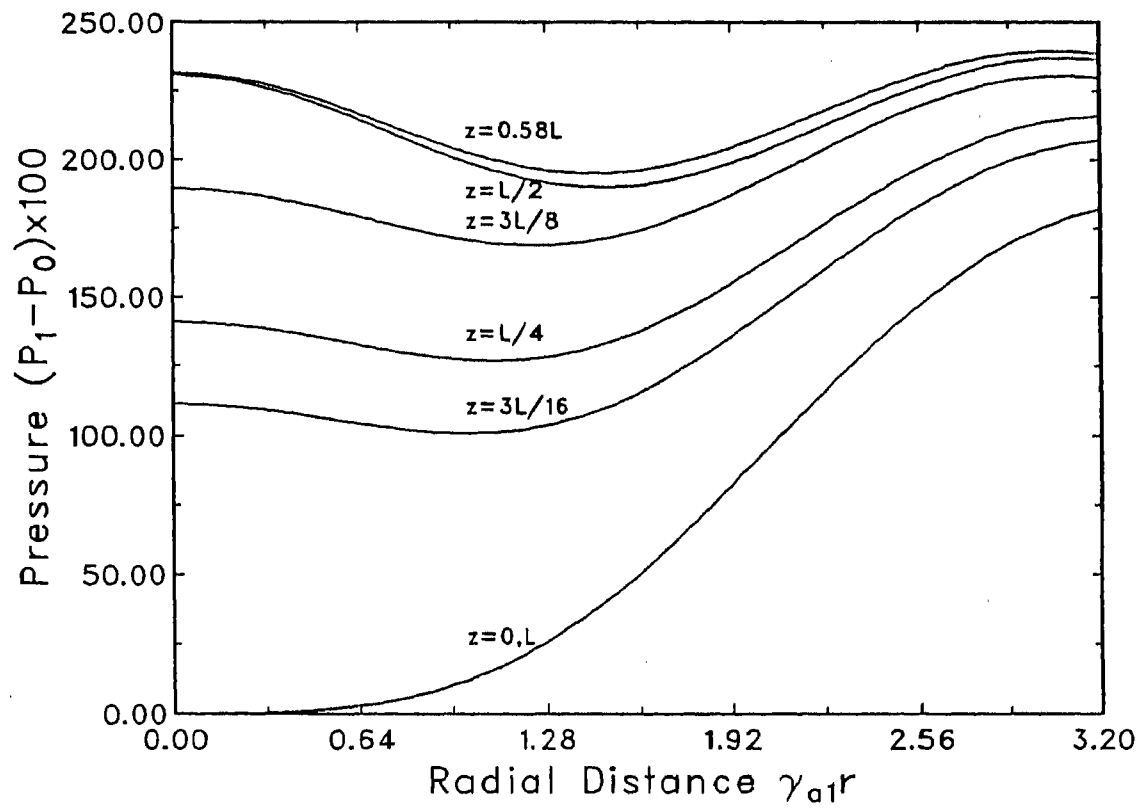
Radial Distance $\gamma_{a1}r$

Fig.4.10. Radial variation of pressure for different
axial distances. Same as fig.4.1 but for $\eta_{c1} > \eta_{a1}$.
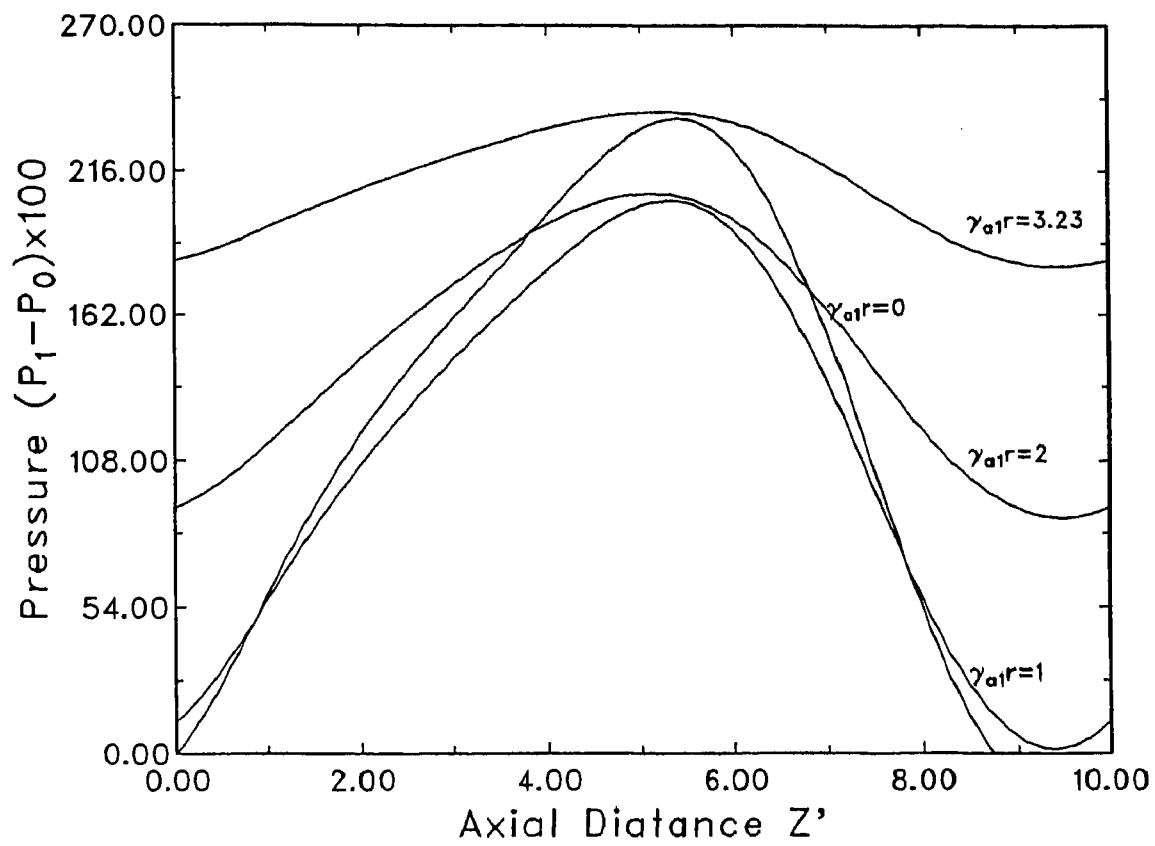
Fig. 4.11. Axial variation of the pressure for different radial distances. Same as fig4.2 but for $\eta_{c1} > \eta_{a1}$.
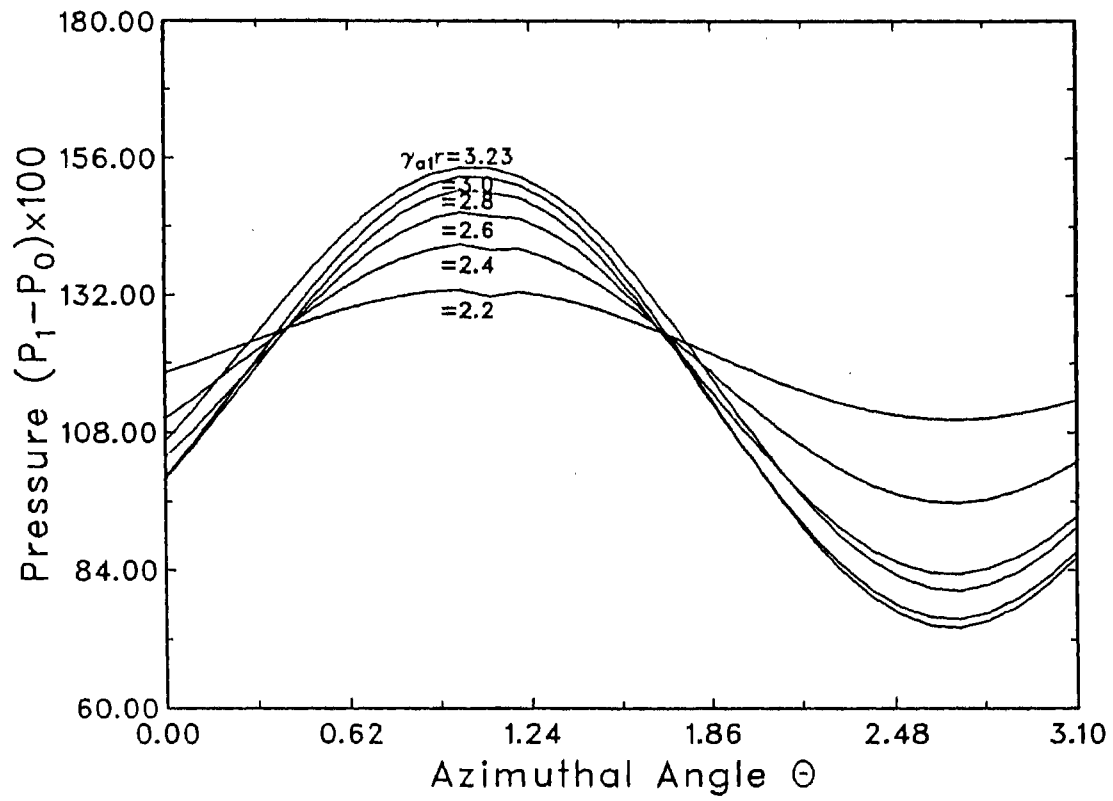
Fig.4.12. Azimuthal variation of pressure for different radial distances. Same as fig4.4 but for η_{c1} $> \eta_{a1}$.

radial variation of pressure for different azimuthal angles. The results in both the cases are more or less comparable to that obtained in the pump approximation case (Figure **4.2** and **4.3**).

CASE 2: PRESSURE STRUCTURE P_2 FOR THE TRIADS $a_2 = (0,0)$, $b_2 = (1,1)$ and $c_2 = (-1,-1)$:

In this case the mode $a \equiv (0,0)$ corresponds to the largest spatial scale and therefore if this is assumed to be stronger than the other two modes. This leads to the conditions $\lambda_a^2 \eta_a^2 > \lambda_b^2 \eta_b^2$ and $\lambda_a^2 \eta_a^2 > \lambda_c^2 \eta_c^2$ which are identical to the pump approximation case for the triads (a, b, c). The pressure profile is therefore similar to the one in Figures **4.7**, **4.8** and **4.9**.

4.6 SUMMARY:

The representation of velocity and magnetic fields by a three mode Chandrasekhar-Kendall functions, brings out the three dimensional features of the pressure profile. The choice of the triads representing the variations of velocity and magnetic fields

on the largest spatial scales permitted by the system, provides a fairly realistic description of the loop plasma. Though the pressure structure is a strong function of the relative amplitudes of the modes, the trends, like an increase of pressure towards the surface and the existence of maximum somewhere along the length of the loop emerge as the general features. The superposition of C-K functions has produced results which are in general agreement with the observed cool core and hot sheath features of the coronal loops. However the discussion in this chapter were purely restricted to the spatial variation of pressure. An attempt at the study of temporal evolution has been made and the same is discussed in the next chapter.

5 TEMPORAL EVOLUTION OF PRESSURE IN SOLAR CORONAL LOOPS

5.1 INTRODUCTION:

As already mentioned coronal loops are dominant structures in the higher levels of the solar atmosphere and they exhibit stable and well configured geometry inspite of the magnetic and velocity field fluctuations in plasma. Such a steady state is the result of various manifestations of the balance of inertial and magnetic forces. The structure of the velocity and magnetic fields plays a pivotal role in determining the heating, stability and evolution of the plasma in coronal loops (Athay and Klimchuk, 1987; Priest, 1982; Krishan, 1983 and 1985). In the previous chapter the steady state structure of the pressure of the loop plasma was delineated using Chandrasekhar-Kendall representation of the velocity and magnetic fields. This was done under the steady state assumption and therefore no information on the temporal behavior of the fields and of the pressure could be derived.

In this chapter the study is extended to include time

dependence of velocity, magnetic field and pressure and thereby study their evolution. As before, the dynamics of the velocity and magnetic fields are studied using the MHD equations and Chandrasekhar-Kendall representation. The complete dynamics is described by a set of infinite coupled and nonlinear ordinary differential equations which are of the first order in time for the expansion coefficients of the velocity and magnetic field. Since the evolution equations are coupled and nonlinear , the dependence of their solution on the initial conditions is expected to reveal chaotic behavior. Towards this end, an investigation is done on the existence of chaos in the evolution of pressure in coronal loops by studying the power spectrum of the data generated by the solution of the MHD equations and by evaluating the invariant dimension especially the second order correlation dimension of the attractor D_2 of the system.

The representation of the fields by the superposition of the three lowest order C-K functions reduces the system to a set of six equations, three for velocity and three for magnetic field. Analytical solutions can be arrived at in two simplified cases:
(1) when the system is disturbed linearly from its state of equilibrium, and,
(2) when one of the three modes has an amplitude much larger than the other two, referred to as the pump approximation.

In the first case, it is found that the disturbed fields undergo sinusoidal oscillations with a period which is a function of the equilibrium amplitudes of the three modes. This may be one of the ways of explaining the quasi-periodic oscillations observed in the X-ray, microwave and EUV emissions from the coronal loops (Aschwanden, 1987; Svestka, 1994 and references therein).

In the second case, for special values of the initial amplitudes, the system exhibits sinusoidal oscillations. However under general initial conditions, the velocity and magnetic fields go through periods of growth, reversal, decay and saturation in an apparently random manner.

In the most general case, with arbitrary initial conditions, the set of six equations can be solved numerically. The velocity and magnetic fields show a rather complex temporal structure which can be interpreted on the basis of chaotic phenomena. The evidence of chaos is established by evaluating the invariant-dimension, especially the second order correlation dimension of the attractor D_2 of the system. A fractal value for D_2 indicates the existence of deterministic chaos. In evaluating the invariant dimension the following informations are obtained:
(a) Is there an attractor and if there exists one, is it regular or strange?

(b)Is there only a single attractor or are there more than one?

(c)What is the embedding dimension so that in describing non linear process characterised by the set of given equations, what should be the dimensions of the phase space to describe the dynamics of the system.

The algorithm proposed by Grassberger and Proccacia (1983) has been adopted in this chapter.

5.2. DERIVATION OF THE PRESSURE PROFILE:

As mentioned in the previous chapter the coronal loop plasma is represented by a cylindrical column of length 'L' and radius 'R'. The equations describing an incompressible ideal MHD turbulent plasma in terms of fluid velocity **V** and the magnetic field **B** are:(This section upto equation 5.21 has already been discussed in chapter 4. However,for easy reference the same is being repeated here).

$$\frac{\bar{\nabla} P}{\rho} = \frac{(\bar{\nabla} \times B) \times B}{\rho} - (V.\bar{\nabla})V - \frac{\partial V}{\partial t} \qquad (5.1)$$

106

$$\bar{\nabla} \times (V \times B) - \frac{\partial B}{\partial t} = 0 \qquad\qquad (5.2)$$

where P is the mechanical pressure and ρ is the mass density. The force due to gravity has been neglected. Equations (5.1) and (5.2) preserve in time the constraints

$$\nabla \cdot V = 0 \qquad\qquad (5.3)$$

$$\nabla \cdot B = 0 \qquad \text{and} \qquad\qquad (5.4)$$

$$P = nKT \qquad\qquad (5.5)$$

n is the number density of particles , K is the Boltzmann's constant and T is the temperature. The equations (5.1) to (5.5) form closed set of equations in B, V, ρ and T.

Using the identity

$$(V \cdot \bar{\nabla}) V = (\bar{\nabla} \times V) \times V + 1/2 \; \bar{\nabla} V^2 \; ,$$

equation (5.1) reduces to

$$\bar{\nabla} \ [P/\rho + (1/2)V^2] = \left(\frac{(\bar{\nabla}xB)xB}{\rho} - (\bar{\nabla}xV)xV\right) - \frac{\partial V}{\partial t} \qquad (5.6)$$

In the steady state $\partial V/\partial t = 0$ and for a force free representation of the magnetic field and a Beltrami flow, i.e., for $\bar{\nabla}xB=\alpha B$ and $\bar{\nabla}xV=\alpha V$, we find

$$\bar{\nabla} \ [\ P/\rho + 1/2 \ V^2] = 0 \qquad\qquad (5.7)$$

Equation (5.7) also holds good where there is an equipartition of energy between velocity and magnetic fields, i.e., $|V| = |B|/\rho$.

In cylindrical geometry, with a rigid perfectly conducting, impenetrable wall at a radius $r = R$, the boundary conditions on B and V at $r = R$ are $V_r(r=R)=0$ and $B_r(r=R)=0$. A periodic boundary condition with a period L in the z direction is assumed. Identifying L with the major circumference of a torus enables to include the case of a toroidal boundary with the curvature neglected. The z or the axial direction will be referred as the "toroidal" direction and the θ direction as the "poloidal" direction.

108

Following the procedure adopted by Montgomery et al(1978), the velocity field **V** and magnetic field **B** in the loop plasma are represented by the superposition of Chandrasekhar-Kendall functions. They are eigenfunctions of the curl operator. They are the solutions of the eigenvalue problem $\bar{\nabla} \times \mathbf{a} = \lambda \mathbf{a}$, where λ is real Individually they are force free fields although the sum of two or more of them is not, in general, force free. The complete dynamics can be described by a set of infinite coupled nonlinear ordinary differential equations which are of first order in time for the expansion coefficients of velocity and magnetic fields and it is a formidable task to find solutions to these equations. Hence, the fields are represented by the superposition of the three lowest order C-K functions. Another justification for doing so is that these functions represent the largest spatial scales and therefore may be the most suitable states for comparison with observed phenomena.

The eigen functions of the curl operator can be written as:

$$\mathbf{a}_{(n,m,q)} = \bar{\nabla} \, \psi_{(n,m,q)} \times \hat{e}_z + \left[\nabla \times \nabla \times [\hat{e}_z \psi_{(n,m,q)}] \right] / \lambda_{(n,m,q)}$$

$$(5.8)$$

where $\psi_{(n,m,q)}$ is a solution of the scalar wave equation

109

$$[\nabla^2 + \lambda^2_{(n,m,q)}]\psi_{(n,m,q)} = 0 \qquad\qquad (5.9)$$

$$\psi_{(n,m,q)} = J_m(\gamma_{nmq}r)\,\exp(im\theta + ik_n z) \qquad (5.9a)$$

Where

$$\lambda_{(n,m,q)} = \pm\,(\gamma^2_{nmq} + k^2_n)^{1/2} \qquad\qquad (5.9b)$$

Here, $k_n = 2\pi n/L$, where $n = 0, \pm1. \pm2, \dots$.

The integer m takes on the values $m = 0, \pm1, \pm2, \dots\dots$,
$\gamma_{nmq} > 0$ and is determined as that solution which makes equation
(5.8) satisfy the boundary conditions at $r=R$. $J_m(\gamma_{nmq}r)$ is the
Bessel function. written in detail equation (5.8) is:

$$
\begin{aligned}
\mathbf{a}_{(n,m,q)} = \ & \hat{e}_r\left(\frac{im}{r} + \frac{ik_n}{\lambda_{(n,m,q)}}\frac{\partial}{\partial r}\right)\psi_{(n,m,q)} \\[2mm]
& + \hat{e}_\theta\left(-\frac{\partial}{\partial r} - \frac{mk_n}{r\lambda_{(n,m,q)}}\right)\psi_{(n,m,q)} \\[2mm]
& + \hat{e}_z\left(\frac{\lambda^2_{(n,m,q)} - k^2_n}{\lambda_{(n,m,q)}}\right)\psi_{(n,m,q)} \qquad (5.10)
\end{aligned}
$$

For the inequality $m^2 + n^2 > 0$, the condition $R_r = 0$ at $r = R$, requires

$$Rk_n \, \gamma_{nmq} \, J'_m \, (\gamma_{nmq} R) + m\lambda_{(n,m,q)} J_m (\gamma_{nmq} R) = 0 \qquad (5.11)$$

The eigenvalues for $m = n = 0$ are not determined by the radial boundary condition, since $R_r = 0$ for $n = m = 0$. $\lambda_{(0,0,q)}$ is determined using the fact that for each individual $(0,0,q)$ mode the ratio of the toroidal magnetic flux ψ_t to the poloidal flux ψ_p is

$$\frac{\psi_t}{\psi_p} = - \frac{R}{L} \frac{|\lambda_{(0,0,q)}|}{\lambda_{(0,0,q)}} \frac{J'_0 (\gamma_{00q} R)}{J_0 (\gamma_{00q} R)} \qquad (5.12)$$

Since both ψ_t and ψ_p are constants of the motion, it is natural to determine $\lambda_{(0,0,q)}$ from the equation (5.12) as :

$$\frac{J'_0 (\gamma_{00q} R)}{J_0 (\gamma_{00q} R)} = - \frac{L}{R} \frac{\lambda_{(0,0,q)}}{|\lambda_{(0,0,q)}|} \frac{\psi_t}{\psi_p} \qquad (5.13)$$

for all $q = 1, 2, 3, \ldots \ldots$. $q=1$ is the eigenmode corresponding to the lowest $|\lambda_{(0,0,0)}|$ The choice of equation (5.13) guarantees the orthogonality of all pairs of modes For $n^2+m^2>0$, the modes occur in pairs, so that if λ is an eigen value $-\lambda$ is also one, corresponding to the opposite sign of m or n.

$A_{(n,m,q)}$ is the normalized $a_{(n,m,q)}$ such that,

$$\int d^3x \, \overline{A}^*_{(n,m,q)} \cdot \overline{A}_{(n',m',q')} = \delta_{nn'} \delta_{mm'} \delta_{qq'} \qquad (5.14)$$

$\delta_{nn'} = \delta_{mm'} = \delta_{qq'} = 1$, if $n = n'$, $m = m'$ and $q = q'$, and $= 0$ if n, m and q are not equal to n', m' and q' respectively.

The normalizing constant that relates $\overline{A}_{(n,m,q)}$ to $\overline{a}_{(n,m,q)}$ is given by

$$\overline{A}_{(n,m,q)} = C_{(n,m,q)} \, \overline{a}_{(n,m,q)} \qquad (5.15)$$

Using equation (5.14) in (5.15)

$$\int C^2_{nm} \, a_{nm} \cdot a^*_{nm} \, d^3x = 1 \qquad (5.16)$$

In cylindrical coordinates

$$C^2_{nm} = 1/\int a_{nm} \cdot a^*_{nm} \, r dr \, d\theta \, dz \qquad (5.17)$$

The limits of integration are : $r = 0$ to R, $\theta = 0$ to 2π and $z = 0$ to L.

The values of $\gamma_{11} R$, $\gamma_{10} R$ and $\gamma_{01} R$ are 3.228998 , 3.85

112

and $\underline{3.85.}$ respectively.

And, that of $\lambda_{11}R$, $\lambda_{10}R$ and $\lambda_{01}R$ are $\underline{3.28956}$ $\underline{3.85}$ and $\underline{3.85}$ respectively (Refer Chapter 4).

Using these values of λ's and γ's the normalisation constants are found to be :

$$C_{11} = 2.922 \text{ L}$$
$$C_{01} = 1.0198238 \text{ L}$$
$$C_{10} = 0.1278097 \text{ L}$$

The magnetic field B and the velocity field V can be expanded in terms of the C-K function as:

$$B = \sum_{nmq} \xi_{(n,m,q)} \; \lambda_{(n,m,q)} \; A_{(n,m,q)} \qquad (5.18)$$

$$V = \sum_{nmq} \eta_{(n,m,q)} \; \lambda_{(n,m,q)} \; A_{(n,m,q)} \qquad (5.19)$$

where η's and ξ's are the expansion coefficients and are functions of time. Since B and V are real, by symmetry condition the expansion coefficients $\xi_{(n,m,q)}$ and $\eta_{(n,m,q)}$ must be such that

113

$\xi_{(n,m,q)} = \xi_{(-n,-m,-q)}$ so that $\xi_{(0,0,q)}$ and $\eta_{(0,0,q)}$ are real

for all values of q. In the truncated triple mode system

$$V = \lambda_a \eta_a(t) A_a + \lambda_b \eta_b(t) A_b + \lambda_c \eta_c(t) A_c \qquad (5.20)$$

$$B = \lambda_a \xi_a(t) A_a + \lambda_b \xi_b(t) A_b + \lambda_c \xi_c(t) A_c \qquad (5.21)$$

η's and ξ's are in general complex.

The functions a_{nm} satisfy $\nabla \times a_{nm} = \lambda_{nm} a_{nm}$.

γ_{nm} have been determined from the boundary conditions for a perfectly conducting and rigid boundary since the observations do show very well defined loop structures aligned with the magnetic field across which there is little or no transport. Thus the radial component of the velocity and the magnetic field vanish at the surface $r = R$.

The dynamics can be described by taking the inner products of curl of equations of (5.1) and (5.2) with A_{nm}^* and integrating over the volume. The resulting six complex, coupled, non-linear ordinary differential equations are:

114

5.2.1. DERIVATION OF THE DYNAMICAL EQUATIONS:

Equation (5.1) is, $\dfrac{\partial V}{\partial t} + (V.\nabla)V = -\nabla P + (\nabla \times B) \times B$

Taking curl on both sides and rewriting,

$$\nabla \times \dfrac{\partial V}{\partial t} = -\nabla \times (V.\nabla)V - \nabla \times \nabla P + \nabla \times (\nabla \times B) \times B \qquad (5.1a)$$

$$\nabla \times \dfrac{\partial V}{\partial t} = \nabla \times \dfrac{\partial}{\partial t}[\lambda_a \eta_a A_a + \lambda_b \eta_b A_b + \lambda_c \eta_c A_c]$$

$$= \lambda_a^2 \dfrac{\partial \eta_a}{\partial t} A_a + \lambda_b^2 \dfrac{\partial \eta_b}{\partial t} A_b \quad \lambda_c^2 \dfrac{\partial \eta_c}{\partial t} A_c \quad [\text{Using } \nabla \times A = \lambda A]$$

Dot multiply by A_a^* and integrate over the volume. Taking $\int A^*.(A_b \times A_c)d^3r = I$ and using $\nabla \times A = \lambda A$,

$$\int [\nabla \times \dfrac{\partial V}{\partial t}].A_a^* \ d^3r = \lambda_a^2 \dfrac{\partial \eta_a}{\partial t} \qquad (5.1b)$$

$$(\nabla \times B) \times B = [\nabla \times (\lambda_a \xi_a A_a + \lambda_b \xi_b A_b + \lambda_c \xi_c A_c)] \times$$
$$(\lambda_a \xi_a A_a + \lambda_b \xi_b A_b + \lambda_c \xi_c A_c)$$

115

Dot multiplying by $\mathbf{A}^*$ and integrating over the volume

$$\int [(\nabla\times B)\times B].\mathbf{A}_a^* d^3r \;=\; \nabla \times [\lambda_b^2\lambda_c\xi_b\xi_c - \lambda_c^2\lambda_b\xi_b\xi_c]\int (\mathbf{A}_b\times\mathbf{A}_c).\mathbf{A}_a^* \; d^3r$$

$$= \nabla \times [\lambda_b^2\lambda_c\xi_b\xi_c - \lambda_c^2\lambda_b\xi_b\xi_c]\int \; I\mathbf{A}_a.\mathbf{A}_a^* \; d^3r$$

$$= [\lambda_b^2\lambda_c\xi_b\xi_c - \lambda_c^2\lambda_b\xi_b\xi_c] \; I \; \lambda_a\int \mathbf{A}_a.\;\mathbf{A}_a^* \; d^3r$$

$$\int [(\nabla\times B)\times B].\mathbf{A}_a^* d^3r \;=\; \lambda_a\lambda_b\lambda_c \; [\lambda_b-\lambda_c] \; I \; \xi_b\xi_c \qquad\qquad (5.1c)$$

Using, $(V.\nabla)V = -V \times (\nabla\times V) + 1/2\nabla V^2$

Taking the curl on both the sides $\nabla\times (V.\nabla)V = \nabla\times(-V \times (\nabla\times V))$

$$\nabla \times (V\times (\nabla\times V)) = \nabla \times (\lambda_a\eta_a\mathbf{A}_a + \lambda_b\eta_b\mathbf{A}_b + \lambda_c\eta_c\mathbf{A}_c) \times$$

$$(\nabla\times \lambda_a\eta_a\mathbf{A}_a + \lambda_b\eta_b\mathbf{A}_b + \lambda_c\eta_c\mathbf{A}_c)$$

Dot multiplying with $\mathbf{A}_a^*$ and integrating over the volume,

$$\int [V\times (\nabla\times V)].\mathbf{A}_a^* d^3r \;=\; \lambda_a\lambda_b\lambda_c\eta_b\eta_c I(\lambda_c - \lambda_b) \qquad\qquad (5.1d)$$

Combining equations (5.1b),(5.1c) and (5.1d) and using,

$$\nabla \times \nabla P = 0$$

$$\lambda_a^2 \frac{\partial \eta_a}{\partial t} = \lambda_a \lambda_b \lambda_c \ [\lambda_b - \lambda_c] \ I \ \xi_b \xi_c + \lambda_a \lambda_b \lambda_c \eta_b \eta_c I (\lambda_c - \lambda_b)$$

$$\frac{\partial \eta_a}{\partial t} = \frac{\lambda_b \lambda_c}{\lambda_a} \ [\lambda_b - \lambda_c] \ I \ [\xi_b \xi_c - \eta_b \eta_c] \qquad\qquad (5.1e)$$

Equation **(5.1e)** is same as **(5.22)**.   Similarly other equations **(5.23)** and **(5.24)** can be derived.

Equation **(5.2)** rewriten is, $\dfrac{\partial B}{\partial t} = \nabla \times (V \times B)$

$$\nabla \times (V \times B) = \nabla \times \left[\lambda_a \eta_a A_a + \lambda_b \eta_b A_b + \lambda_c \eta_c A_c \right] \times$$

$$\left[\lambda_a \xi_a A_a + \lambda_b \xi_b A_b + \lambda_c \xi_c A_c \right]$$

$$= \nabla \times \Bigg[\left[\lambda_a \lambda_b \eta_a \xi_b (A_a \times A_b) - \lambda_a \lambda_b \eta_b \xi_a (A_a \times A_b) \right] +$$
$$\left[\lambda_a \lambda_c \eta_a \xi_c (A_a \times A_c) - \lambda_a \lambda_c \eta_c \xi_a (A_a \times A_c) \right]$$
$$\left[\lambda_b \lambda_c \eta_b \xi_c (A_b \times A_c) - \lambda_b \lambda_c \eta_c \xi_b (A_b \times A_c) \right] \Bigg]$$

117

Dot multiply by $\mathbf{A}_a^*$ and integrate over the volume. Taking $\int \mathbf{A}^*.(\mathbf{A}_b \times \mathbf{A}_c)d^3r = I$ and since, $\nabla \times \mathbf{A} = \lambda \mathbf{A}$

$$\int [\nabla \times (\mathbf{V} \times \mathbf{B})].\mathbf{A}_a^* \, d^3r = \lambda_b \lambda_c \left[\eta_b \xi_c - \eta_c \xi_b \right] \lambda_a I \qquad (5.2a)$$

Dot multiplying the LHS by $\mathbf{A}_a^*$ and integrating

$$\int \frac{\partial \mathbf{B}}{\partial t}.\mathbf{A}_a^* \, d^3r = \frac{\partial}{\partial t} \left[\int \lambda_a \xi_a \mathbf{A}_a.\mathbf{A}_a^* \, d^3r + \int \lambda_b \xi_b \mathbf{A}_b.\mathbf{A}_a^* \, d^3r + \right.$$
$$\left. \int \lambda_c \xi_c \mathbf{A}_c.\mathbf{A}_a^* \, d^3r \right]$$

$$= \frac{\partial}{\partial t} \lambda_a \xi_a \qquad (5.2b)$$

combining equations (5.2a) and (5.2b)

$$\frac{\partial \xi_a}{\partial t} = \lambda_b \lambda_c \left[\eta_b \xi_c - \eta_c \xi_b \right] I \qquad (5.2c)$$

Equation (5.2c) is the same as equation (5.27). Similarly other equations (5.28) and (5.29) can be derived. The ρ in the dynamical equations can be absorbed by using $\xi = \sqrt{\rho}/\xi'$.

$$\frac{d\eta_a}{dt} = \frac{\lambda_b \lambda_c}{\lambda_a} (\lambda_c - \lambda_b) \, I \, [\eta_b \eta_c - \xi_b \xi_c /\rho] \qquad (5.22)$$

118

$$\frac{d\eta_b}{dt} = \frac{\lambda_c \lambda_a}{\lambda_b} \; (\lambda_a - \lambda_c) \; I^*[\eta_c^*\eta_a - \xi_c^*\xi_a/\rho] \tag{5.23}$$

$$\frac{d\eta_c}{dt} = \frac{\lambda_a \lambda_b}{\lambda_c} \; (\lambda_b - \lambda_a) \; I^*[\eta_a\eta_b^* - \xi_b^*\xi_a/\rho] \tag{5.24}$$

$$\frac{d\xi_a}{dt} = \lambda_b \lambda_c \; I \; [\eta_b\xi_c - \eta_c\xi_b] \tag{5.25}$$

$$\frac{d\xi_b}{dt} = \lambda_c \lambda_a \; I^*[\eta_c^*\xi_a - \eta_a\xi_c^*] \tag{5.26}$$

$$\frac{d\xi_c}{dt} = \lambda_a \lambda_b \; I^*[\eta_a\xi_b^* - \eta_b^*\xi_a] \tag{5.27}$$

where $I = \int A_a^* \cdot (A_b \times A_c) \; d^3r$

and, the (n,m) values of the modes (a,b,c) satisfy the condition $n_a = n_b + n_c$ and $m_a = m_b + m_c$. Equation (5.6) with the representation of V and B as given by equation(5.20) and (5.21) can be manipulated to yield:

119

$$\bar{\nabla} \left(\frac{P}{\rho} + \frac{1}{2} \sum_i \sum_j \lambda_i \lambda_j \eta_i \eta_j A_i A_j \right)$$

$$i,j = a,b,c$$

$$= \sum_{\substack{i=a,b,c \\ j=b,c,a}} \lambda_i \lambda_j [\lambda_i - \lambda_j] \left(\frac{\xi_i \xi_j}{\rho} - \eta_i \eta_j \right) (A_i \times A_j)$$

$$- \sum \frac{\partial \eta_i}{\partial t} \lambda_i A_i \qquad \qquad (5.28)$$

The expansion coefficients η_i and ξ_i can be solved numerically from the dynamical equations (5.22) to (5.27) which when substituted in equation (5.28) determines the pressure as a function of space and time.

5.3 DYNAMICAL ASPECTS:

The temporal evolution of the pressure for a cylindrical column of plasma of length "L" and radius "R" and for a toroidal to poloidal magnetic flux, ψ_t/ψ_p ratio of 1/10 is discussed in this section. As mentioned earlier, triads a,b,c are chosen to represent the largest possible spatial scales and also satisfy the

120

condition a = b+c ;   a = (1,1), b = (1,0), c = (0,1).

The values of γ_1 and λ_1 found from the boundary conditions as mentioned earlier are:

$\gamma_a R = 3.23$, $\gamma_b R = 3.85$, $\gamma_c R = 3.85$, and

$\lambda_a R = 3.29$, $\lambda_b R = 3.90$, $\lambda_c R = 3.85$

The total energy of a loop plasma in a given configuration (a,b,c) is given by :

$$E = \sum_{i=a,b,c} \lambda_i^2 \ (\eta_i^2 + \xi_i^2)$$

There is no obvious way of fixing the relative magnitudes of the three modes even though we have some estimates of the total energy of a typical loop. There are two physical situations under which equations (5.22) to (5.27) can be solved analytically.
(1)The linear case, and, (2)The pump approximation.

5.4. THE LINEAR CASE:

In this case the time evolution of the small deviations of

121

the velocity and magnetic fields from their equilibrium values. i.e.,when,

$\eta = \eta_0 + \eta_1$, $\xi = \xi_0 + \xi_1$, and $\eta_1 << \eta_0$, $\xi_1 << \xi_0$ for all modes are supposed. From the equation of state $\eta_0 = \xi_0$.

Assuming both $\eta_1(t)$ and $\xi_1(t)$ to have time dependence through e^{St}, we can obtain a dispersion relation whose solution is:

$$S = \mp i \ |I| \left[\lambda_b^2 \ (\lambda_b - \lambda_c - \lambda_a)^2 |\eta_{b0}|^2 + \lambda_c^2 (\lambda_c - \lambda_a - \lambda_b)^2 |\eta_{c0}|^2 \right.$$

$$\left. - \lambda_a^2 (\lambda_a - \lambda_b - \lambda_c)^2 |\eta_{a0}|^2 \right]^{1/2} \tag{5.29}$$

Thus, the system exhibits marginal stability since the perturbed quantities have sinusoidal oscillations with a period which depends upon the equilibrium values of the fields.

5.4.1 TEMPORAL EVOLUTION OF PRESSURE:

Figure 5.1 is a plot of the temporal evolution of pressure [P(t)] at an axial point of the coronal loop when the initial

122

values of velocity and magnetic field coefficients η_i and ξ_i are very nearly equal. The values of η_i and ξ_i chosen are :

$$|\eta_a| = 1.0, \quad |\eta_b| = 2.0, \quad |\eta_c| = 3.0$$
$$|\xi_a| = 1.1, \quad |\xi_b| = 2.1, \quad |\xi_c| = 3.1$$

Figure 5.2 is a plot of power spectrum corresponding to Figure 5.1. The plot is a discrete spectrum which clearly indicates that the pressure profile has a finite number of frequencies when the magnitude of the velocity and magnetic fields are approximately equal initially. This marginal stability exists only for the time scales for which the linearisation is valid. The skylab, UV and microwave observations do indicate that the loops are in a state of quasi periodic pulsations. (Aschwanden 1987)

5.5 PUMP APPROXIMATION:

In the pump approximation one of the three modes is taken to be the strongest. For example, here, since the conservation condition requires a = b + c, we can take 'a' to be the dominant mode and call it the pump which shares its energy with the other two modes. The time evolution of the two weaker modes does not
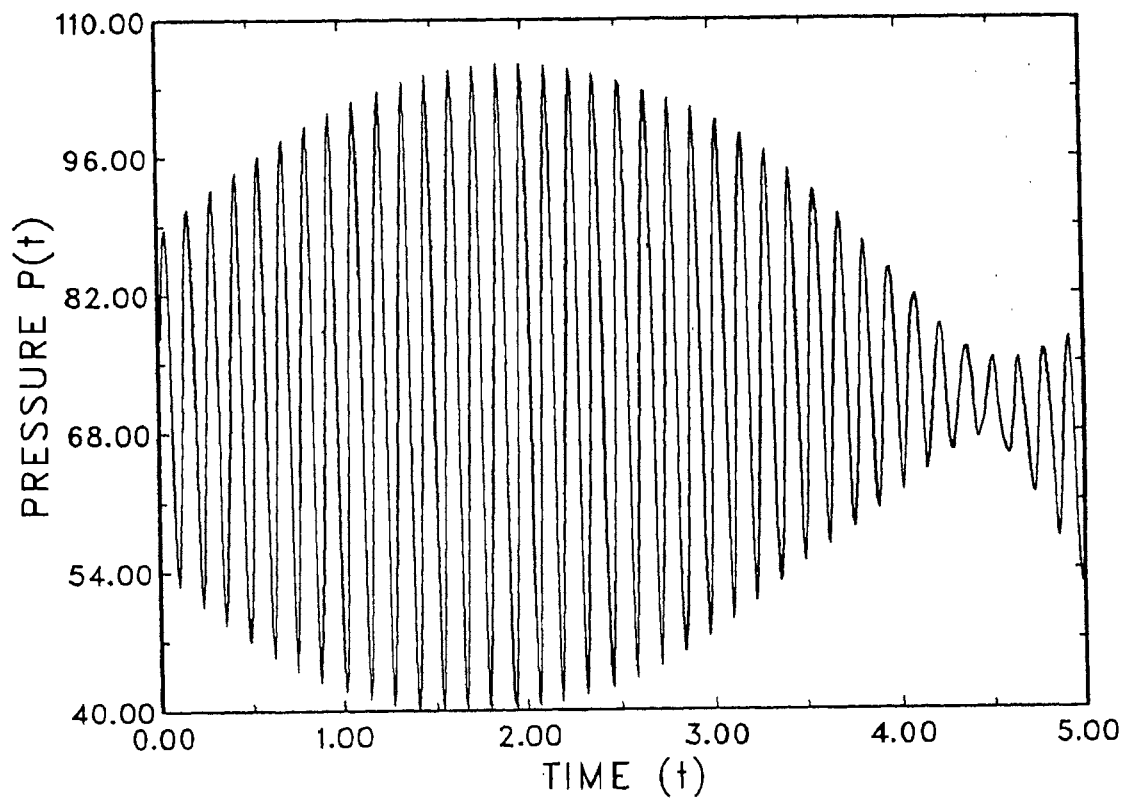
123

Fig.5.1. Temporal evolution of pressure P(t) at an
axial point of the coronal loop when the initial
values of the velocity and magnetic field coeffi-
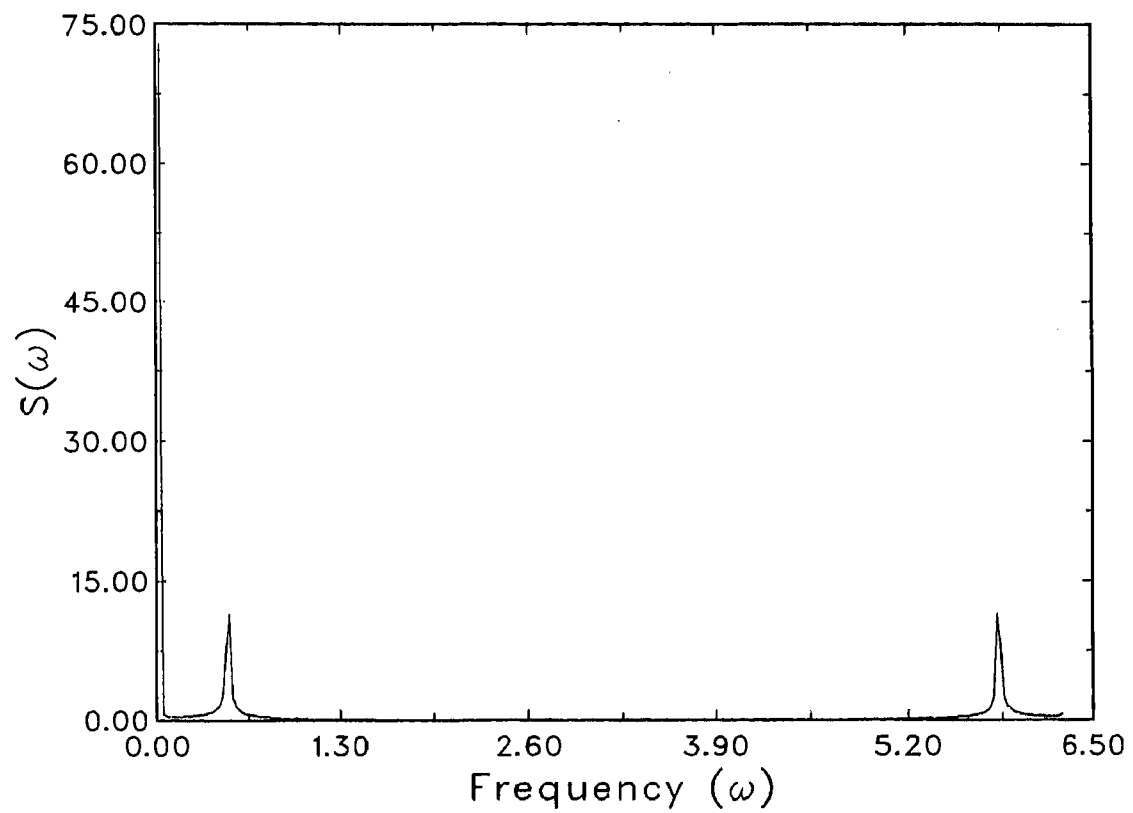cinets are very nearly equal.

124

Fig.5.2. The power spectrum $S(w)-(\text{constant})$ $\lim_{T\to\infty}$ $T^{-1}\left|\int_0^T e^{-i\omega t}P(t)dt\right|^2$ corresponding to the time variation of pressure shown in Fig.5.1.

125

produce any significant change in the pump (stronger) mode and hence, we can neglect all time variations in (η_a, ξ_a) and they remain constant. The system of six equations (5.22) to (5.27) therefore reduces to four(Equations (5.22) and (5.25) are automatically satisfied under the pump approximation since both sides of the equations are vanishingly small). With the additional assumption $\eta_a = \xi_a$ and takes the following simplified form which can be solved analytically.

$$\frac{d\eta_b}{dt} = \frac{\lambda_c \lambda_a}{\lambda_b} (\lambda_a - \lambda_c) \, I^* \, [\eta_c^* - \xi_c^*] \eta_a \qquad (5.30)$$

$$\frac{d\eta_c}{dt} = \frac{\lambda_a \lambda_b}{\lambda_c} (\lambda_b - \lambda_a) \, I^* \, [\eta_b^* - \xi_b^*] \eta_a \qquad (5.31)$$

$$\frac{d\xi_b}{dt} = \lambda_a \lambda_c \, I^* [\eta_c^* - \xi_c^*] \eta_a \qquad (5.32)$$

$$\frac{d\xi_c}{dt} = \lambda_a \lambda_b \, I^* [\xi_b^* - \eta_b^*] \eta_a \qquad (5.33)$$

Derivative of (5.30) w.r.t t keeping η_a as constant, we get

$$\frac{d\eta_b^2}{dt^2} = \frac{\lambda_c \lambda_a}{\lambda_b} (\lambda_a - \lambda_c) \, I^* \, \eta_a \left[\frac{d\eta_c^*}{dt} - \frac{d\xi_c^*}{dt} \right]$$

126

Complex conjugate of equations (5.31) and (5.33) gives

$$\frac{d\eta_c^*}{dt} = \frac{\lambda_a \lambda_b}{\lambda_c} (\lambda_b - \lambda_a) \, I \quad [\eta_b - \xi_b] \eta_a^* \qquad (5.34)$$

$$\frac{d\xi_c^*}{dt} = \lambda_a \lambda_b \, I \, [\xi_b - \eta_b] \eta_a^* \qquad (5.35)$$

The difference between equation (5.34) and (5.35), gives

$$\frac{d\eta_c^*}{dt} - \frac{d\xi_c^*}{dt} = \frac{\lambda_a \lambda_b}{\lambda_c} (\lambda_b - \lambda_a + \lambda_c) \, I \, \eta_a^* \, [\eta_b - \xi_b] \qquad (5.36)$$

Time derivative of equation 5.30 along with equation (5.36) can be written as

$$\frac{d^2 \eta_b}{dt^2} = \lambda_a^2 \, |I|^2 |\eta_a|^2 (\lambda_a - \lambda_c)(\lambda_b - \lambda_a + \lambda_c) \, (\eta_b - \xi_b) \qquad (5.37)$$

where, $II^* = |I|^2$ and $\eta_a x \eta_a^* = |\eta_a|^2$

$$\frac{d^2 \eta_c}{dt^2} = \lambda_a^2 |I|^2 |\eta_a|^2 (\lambda_b - \lambda_a)(\lambda_a - \lambda_b - \lambda_c)(\eta_c - \xi_c) \qquad (5.38)$$

127

Equations (5.37) and (5.38) can be written as

$$\frac{d^2\eta_b}{dt^2} = P_1\eta_b + P_2 \qquad\qquad\qquad (5.39)$$

$$\frac{d^2\eta_c}{dt^2} = P'_1\eta_c + P'_2 \qquad\qquad\qquad (5.40)$$

where,

$$P_1 = \lambda_a^2 (\lambda_a - \lambda_b - \lambda_c)^2 |I|^2 |\eta_a|^2$$

$$P_2 = \lambda_a^2\lambda_b (\lambda_a - \lambda_b - \lambda_c) |I|^2 |\eta_a|^2 I_b$$

$$P'_1 = P_1$$

$$P'_2 = \lambda_a^2 \lambda_c (\lambda_a - \lambda_b - \lambda_c) |I|^2 |\eta_a|^2 I_c$$

$$\xi_b = \frac{\lambda_b}{(\lambda_a - \lambda_c)} (\eta_b - I_b)$$

$$I_b = \eta_{b0} - \frac{(\lambda_a - \lambda_c)}{\lambda_b} \xi_{b0}$$

$$\xi_c = \frac{\lambda_c}{(\lambda_a - \lambda_b)} (\eta_c - I_c)$$

$$I_c = \eta_{c0} + \frac{(\lambda_b - \lambda_a)}{\lambda_c} \xi_{c0}$$

Integrating equations (5.39) and (5.40), we get

$$\eta_b = A\, e^{\sqrt{P_1}\, t} + B\, e^{-\sqrt{P_1}\, t} - \frac{P_2}{P_1} \tag{5.41}$$

$$\eta_c = Q\, e^{\sqrt{P_1}\, t} + R\, e^{-\sqrt{P_1}\, t} - \frac{P'_2}{P_1} \tag{5.42}$$

where A, B, Q and R are to be determined by the initial conditions. Equations (5.41) and (5.42) show that all the four field coefficients η_b, η_c, ξ_b and ξ_c exhibit growing and decaying modes. This is to be expected since there is an infinite capacity pump mode η_a, ξ_a in the system at the expense of which η_b, ξ_b, η_c and ξ_c are growing. Thus, in the case of pump approximation analytical solutions to the system can be found.

5.6. THE NONLINEAR CASE:

Equations (5.22) to (5.27) are a set of six ordinary first

129

order differential equations which are highly nonlinear. Also the velocity field coefficient (η_i) and magnetic field coefficient (ξ_i) components are both coupled which adds to the inherent nonlinearity of the equations of motion, characteristic of MHD equations. These equations in principle can be considered as equivalent to one ordinary sixth order differential equation which will manifest all the nonlinearities and therefore may lead to chaotic dynamics. To investigate this aspect we first determine the power spectrum of the system. A broad band power spectrum **(Fig 5.4)** is a sure indication of the existence of chaos in the dynamics. The irregular and unpredictable time evolution of many non linear systems has been referred to as 'Chaos'. It occurs in mechanical oscilltors such as a pendulum or vibrating objects in rotating or hot fluids, in Laser cavities and in some chemical reactions. Its central characteristic is that the system does not repeat its past behavior (even approximately). Inspite of the lack of regularity chaotic dynamical systems follow deterministic equations such as those determined from Newton's second law.

The unique character of chaotic dynamics can be understood by imagining a system to be started twice, but from slightly different initial condition. This small initial difference can be thought of as resulting from measurement error. For non chaotic system this uncertainty leads only to an error in prediction that

grows linearly with time. For chaotic systems, the error grows exponentially in time, so that the state of the system is essentially unknown after a very short time. This phenomenon, which occurs only when the governing equations are nonlinear, is known as sensitivity to initial conditions. According to Henri Poincare, "it may happen that small differences in the initial conditions produce very great ones in the final phenomena. A small error in the former will produce an enormous error in the latter; prediction becomes impossible. If prediction becomes impossible, it is evident that a chaotic system can resemble a stochastic system (a system subject to random external forces). However, the source of irregularity is quite different. For chaos, the irregularity is part of the intrinsic dynamics of the system, not unpredictable outside influences.

Chaotic motion is not a rare phenomena. Consider a dynamical system described by a set of first order differential equations. The conditions necessary for chaotic motion are that (1) the system has at least three independent dynamical variables; and (2) the equations of motion contain a nonlinear term, that couples several of the variables. The phase space is sufficient to allow for (a) divergence of the trajectories (b) confinement of the motion to a finite region of the phase space of the dynamical variables, and (c) uniqueness of the trajectory. The nonlinearity

131

condition is valid because solutions to linear differential equations can always be expressed as a linear superposition of periodic functions, once initial transients have decayed. The effect of a nonlinear term is often to render a periodic solution unstable for certain parameter choices. These conditions though do not guarantee chaos, they make its existence possible.

The addition of a damping term to the equation for an undamped pendulum results in an attractor at the origin where $\sin\theta \approx \theta$. Further attractors are added at $\theta = \pm n\pi$, $\omega = 0$. This is evident by setting the phase velocity equal to zero and solving for the stationary values of θ and ω. These attractors are points where phase velocity goes to zero. The critical point will reveal whether these trajectories tend to go back to these critical points if slightly perturbed, and will their stability depend upon the direction of the perturbation?

An insight into chaotic system can be obtained by determining the invariant parameters such as correlation dimensions D_i, Kolmogorov entropies K_i, Lyapunov exponents etc which are all infinite in number. However it has been shown that of the infinite number of the correlation dimensions and Kolmogorov information entropies, the second order quantities are the most significant ones and hence the need to determine D_2 in the present analysis. The

algorithm followed in this chapter is that proposed by Grassberger and Proccacia (1983) and later developed by Atmanspacher and Schinegraber (1986) and Abraham et al(1986).

Let $\{X_0(t)\}$ be the original time series with the data being taken at constant interval. These data set can be rearranged so as to get (d-1) additional data sets as

$$X_0(t_1)\ldots\ldots\ldots\ldots\ldots\ldots X_0(t_N)$$
$$X_0(t_1+\Delta t)\ldots\ldots\ldots\ldots\ldots X_0(t_N+\Delta t)$$
.   .

.   .

.   .

.   .

.   .
$$X_0(t_1+d\Delta t)\ldots\ldots\ldots\ldots\ldots X_0(t_N+d\Delta t)$$

The transpose of the above matrix can be considered as consisting of N vectors having d components in a d dimensional space. The general vector can be written as

$$\bar{X}_i=(X_0(t_1)\ldots\ldots\ldots X_0(t_1+d\Delta t))$$

where, $i = 1\ldots N$ and $\bar{X}_i$ is a point in the constructed d dimensional space. With this the correlation function can be evaluated.

133

$$C_d(r) = \underset{N \to \infty}{Lt} \frac{1}{N^2} \sum_{i,j=1,N} \theta(r - |X_i - X_j|)$$

where θ is the Heaviside function defined as $\theta(x) = 0$ for $x < 0$ and unity for $x > 0$. This implies that if the absolute value of the vector difference $|X_i - X_j|$ is less than r, it is counted as unity and is zero if it is greater than r. Small boxes of side r are constructed in the phase space and the vector tips that lie in this box are counted. This is referred to as box counting. It is seen that as r becomes smaller $C_d(r) \sim r^\nu$, so that

$$\log C_d(r) \sim \nu \log r$$

As $r \longrightarrow 0$ and $d \longrightarrow \infty$, ν takes a definite value which is called the second order correlation dimension. i.e.

$$D_2 = \underset{\substack{r \to 0 \\ d \to \infty}}{\lim} \frac{\log C_d(r)}{\log (r)}$$

The correlation integral $C(r)$ is calculated for several values of r with respect to each particular dimension d of the constructed phase space. For each dimension d a curve of $\log C_\partial(r)$ Vs. $\log (r)$ is drawn. The slope ν of the linear part of the curve

134

is obtained using least square fit. The finite value to which ν converges for higher values of d is denoted by D_2 An integer value for D_2 indicates that the system is regular and a fractal value that the system is chaotic.

The equations (5.22) to (5.27) have been numerically solved for arbitrary initial values of the field coefficients. The time evolution of pressure at an axial point of the loop for initial values

$$|\eta_a| = 4.0, \quad |\eta_b| = 7.0, \quad |\eta_c| = 10.0,$$
and,
$$|\xi_a| = 8.0, \quad |\xi_b| = 11.0, \quad |\xi_c| = 14.0$$

is shown in Figure 5.3. The time variation is found to be highly complex. The corresponding power spectrum is shown in Figure 5.4. The power spectrum is found to be fluctuating and has a broad band indicating the presence of chaos. A set of 500 data points corresponding to this chaotic evolution of pressure was used to evaluate the information dimension D_2 by the box counting method described above.

Figure 5.5 illustrates the converging and from which the value of D_2 is found to be 1.732. For the same initial conditions
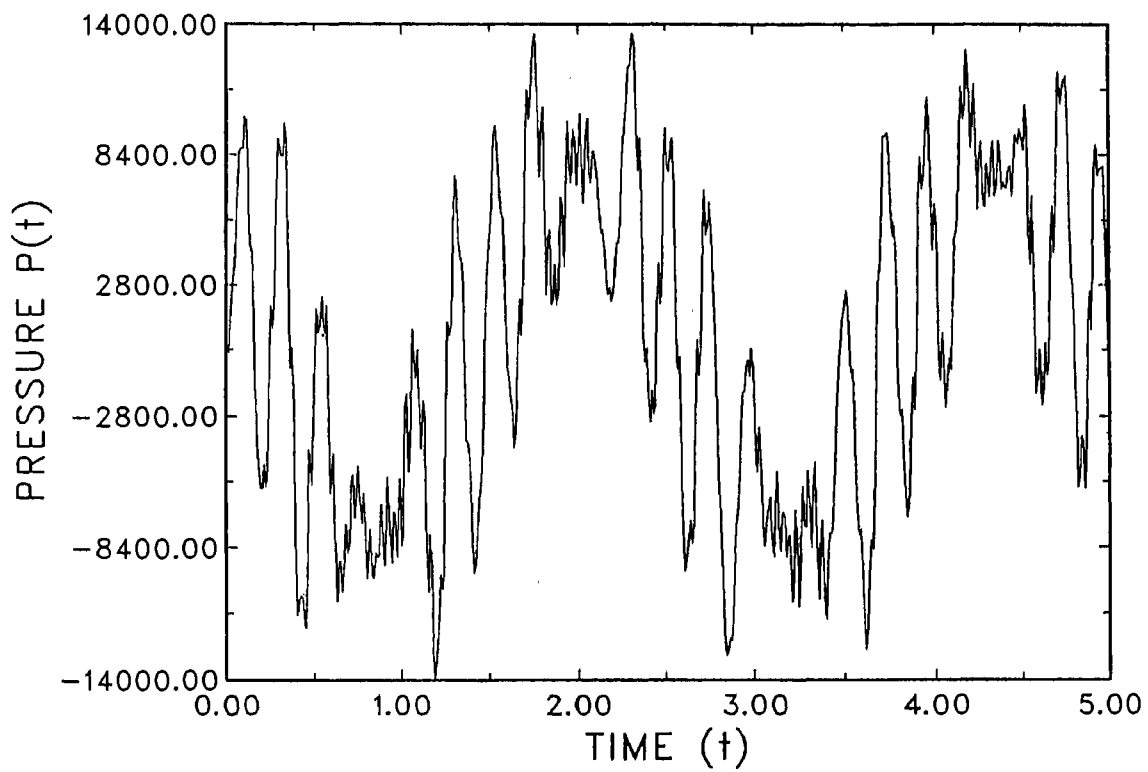
Fig.5.3.. The variation of pressure at an axial point of the loop when the initial values of the fieldcoefficients η_a, η_b, η_c are much different from those of ξ_a, ξ_b and ξ_c respectively.
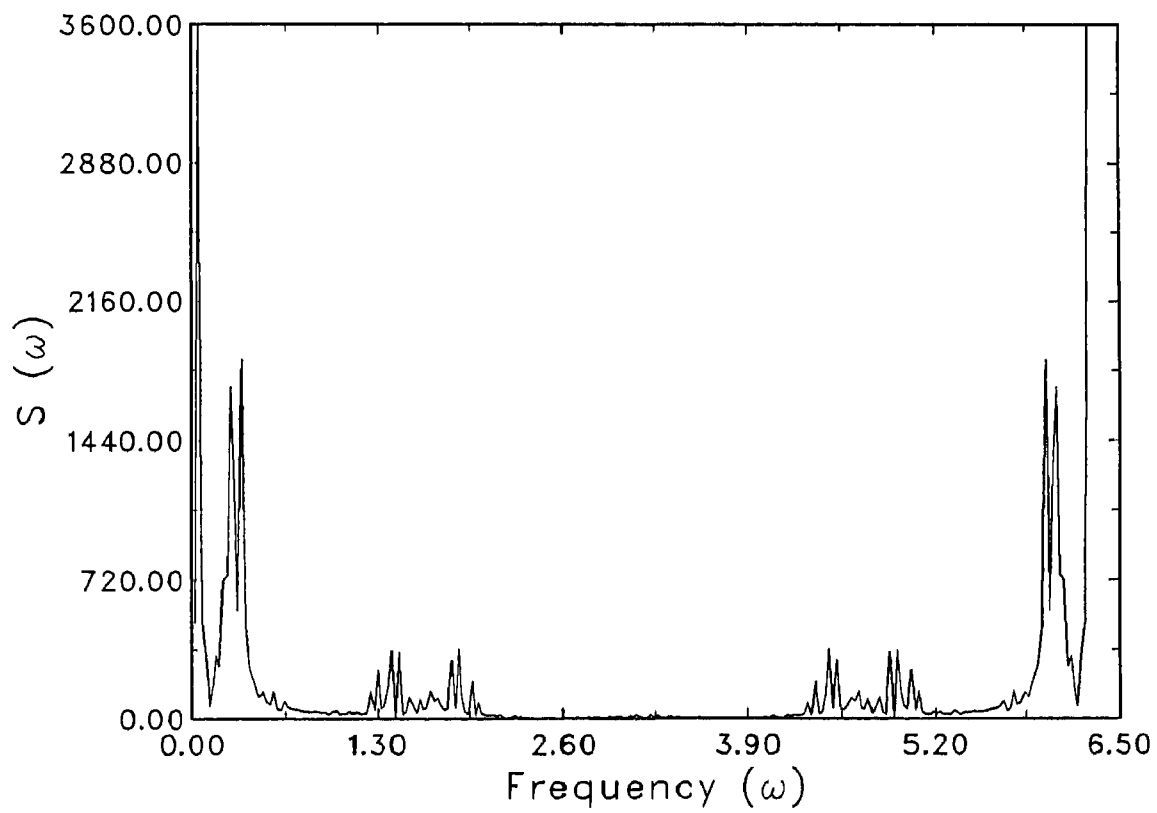
Fig.5.4. Power spectrum S(w) corresponding to the
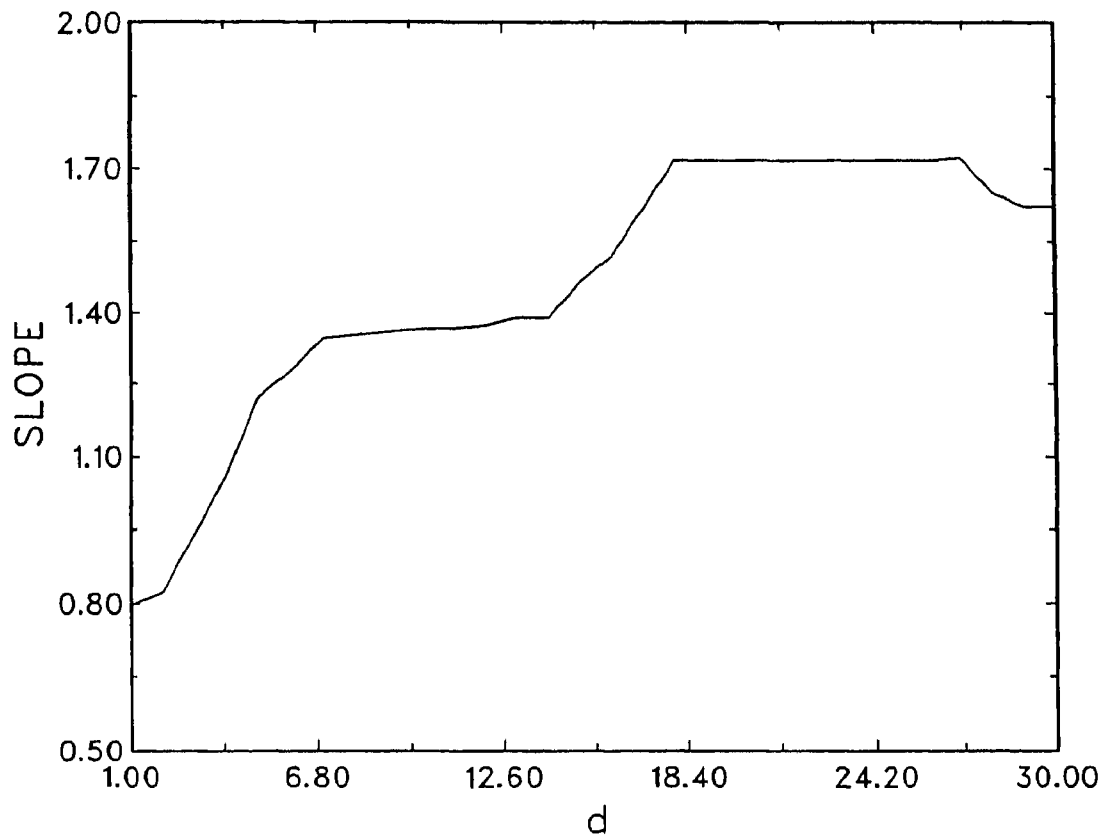time variation of pressure shown in Fig.5.3.

137

Fig.5.5. The slope (ν) of the linear part of the $\log C_d(r)$ vs $\log(r)$ curves, obtained using least-squares fits are plotted against the dimension d of the constructed phase space. The two asymptotic values of the slopes are 1.39 and 1.73. This is corresponding to the chaotic evolution of pressure at an axial point of the loop.

when D_2 is evaluated at a surface point, the slope does not seem to converge to a limiting value (Figure5.6). The fractal value of D_2 is clear evidence for the existence of deterministic chaos.

In a chaotic regime the system can either dissipate to an attractor stage or can follow a stochastic(random) flow. As the dimension d of the constructed phase space increases the slope v may converge to a limiting value. In this case the flow will be confined to a geometrical object called attractor. The converging value of the slope is the dimension D_2 of the attractor. The dimension of the attractor measures the minimum number of independent parameters needed to describe the system dynamics. In other words if D_2 exists, there is a properly defined dynamical system. The steady increase of slope v with d (Figure 5.6)evidently shows that it cannot converge and consequently the number of degrees of freedom of the system is increasing. Then the complexity of the system increases and it tends to a more disordered state indicating that system behavior is stochastic.

5.7 SUMMARY:

In the equilibrium state $\eta_a = \xi_a$, $\eta_b = \xi_b$, $\eta_c = \xi_c$. When the
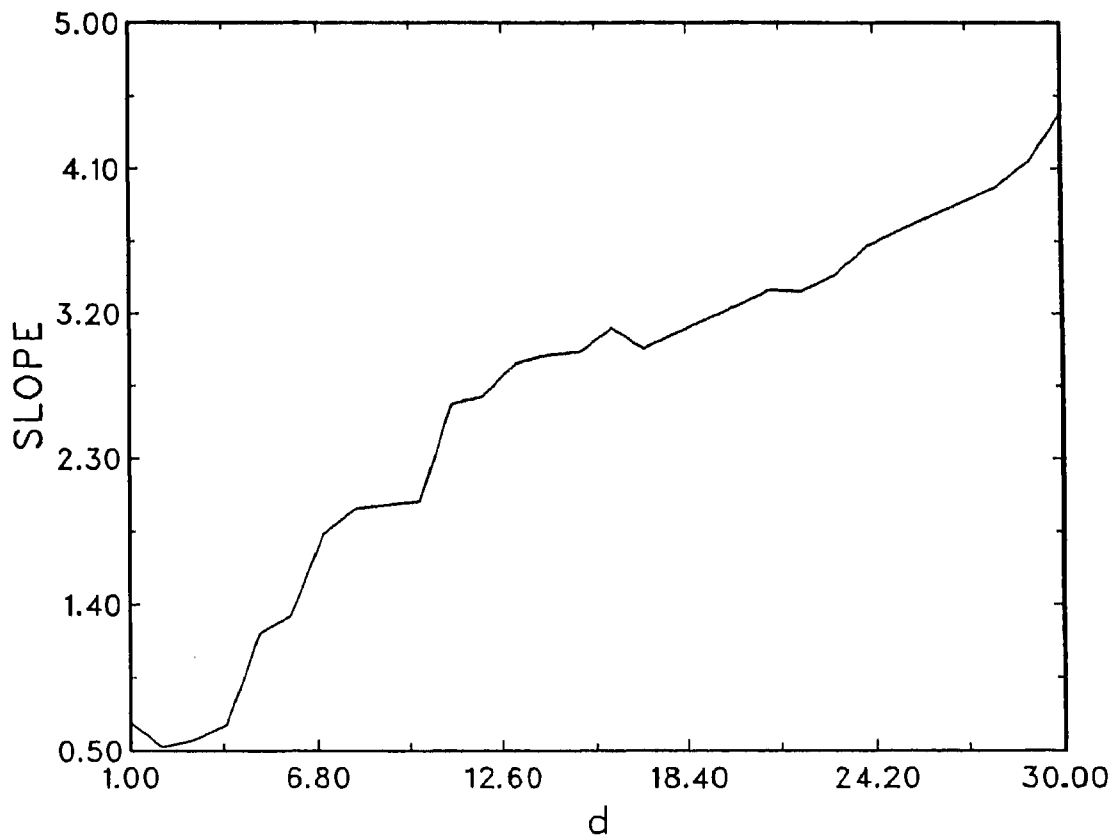
Fig. 5.6. Corresponding to the chaotic time evolution of pressure at a surface point of the loop, the slopes(v)of the linear part of the $logC_d$ vs $log(r)$ curves are plotted against the dimension d. The slopes do not converge to any limiting value.

system is slightly disturbed from the equilibrium state, the time evolution for small departure from equilibrium condition reveals that the system exhibits sinusoidal oscillation with a period which depends upon the initial values of the field coefficients. In other words, when the system is perturbed from a state where the magnetic energy $B^2/4\pi$ and the kinetic energy $(1/2)mv^2$ are nearly equal, it exhibits marginal stability. The microwave and X-ray observations of coronal loops show quasi periodic oscillations with time scales ranging from a fraction of a second to tens of minutes. (Aschwanden 1987, Svestka 1994 and references therein). These oscillations are usually interpreted in terms of magnetohydrodynamic waves in loop plasma. (Roberts, Edwin and Benz 1984). The observed power spectrum of pulsations actually exhibits a more complex behavior (e.g. fig. 1d of Svestka 1994) which appears quasi periodic only if we ignore finer variations. Thus, quasi periodic behavior is expected only near equilibrium as is shown in the above study and the linear wave analysis studies. Under large departures from the equilibrium, a loop shows a complex temporal structure which can only be described in terms of objects with fractal dimensions in the phase space of the velocity and magnetic field. Coronal loops being continuously subjected to external forcing through their foot points and through their interaction with neighboring regions are most likely to be in a chaotic state of pressure fluctuations. Therefore , when there are large deviations from equilibrium i.e., for initial values of

141

η_a, η_b, η_c much different from those of ξ_a, ξ_b, ξ_c respectively, the system is nonlinear and so is the corresponding time evolution of the pressure. In this case each individual mode becomes distinct, stronger and mode-mode interaction can take place. In the pump approximation case since the variation of the strongest mode is negligible when compared with other modes, the interaction is between less number of modes of oscillations and the system showed oscillatory behavior, whereas the chaotic behavior is caused by the superposition of more than two modes of oscillation and due to strong nonlinear coupling between them as is indicated in the nonlinear case above. This fact is evident in the evaluation of D_2. Figure 5.5 shows the determination of D_2 at an axial point. It is interesting to note that there are two asymptotic values, one at 1.39 and the other at 1.73. This could be interpreted as the existence of two strange attractors with embedding space of dimension 7 and 18 and the trajectory can land up on either of these attractors. The fact that these are strange attractors (because of fractal dimension) the trajectories could jump from one to the other. This clearly shows the complexity of the situation. The curve of slope ν vs dimension d at r=R does not show any saturation and that the curve is more or less centered on the 45° line showing the presence of randomness or white noise as shown in Figure 5.6. Thus, as we proceed from the axis towards the surface the dynamics show the development of strange attractors ending up

142

in complete randomness.

In figure 5.5 and 5.6 even though the initial values of ξ's and η's are the same, those of pressure P at (r=0, t=0) and at (r=R, t=0) are not same. This difference in Figure 5.5 and 5.6 is due to the different initial values of pressure at axial and surface points. The transition from a strange attractor state to randomness requires a much finer analysis. In conclusion the time scale over which the system is stable or otherwise can be inferred only by evaluating the Lyapunov constants which are sensitive to the initial conditions. Inverting the problem by specifying the lyapunov constants, one can possibly evaluate the class of initial states which can give the observed life time of the loops.

6 VLASOV MAXWELL-EQUILIBRIA OF SOLAR CORONAL LOOPS

6.1 INTRODUCTION:

The fluid theory that has been used so far in the previous chapters is the simplest description of a plasma. This approximation is sufficiently accurate to describe the majority of observed phenomena. However, there are some phenomena for which a fluid treatment is inadequate. For such cases we need to consider the velocity distribution function $f(v)$ for each species. This treatment is called Kinetic theory. In fluid theory, the dependent variables are functions of only four independent variables: x, y, z and t. This is possible because velocity distribution of species is assumed to be Maxwellian everywhere and can therefore be uniquely specified by only one number, the temperature T. Since collisions can be rare in high temperature plasmas, deviations from thermal equilibrium can be maintained for relatively long times.

Exact nonlinear solutions to coupled field theories are generally rare. For the Vlasov-Maxwell system describing a

144

collision less plasma the list of reported exact solutions are: (1) the electrostatic solutions of the Bernstein-Green-Kruskal(BGK) type (2)the magnetic solutions of the type obtained by Pfirsch,Laval,Pellat and Vuillemin, Marx and Harris. The magnetic solutions were constructed to model the behavior of laboratory plasma containment devices. It was assumed that only the plasma density was a function of space while plasma temperature and current are taken to be spatially uniform. The process leads to the well known Bennet pinch density profiles in the cylindrical geometry, and to the strongly localised $sech^2x/\delta$ (where δ is some appropriate length) profiles in the slab model. A more realistic description of the current laboratory plasmas, however, would require the inclusion of the temperature as well as the current gradients (i.e., gradients in current which are in addition to the automatic gradients resulting from the density dependence of current). It is with this idea that in this chapter a vlasov-Maxwell description of the ubiquitous solar coronal structures is discussed. It is found that an equilibrium plasma configuration can live with spatial gradients in density, temperature, current and drift speeds of the charged particles. The stability study is carried over this inhomogeneous equilibrium state. The Vlasov description admits the investigation of kinetic processes like heating and radiation and unlike a fluid description, it does not require an equation of state to determine

145

the individual variations of temperature and density.

6.2 DERIVATION OF THE VLASOV EQUATION:

A kinetic equation is any equation of the form

$$\frac{\partial F_1}{\partial t} = M \ [F_1] \tag{6.1}$$

where M is a known functional that maps F_1 onto functions of $(p, x, t; F_1)$. The generic form for all kinetic equations is,

$$\frac{\partial F_1}{\partial t} + \frac{p_1}{m} \frac{\partial F_1}{\partial x_1} = -\frac{1}{v} \frac{\partial}{\partial p_1} \int d2G_{12} \ F_2(1,2) \tag{6.2}$$

in dimensional form. To obtain a kinetic equation from this equation some approximate form must be inserted for F_2, or equivalently, F_2 must be expressed as some known functional of F_1.

$$F_2 = F_2(1,2;F_1) \tag{6.3}$$

Inserting equation (6.3) into (6.2) gives the kinetic equation

$$\frac{\partial F_1}{\partial t} + \frac{p_1}{m} \frac{\partial F_1}{\partial x_1} = -\frac{1}{v} \frac{\partial}{\partial p_1} \int d2 G_{12} F_2(1,2; F_1) \qquad (6.4)$$

The equation that emerges for F_1 in an expansion about vanishing correlation is (dimensional notation).

$$\frac{\partial F_1}{\partial t} + \frac{p_1}{m} \frac{\partial F_1}{\partial x_1} + \frac{1}{v} \frac{\partial}{\partial p_1} \int d2 G_{12} F_1(1) F_1(2) = 0 \qquad (6.5)$$

This equation is known as Vlasov equation. The vlasov equation may be put in a more conventional form using the fact that the number density $n(x, t)$ can be expressed in terms of F_1 as

$$n(x, t) = \frac{1}{v} \int F_1 \, dp \qquad (6.6)$$

If the mean force $G(x)$ at the point x is defined as

$$G(x_1) \equiv \int n(x_2) \, G_{12}(x_1, x_2) dx_2 \qquad (6.7)$$

then, the integral in equation (6.5) may be written in terms of G and F_1 :

147

$$\frac{\partial}{\partial p_1} \int d^3x_2 \, d^3p_2 G_{12}(x_1, x_2) \, F_1(1) \, \frac{F_1(2)}{v} = \frac{\partial}{\partial p_1} F_1(1) \int d^3x_2 G_{12} n(x_2)$$

$$= \frac{\partial}{\partial p_1} F_1(1).G(x_1) \qquad (6.8)$$

Equation (6.5) is equivalent to

$$\frac{\partial F}{\partial t} + \frac{p}{m} \cdot \frac{\partial F}{\partial x} + \frac{\partial F}{\partial p} \cdot G = 0 \qquad (6.9)$$

$$G(x_1) \equiv \int G_{12}(x_1, x_2) \, n(x_2) \, d^3x_2 \qquad (6.10)$$

$$vn(x_2) = \int F_1(2) \, d^3p_2 \qquad (6.11)$$

Vlasov equation represents the dynamics of a single particle influenced by a smeared out or average force field. This average force field is the average of the two particle interaction over the density of remaining particles. The G in the vlasov equation is a functional of F through the equations (6.10) and (6.11).

148

6.3 THE MEANING OF f(v):

In kinetic description the density is a function of four scalar variables $n = n(r,t)$. When velocity distribution is considered there are seven independent variables: $f = f(r,v,t)$. This implies the number of particles per m^3 at the position r and at time t with velocity components between v_x and $v_x + dv_x$, v_y and v_y + dv_y, and v_z and $v_z + dv_z$. is

$$f(x,y,z,v_x,v_y,v_z,t)dv_x \; dv_y \; dv_z.$$

Theintegral of this can be written in any one of the ways as shown below.

$$n(r,t) = \int_{-\infty}^{\infty} dv_x \int_{-\infty}^{\infty} dv_y \int_{-\infty}^{\infty} dv_z \; f(r,v,t) = \int_{-\infty}^{\infty} f(r,v,t)d^3v$$

$$= \int_{-\infty}^{\infty} f(r,v,t)dv \qquad (6.12)$$

dv is not a vector; but it represents a three dimensional volume element in velocity space. If f is normalized so that

$$\int_{-\infty}^{\infty} \hat{f}(r, v, t)dv = 1 \qquad\qquad (6.13)$$

$\hat{f}$ is called the probability distribution function.

So that $f(r, v, t) = n(r, t)\hat{f}(r, v, t)$ $\qquad\qquad (6.14)$

$\hat{f}$ is still a function of seven variables, since the shape of the distribution, as well as the density, can change with space and time.

A particularly important distribution function is the maxwellian:

$$\hat{f}_m = (m/2\pi \, KT)^{3/2} \exp(-v^2/v_{th}^2) \qquad\qquad (6.15)$$

where $v \equiv (v_x^2 + v_y^2 + v_z^2)^{1/2}$ and $v_{th} \equiv (2KT/m)^{1/2}$ $\qquad (6.16)$

For an isotropic distribution like a maxwellian, another function $g(v)$ which is a function of the scalar magnitude of v such that

$$\int_0^{\infty} g(v) \, dv = \int_{-\infty}^{\infty} f(v)d^3v \qquad\qquad (6.17)$$

can be defined.

150

For a maxwellian the function $g(v)$ will be of the form.

$$g(v) = 4\pi n (m/2\pi KT)^{3/2} v^2 \exp(-v^2/v_{th}^2)$$
(6.18)

6.4 EQUATIONS OF KINETIC THEORY:

The fundamental equation which $f(\mathbf{r}, \mathbf{v}, t)$ has to satisfy is the Boltzmann equation:

$$\frac{\partial f}{\partial t} + \mathbf{v} \cdot \bar{\nabla} f + \frac{\mathbf{F}}{m} \cdot \frac{\partial f}{\partial \mathbf{v}} = \left(\frac{\partial f}{\partial t}\right)_c$$
(6.19)

F is the force acting on the particles, and $(\partial f/\partial t)_c$ is the time rate of change of f due to collisions. ∇ represents the gradient in (x, y, z) space. The symbol $\partial/\partial v$ or ∇_v stands for the gradient in velocity space:

$$\frac{\partial}{\partial \mathbf{v}} = \hat{\mathbf{x}} \frac{\partial}{\partial v_x} + \hat{\mathbf{y}} \frac{\partial}{\partial v_y} + \hat{\mathbf{z}} \frac{\partial}{\partial v_z}$$
(6.20)

In a sufficiently hot plasma, collisions can be neglected. Further the force **F** is entirely electromagnetic and hence, the equation

151

(6.19) takes the form and if E and B are self consistent fields,

$$\frac{\partial f}{\partial t} + \mathbf{v} \cdot \nabla f + \frac{q}{m} (E + \mathbf{v} \times B) \cdot \frac{\partial f}{\partial \mathbf{v}} = 0 \qquad (6.21)$$

This is Vlasov equation.

6.5 VLASOV-MAXWELL EQUILIBRIA:

The coronal loop plasma will be represented by a cylindrical column with current density J_z along the axis of the cylinder and with no gravity. The actual geometry of a coronal loop consists of the two ends (the foot points) of a cylindrical plasma embedded in a sub photospheric region. A small twisting motion of the foot points may introduce a small amount of azimuthal current J_θ which is neglected for the present. The subphotospheric region contains a high-β plasma, where β is the ratio of gas kinetic pressure to magnetic pressure. As a result the magnetic field lines move on a time scale much longer than the coronal time-scales. This line tying reduces the region of unstable excitations, especially those of long wavelength. The neglect of gravity reduces the coronal loop to an essentially horizontal

152

cylinder. While studying the stability of an equilibrium, the end effects, gravity and curvature are to be properly taken into account.

The particle density n, the temperature T and the particle drift speeds u are in general, spatially varying quantities. All spatial variations are allowed only in the radial direction as there is observational evidence in support of it. The plasma is assumed to be embedded in a uniform magnetic field B_0. The relevant equation for an equilibrium system (with $\partial/\partial t = 0$), i.e., Boltzman equation for electron and ions describing the conservation of particles in phase space of position and momenta are:

$$V_r \frac{\partial f_e}{\partial r} - \frac{e}{m_e} [E + \frac{V}{c} \times (B + \hat{e}_z B_0). \frac{\partial f_e}{\partial V} = 0 \qquad (6.22)$$

$$V_r \frac{\partial f_i}{\partial r} + \frac{e}{m_i} [E + \frac{V}{c} \times (B + \hat{e}_z B_0). \frac{\partial f_i}{\partial V} = 0 \qquad (6.23)$$

Equations (6.22) and (6.23) are Vlasov equations which are valid at high temperatures when Coulomb collisions are neglected.

In addition, the fully ionized plasma is assumed to experience only electromagnetic forces. All non electromagnetic

forces such as gravity are neglected. For loops of smaller length than the density scale height, axial dependence of particle density is also neglected.

Ampere's law is:

$$\nabla \times B = \frac{1}{c} \frac{\partial E}{\partial t} + \frac{4\pi}{c} J \qquad (6.24)$$

and for the case $(\partial/\partial t = 0)$

$$\nabla \times B = \frac{4\pi}{c} J \qquad (6.25)$$

Writing in cylindrical co-ordinates:

$$(\nabla \times B)_r = \frac{1}{r} \frac{\partial B_z}{\partial \theta} - \frac{\partial B_\theta}{\partial z} = \frac{4\pi}{c} J_r \qquad (6.26)$$

$$(\nabla \times B)_\theta = \frac{\partial B_r}{\partial z} - \frac{\partial B_z}{\partial r} = \frac{4\pi}{c} J_\theta \qquad (6.27)$$

$$(\nabla \times B)_z = \frac{1}{r} \frac{\partial}{\partial r}(rB_\theta) - \frac{1}{r} \frac{\partial B_r}{\partial \theta} = \frac{4\pi}{c} J_z \qquad (6.28)$$

154

$(\nabla \times B)_r = 0$ and $(\nabla \times B)_\theta = 0$ implies that the self consistent magnetic field has only θ component. For this to be true B_r should be zero, B_z = constant. Hence, the axial component of Ampere's law will be:

$$\frac{1}{r} \frac{\partial}{\partial r} rB_\theta = \frac{4\pi}{c} J_z \qquad (6.29)$$

Poisson's equation is:

$$\nabla \cdot E = 4\pi\rho \qquad (6.30)$$

In equilibrium study the charge separation occurs over extremely short time scales. Hence, it is justifiable to assume zero charge separation. Under such a condition

$$\nabla \cdot E = 0 \qquad (6.31)$$

Faraday's law is:

$$\nabla \times E = -\frac{1}{c} \frac{\partial B}{\partial t} \qquad (6.32)$$

For steady state fields the equation reduces to

155

$$\nabla \times \mathbf{E} = 0 \qquad\qquad (6.33)$$

The plasma current density J_z in terms of the particle distribution function for the electron and ion is

$$J_z = -e \int d^3V \, v_z \, (f_e - f_i) \qquad\qquad (6.34)$$

Let a displaced Maxwellian of the form

$$f_{e,i} = \frac{n_0}{\pi^{3/2} V_{e,i}^3} \, \text{Exp} \left[-\left(V - u_z^{e,i} \right)^2 / v_{e,i}^2 \right] \, g(r) \qquad\qquad (6.35)$$

be the distribution function for the particles providing a self consistent solutions for the equations (6.22), (6.23), (6.29), (6.31) (6.33) and (6.34). Where,

n_0 is the ambient density,

$V_{e,i} = \left[2T_{e,i} / m_{e,i} \right]^{1/2}$ is the thermal speed,

and $u_z^{e,i}$ is the drift speed,

$T_{e,i}$ is the temperature,

$m_{e,i}$ is the mass and

$g(r)$ is the density profile factor, which is the same for electrons and ions under conditions of no charge separation.

156

6.5.1 DETERMINATION OF DENSITY AND MAGNETIC FIELD PROFILES:

Let $g(r)$ describe the entire spatial variation of density. The density profile can be found assuming f_e to be a function of $g(r)$.

Equation (6.35) can be written as:

$$f_e = k_e g(r) \quad \text{and} \quad f_i = k_i g(r) \tag{6.36}$$

where $k_{e,i} = \dfrac{n_0}{\pi^{3/2} v_{e,i}^3} \exp\left[-(V - u_z^{e,i})^2/v_{e,i}^2\right]$

Hence,

$$\frac{\partial f_e}{\partial V} = - \frac{2k_e g(r)}{v_e^2} [V - u_z^o] \tag{6.37}$$

$$\frac{V}{c} \times (B + \hat{e}_z B_0) \cdot \frac{\partial f_e}{\partial V} = \frac{2k_e g(r)}{v_e^2 c} [\, u_z^e \, v_r \, B_\theta \,] \tag{6.38}$$

$$E \cdot \frac{\partial f_e}{\partial V} = - \frac{2k_e g(r)}{v_e^2} [E_r \, v_r] \tag{6.39}$$

157

$$\frac{\partial f_e}{\partial r} = k_e \frac{\partial g(r)}{\partial r} \qquad\qquad (6.40)$$

Substituting equation (6.38),(6.39) and (6.40) in equation (6.22)

$$\frac{1}{g} \frac{dg}{dr} + \frac{2 e}{m_e v_e^2} \frac{[-u_z^e B_\theta]}{c} = 0 \qquad\qquad (6.41)$$

or $\frac{1}{g} \frac{dg}{dr} = \frac{e}{T_e c} u_z^e B_\theta = b$ $\qquad\qquad (6.42)$

where $b = \frac{e u_z^e B_\theta}{cT_e}$ $\qquad\qquad (6.43)$

where, e is the charge on the electron and c is the speed of light. From equation (6.29)

$$\frac{1}{r} \frac{\partial}{\partial r} rB_\theta = \frac{4\pi}{c} J_z = -\frac{4\pi}{c} en_0 [g_e u_z^e - g_1 u_z^1] \qquad\qquad (6.44)$$

Making use of equation (6.43), this reduces to

$$\frac{1}{r} \frac{\partial}{\partial r} \left[\frac{rbcT_e}{eu_z^e} \right] = -\frac{4\pi e\, n_0}{c} u_z^e \left[g_e - \frac{u_z^1}{u_z^e} g_1 \right] \qquad\qquad (6.45)$$

158

using $g_i = g_e = g$, $\quad \mu = \dfrac{u_z^i}{u_z^e}$ and, $T_e = (1/2)m_e v_e^2$ in equation (6.45)

$$\frac{1}{r} \frac{d}{dr} (rb) = - \frac{2}{\delta^2} g \qquad\qquad (6.46)$$

where δ_e is the characteristic length scale in the solutions of the Vlasov-Maxwell system which will be estimated using the parameters chosen from Hollweg(1981), and

$$\delta_e^2 = \frac{2c^2}{\omega_{pc}^2} \frac{v_e^2(1-\mu)^{-1}}{2(u_z^e)^2} \qquad\qquad (6.47)$$

and ,the electron plasma frequency

$$\omega_{pc} = \left[\frac{4\pi n_e^2}{m_e} \right]^{1/2} \qquad\qquad (6.48)$$

The self consistent solutions for equations (6.22),(6.23), (6.29),(6.31),(6.33) and (6.35) when g(r) describes the entire spatial variation are found to be

$$g(r) = \left[1 + \frac{r^2}{4\delta_e^2} \right]^{-2} \tag{6.49}$$

Figure 6.1 is a plot of density profile function $g(r)$ versus $x = r/\delta_e$ .The graph shows that the density profile is peaked at the axis with a characteristic length scale δ_e and a sharp fall in density away from the axis is obtained. This is reminiscent of the condensations often observed at the axis of the loop.

Using equation (6.49) in (6.42), we obtain

$$b = - \frac{r}{\delta_e^2 \left[1 + \frac{r^2}{4\delta_e^2} \right]} \tag{6.50}$$

$$\text{Or, } b\delta_e = - (r/\delta_e) \left[1 + \frac{r^2}{4\delta_e^2} \right]^{-1} \tag{6.51}$$

Figure 6.2 is a plot of the variation of the magnetic field profile function $(b\delta_e)$ verses $x = r/\delta_e$ corresponding to the above equation. This graph also indicates the magnetic field profile peaking at the axis similar to the density profile case. Thus, from these two graphs it is found that the current density is maximum on the axis.

160
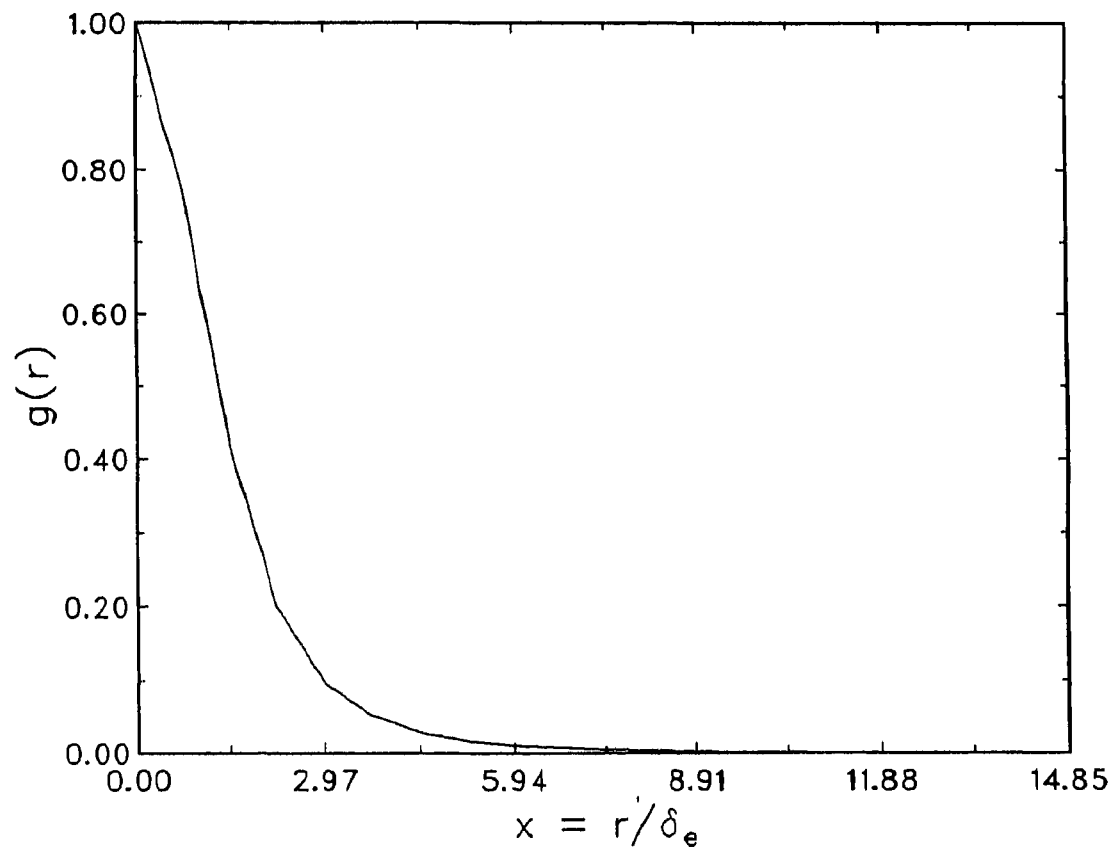
Fig.6.1. Variation of density profile function g(r) vs
x = r/δ$_e$
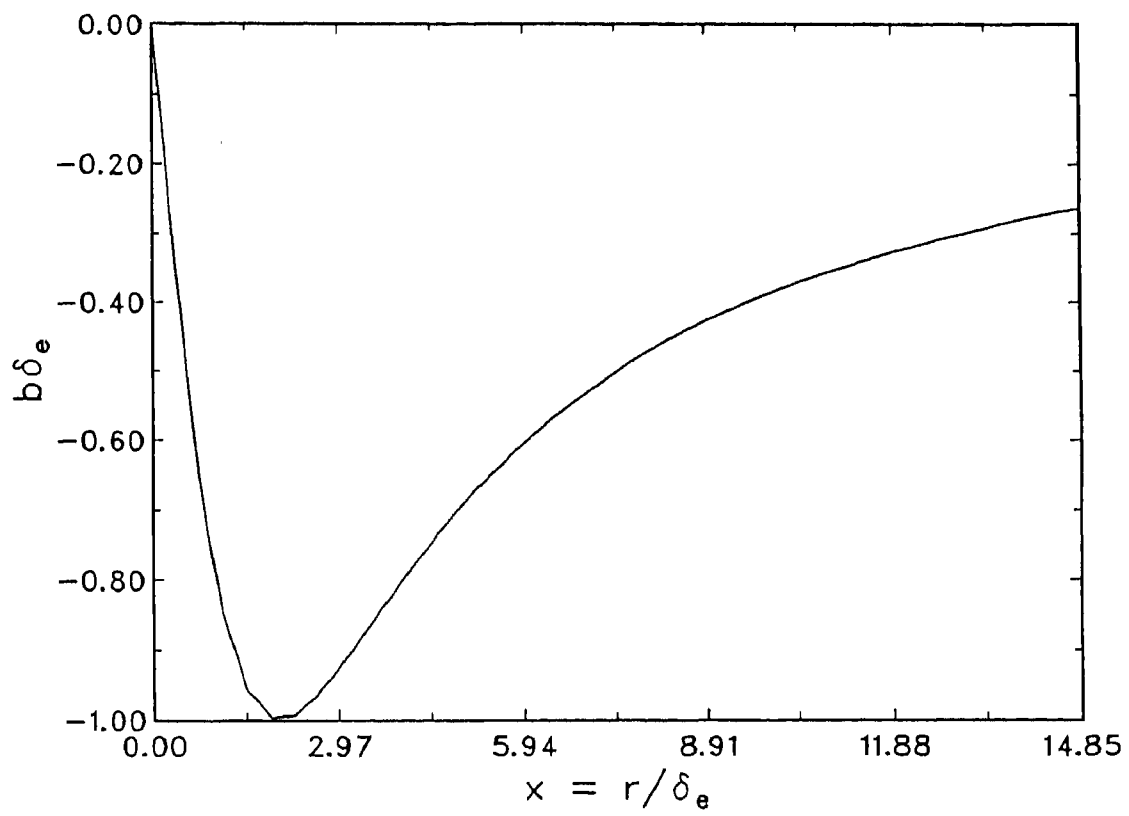
Fig.6.2.Variation of magnetic field profile function
$(b\delta_e)$ vs $x = r/\delta_e$.

6.5.2 ESTIMATION OF CHARACTERISTIC LENGTH δ_e :

Coronal loops, a bipolar structure is characterized by an electron density $n_0 \sim 10^{10} - 10^{12} cm^{-3}$; a temperature range varying from a few tens of thousands to a couple of million K, a radius of $10^8 - 10^9$, and a length of 10^9 to $10^{10} cm$ with an axial magnetic field of a few gauss. The current flows essentially along the axis of the cylindrical plasma column and produces an azimuthal component B_θ of the magnetic field. Observations in the EUV region shows that the loops of different temperatures are coaxial and this has led to the identification of cool core and hot sheath type loops (Foukal 1978; Krishan 1983, 1985). The X-ray observations has further reinforced the inhomogeneous nature of the underlying heating mechanisms. According to Hollweg (1981), the resonance absorption of surface MHD waves, as well as the Joule dissipation of high density current sheets in addition to the ubiquitous mini magnetic reconnections are some of the factors responsible for the heating of the solar corona in general, and coronal loops in particular. Assuming typical parameters from Hollweg δ_e is estimated as follows:

Electron density in the sheath $n_0 = 10^9 cm^{-1}$;
Electron temperature in the sheath $T_e = 2.5 \times 10^7 K$;

Electron thermal speed $V_e = 2.7 \times 10^9$ cm s^{-1};

Electron drift velocity $u_e >$ sound speed $\approx 4.5 \times 10^7$ cm s^{-1};

The magnetic field B_θ produced by the current density J_z is 10 G,

and the thickness (ΔR) of the current sheet turns out to be $\sim 10^3$

cm.

The characteristic length scale which is

$$\delta_e = \frac{c}{\omega_{pc}} \frac{V_e}{u_e} (1 + \sqrt{T_i/T_e})$$

works out to be $= 1.04 \times 10^3$ cm for $T_e \gg T_i$, and,

$= 0.9 \times 10^3$ cm for $T_e = 9T_i$.

Thus, we find that current profile of small widths are the outcome

of exact solutions of the Vlasov-Maxwell system.

6.5.3 VARIATION OF MAGNETIC FIELD PROFILE WHEN TEMPERATURE

VARIATION IS ALLOWED IN ADDITION TO DENSITY VARIATION:

In this case in addition to the density gradient; spatial

164

variation of temperature is also allowed. The drift speeds $u_z^{e,i}$ are still homogeneous. Mahajan(1989) has shown that a series representation for the distribution function gives a valid solution of the inhomogeneous Vlasov-Maxwell system. The expansion parameter for the series being (u/v), the ratio of drift and thermal speeds. This is very much appropriate for the consideration in the coronal loop. Using the smallness of (u/v), the distribution function is written in the form

$$f_{e,i} = \frac{n_0 g(r)}{\pi^{3/2}\left(V_0^{e,i}\psi_{e;i}\right)^3} \; \text{Exp}\left[-\frac{v^{2\cdot}}{\left(V_0^{e,i}\psi_{e,i}\right)^2}\right] \times$$

$$\left[1 + \frac{2u_z^{e,i}}{V_0^{e,i}}\sum_{n=1}^{\infty}\sum_{m=0}^{\infty} c_{nm}\left(\frac{v_z}{v_0^{e,i}}\right)^n \left(\frac{v}{v_0^{e,i}\psi_{e,i}}\right)^{2m}\right] \quad (6.52)$$

where ψ_e describes the spatial variation of electron temperature and V_0^e the thermal speed on the axis (r=0). Since the equilibrium solutions are of interest it is assumed that $\psi_e = \psi_i = \psi$ and $\beta_e = \beta_i$, i.e., the electrons and ions have identical temperature profiles. Since the density variation is generally steeper than temperature variation $\beta_e = \beta_i = -\beta$, where $c_{10} = 1$ and $c_{11} = -\beta$. This equation converts Vlasov equations into ordinary differential equations in g and ψ, in addition to providing relations that

165

determine all c_{nm} in terms of the plasma parameters. c_{nm} $\sim (u_0/v_0)^n$.

Using $u_0/v_0 \ll 1$ which is true for high temperature laboratory fusion plasma, the series is truncated keeping terms only to order u_0/v_0. Thus a simplified distribution function is obtained.

$$f_\alpha = \frac{n_0}{\pi^{3/2}(V_{0\alpha})^3} \frac{g}{\psi_\alpha^3} \left[1 + 2\frac{u_{0\alpha}}{v_{0\alpha}^2} V_z \left\{ 1 + \beta_\alpha \left(\frac{V}{V_{0\alpha}\,\psi_\alpha} \right)^2 \right\} \right]$$

$$\times \text{Exp} \left\{ \frac{-V^2}{V_{0\alpha}^2\,\psi_\alpha^2} \right\} + 0 \left\{ \frac{u_0^2}{v_0^2} \right\} \tag{6.53}$$

Since plasma has current only in the Z direction the self magnetic field has only the B_θ component. The equilibrium Vlasov equation is :

$$V_r \frac{\partial f}{\partial r} + \frac{q}{m} \left[V \times \hat{e}_\theta \frac{B_\theta}{c} \right] \cdot \frac{\partial f}{\partial V} = 0 \tag{6.54}$$

All variations are allowed only in the radial direction. For f as defined in equation (6.52).

166

$$\frac{\partial f}{\partial \mathbf{V}} = \mathbf{V}F_1 + \hat{e}_z F \tag{6.55}$$

Using this in equation (6.54)

$$V_r \frac{\partial f}{\partial r} + \frac{q}{m} (\mathbf{V} \times \hat{e}_\theta \frac{B_\theta}{c}) \cdot [\mathbf{V} F_1 + \hat{e}_z F] = 0 \tag{6.56}$$

or

$$V_r \frac{\partial f}{\partial r} + \frac{q}{mc} V_r B_\theta F = 0 \tag{6.57}$$

Using equation (6.52), $\partial f/\partial r$ and F are calculated as follows:

$$\frac{\partial f}{\partial r} = K \left| \left[\frac{d}{dr}\left(\frac{g}{\psi^3}\right) + \frac{g}{\psi^3} \frac{V^2}{V_0^2} \frac{2}{\psi^3} \frac{d\psi}{dr} \right] \times \right.$$

$$\left[1 + \frac{2u_0}{v_0} \sum_{n=1}^{\infty} \sum_{m=0}^{\infty} c_{nm} \left(\frac{V_z}{V_0}\right)^n \left(\frac{V}{V_0 \psi}\right)^{2m} \right] -$$

$$\left. \frac{2u_0}{V_0} \frac{g}{\psi^3} \sum_{n=1}^{\infty} \sum_{m=0}^{\infty} c_{nm} \left(\frac{V_z}{V_0}\right)^n \left(\frac{V}{V_0 \psi}\right)^{2m} \frac{2m}{\psi} \frac{d\psi}{dr} \right| \tag{6.58}$$

167

$$F = K \; \frac{g}{\psi^3} \; \frac{2u_0}{V^2} \; \sum_{n=1}^{\infty} \; \sum_{m=0}^{\infty} \; c_{nm} \; n \left(\frac{V_z}{V_0}\right)^{n-1} \left(\frac{V}{V_0 \psi}\right)^{2m} \tag{6.59}$$

Substituting for $\partial f / \partial r$ and F in equation (6.57), for $n = 1$ and $m = 0$

$$\left[\frac{d}{dr} \left(\frac{g}{\psi^3}\right) + \frac{g}{\psi^3} \frac{V_z^2}{V_0^2} \frac{2}{\psi^3} \frac{d\psi}{dr} \right] \; x$$

$$\left[1 + \frac{2u_0}{V_0} \frac{d}{dr} \frac{g}{\psi^3} c_{10} \left(\frac{V_z}{V_0}\right) + \frac{2u_0}{V_0} \frac{g^2}{\psi^3} \frac{V^2}{V_0^2} \frac{2}{\psi^3} \frac{d\psi}{dr} c_{10} \frac{V_z}{V_0} \right] +$$

$$\left[\frac{q}{mc} B_\theta \; \frac{g}{\psi^3} \frac{2u_0}{V_0^2} c_{10} \right] = 0 \tag{6.60}$$

Equating the terms independent of V_z

$$\frac{\psi^3}{g} \frac{d}{dr} \left(\frac{g}{\psi^3}\right) + \left[\frac{q}{mc} B_\theta \; \frac{g}{\psi^3} \frac{2u_0}{V_0^2} c_{10} \right] = 0 \tag{6.61}$$

And for $n = 1$, $m = 1$ we get

168

$$\left| \frac{d}{dr}\left(\frac{g}{\psi^3}\right) + \frac{g}{\psi^3}\left(\frac{V}{V_o\psi}\right)^2 \frac{2}{\psi}\frac{d\psi}{dr} \right| + \left| \frac{q}{mc} B_\theta \frac{g}{\psi^3} \frac{2u_0}{V_0^2} c_{11}\left(\frac{V}{V_o\psi}\right)^2 \right| +$$

$$\left| \frac{2u_0}{V_0} \frac{d}{dr} \frac{g}{\psi^3} \; c_{11}\left(\frac{V_z}{V_0}\right)\left(\frac{V}{V_o\psi}\right)^2 \right| \quad = \quad 0 \qquad (6.62)$$

Equating the coefficients of $\left(\dfrac{V}{V_o\psi}\right)^2$

$$\frac{g}{\psi^3} \frac{2}{\psi} \frac{d\psi}{dr} + \frac{q}{mc} \frac{g}{\psi^3} \frac{2u_0}{V_0^2} B_\theta \, c_{11} \;=\; 0 \qquad (6.63)$$

From (6.61) $\qquad \dfrac{\psi_\alpha^3}{g} \dfrac{d}{dr}\left[\dfrac{g}{\psi_\alpha^3}\right] \;=\; -\dfrac{u_{0\alpha}q_\alpha}{T_{\alpha 0}c} B_\theta$

where $T_{\alpha 0} = 1/2mv_0^2 \qquad$ and $c_{10} = 1$

The above equation on simplification yields

$$\frac{1}{g} \frac{dg}{dr} - \frac{3}{\psi_\alpha} \;=\; -\frac{u_{0\alpha}q_\alpha}{T_{\alpha 0}c} B_\theta \qquad (6.64)$$

169

Using equation (6.63) and $c_{11} = -\beta$

$$\frac{2}{\psi_\alpha} \frac{d\psi_\alpha}{dr} = -\frac{u_{o\alpha}q_\alpha}{T_{\alpha o}c} B_\theta \beta_\alpha \qquad (6.65)$$

combining equation (6.64) and (6.65)

$$g = \psi^{[-2/\beta_\alpha + 3]} \qquad (6.66)$$

using the value of g from (6.49) the profile function ψ and g are

$$\psi = \left[1 + \frac{r^2}{4\delta^2_{eff}} \right]^{-(2\beta_\alpha)/(3\beta_\alpha - 2)} \qquad (6.67)$$

$$g = \left[1 + \frac{r^2}{4\delta^2_{eff}} \right]^{-2(3\beta_\alpha - 2)/(5\beta_\alpha - 2)} \qquad (6.68)$$

$$b\delta_{eff} = \left\{ \frac{5\beta}{2} - 1 \right\}^{-1} \frac{(r/\delta_{eff})}{\left[1 + r^2/4\delta^2_{eff} \right]} \qquad (6.69)$$

170

where $\delta_{eff} = \left(2\delta_e/5\beta - 2 \right)$

The temperature

$$T \propto \psi^2 = \left[1 + r^2/4\delta^2_{eff} \right]^{-4\beta/5\beta - 2} \qquad (6.70)$$

The current density

$$J_z \propto g\psi^2 = \left[1 + r^2/4\delta_{eff} \right]^{-2} \qquad (6.71)$$

The pressure

$$p \propto g\psi^2 = \left[1 + r^2/4\delta_{eff} \right]^{-2} \qquad (6.72)$$

The plot of variation of density profile $g(r)$, magnetic field profile function $b\delta_e$ and temperature profile function ψ^2 versus $x = r/\delta_e$ for $\beta = 0.5, 0.8$ and 0.2 are shown in Figures 6.3, 6.4, 6.5; 6.6, 6.7, 6.8 and 6.9, 6.10 and 6.11 respectively. The graphs indicate that depending on the β value the radial variation can be positive or negative. Thus for $\beta > 2/3$, both density and temperature fall away from the axis as in Figure 6.9 and 6.11.

171
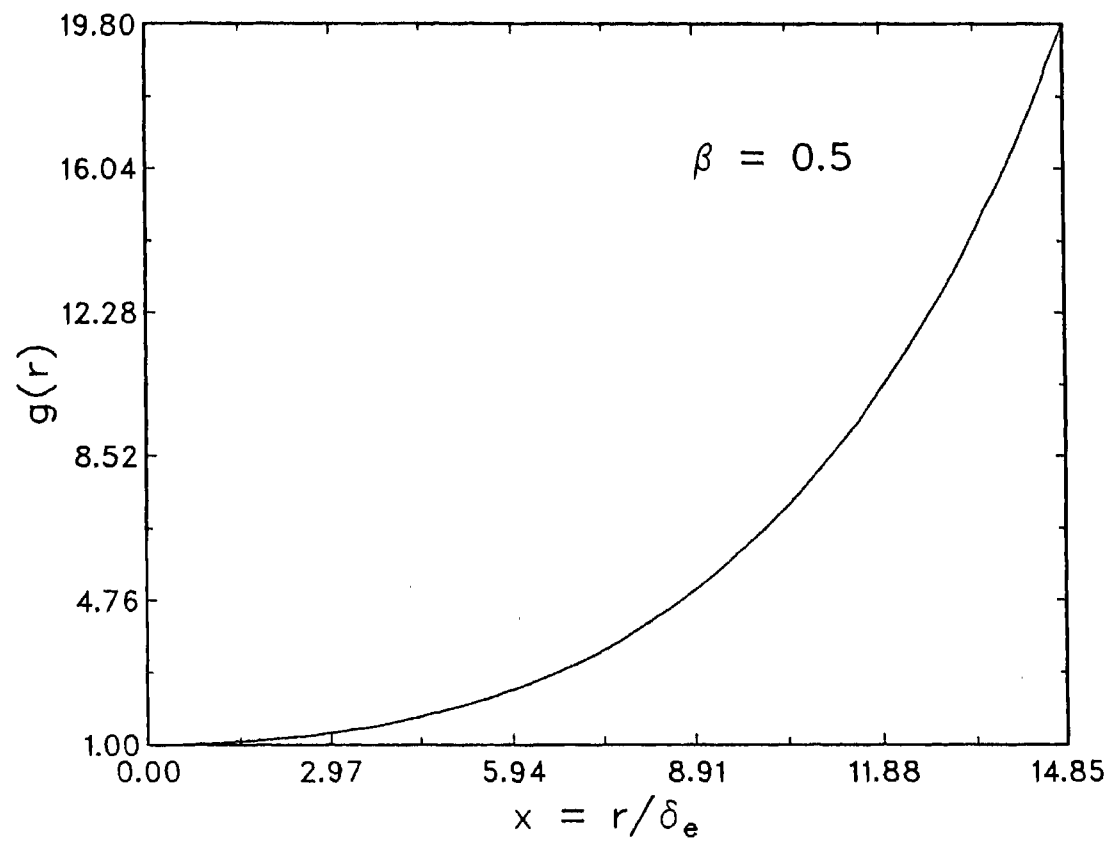
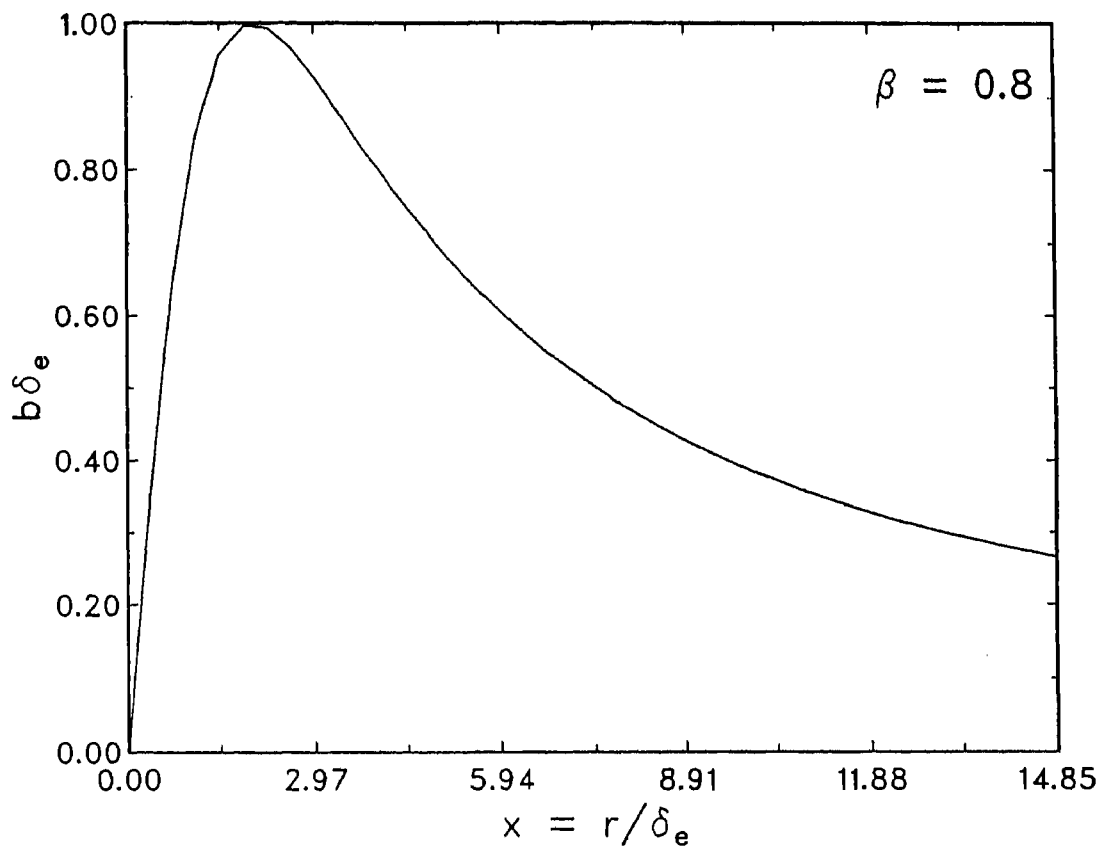Fig.6.3. Variation of density profile function $g(r)$
vs $x = r/\delta_e$.

172
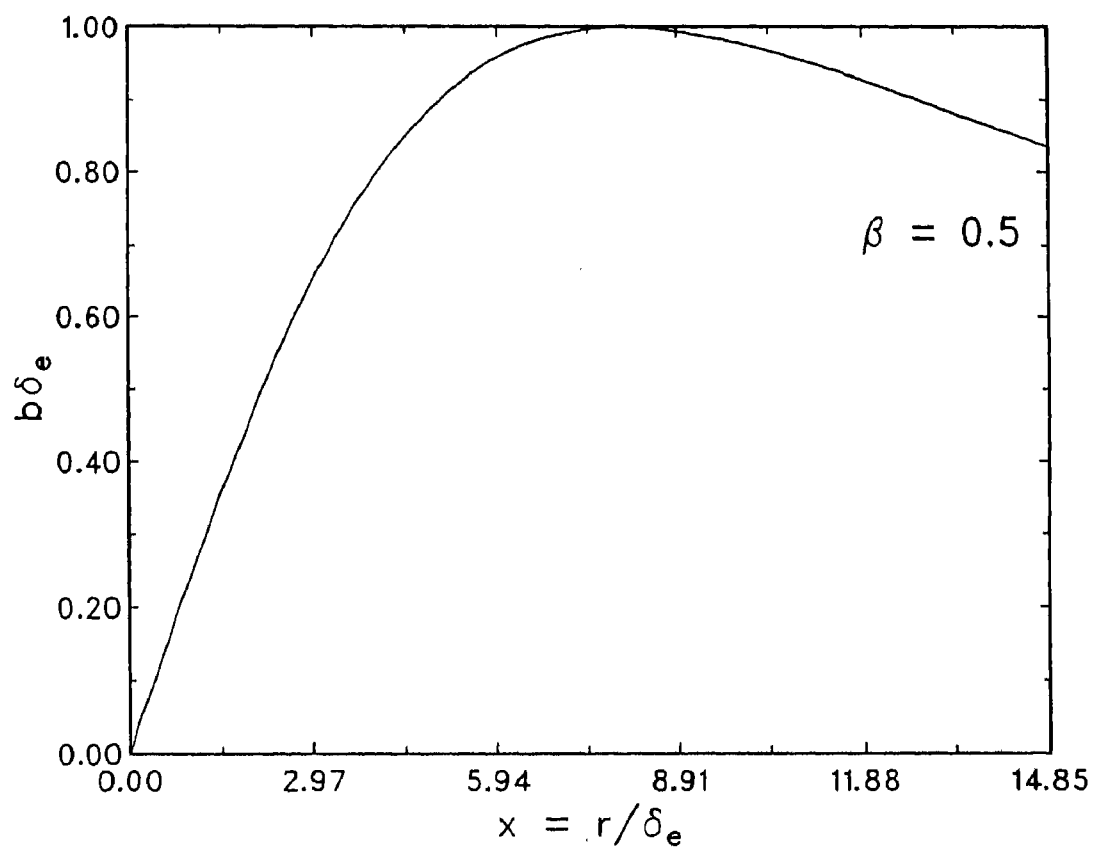
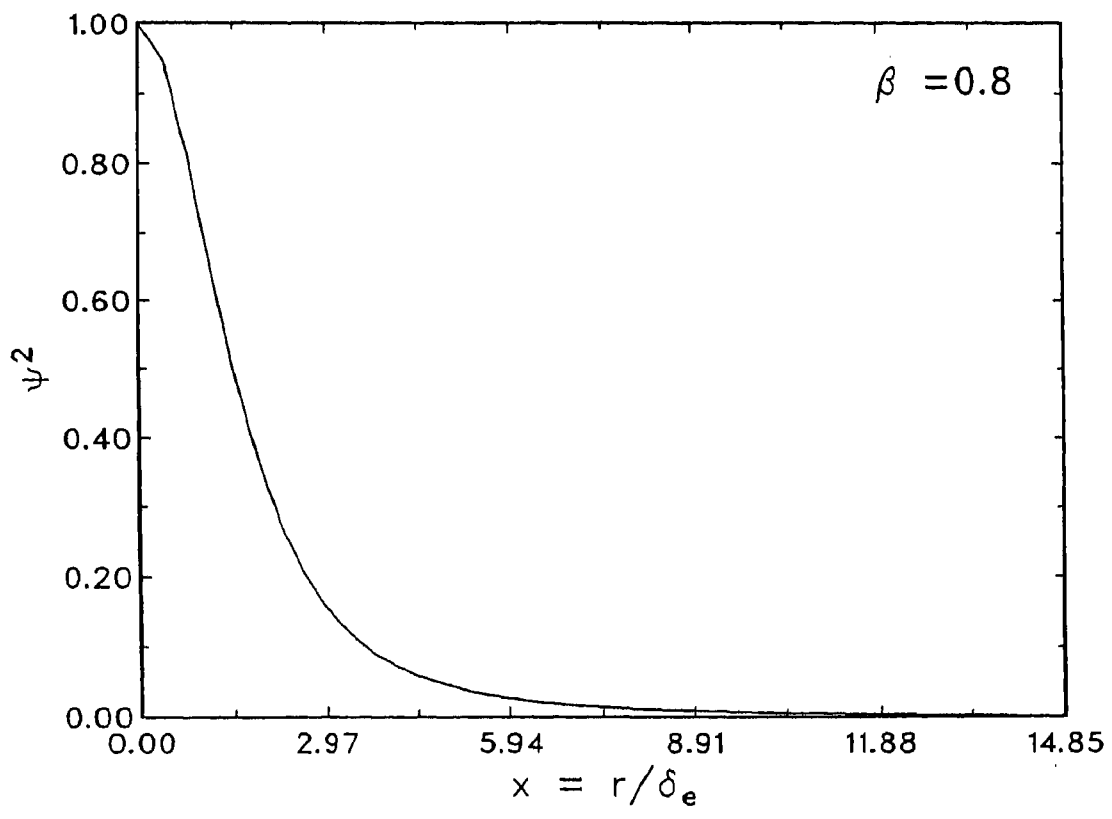**Fig.6.4.** Variation of magnetic field profile function $(b\delta_e)$ vs $x = r/\delta_e$.

173
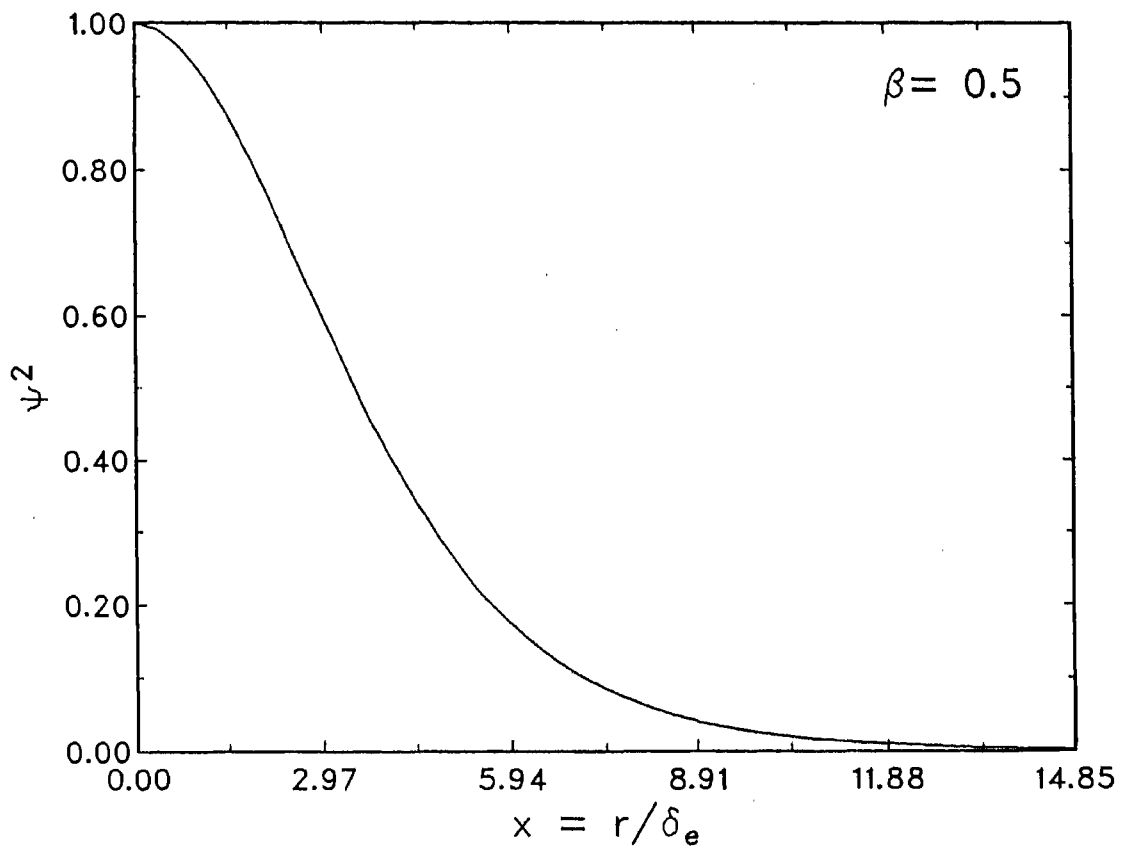
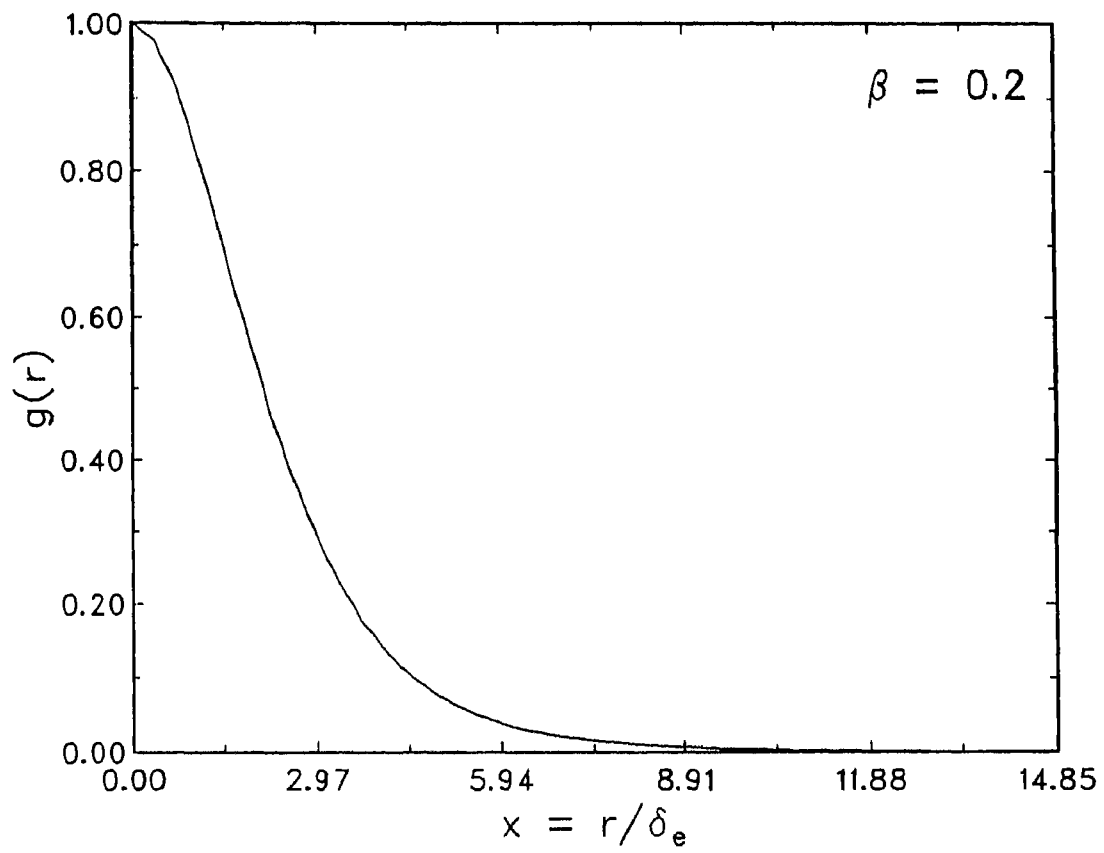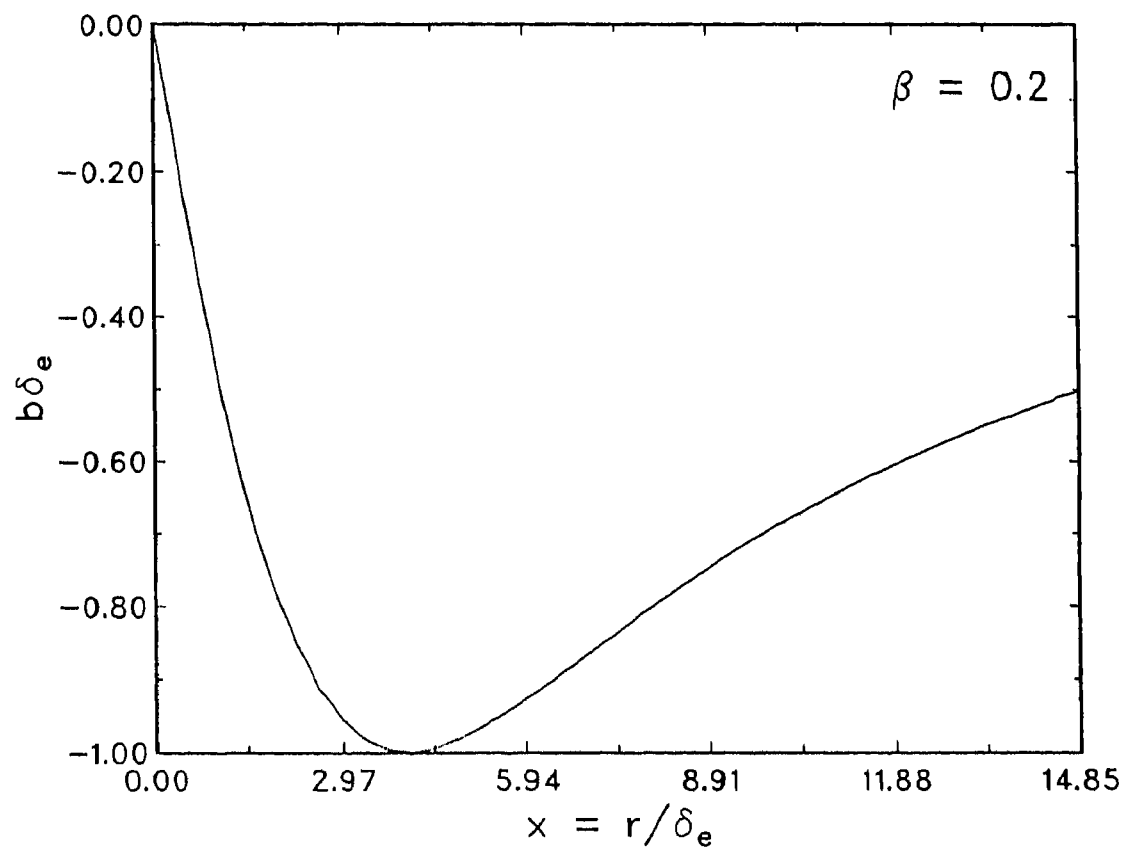Fig.6.5. Variation of temperature profile function ψ^2
vs $x = r/\delta_e$

$\beta = 0.8$

$x = r/\delta_e$
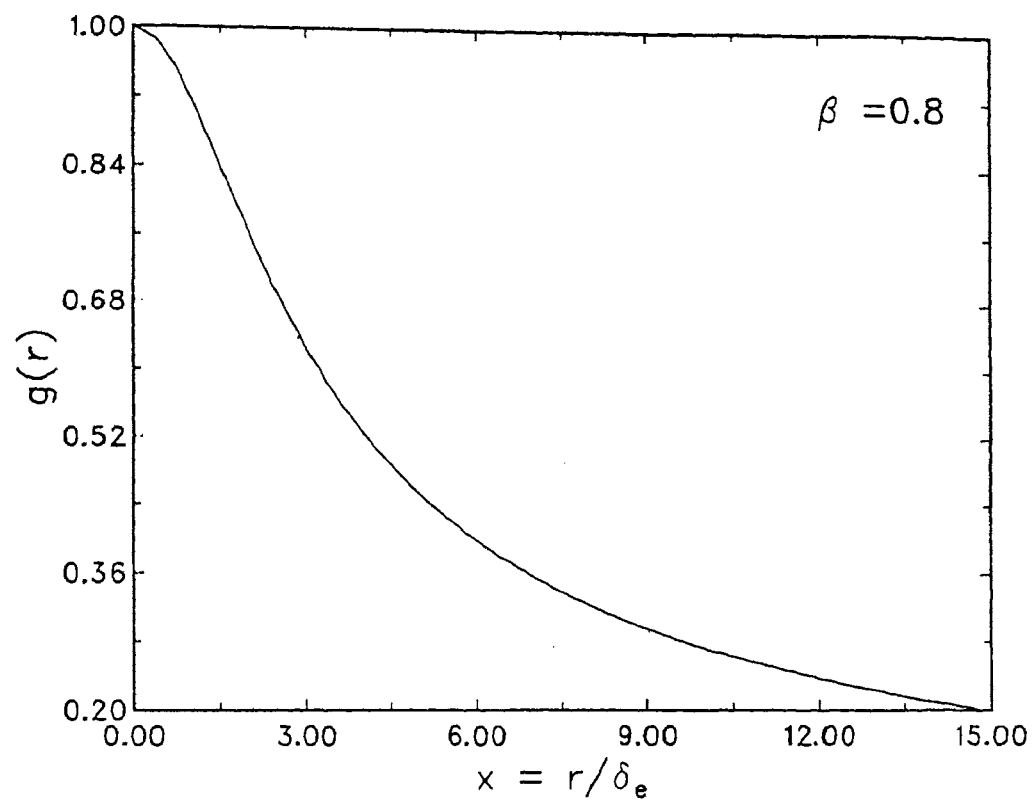
Fig.6.6 Variation of density profile function $g(r)$ vs $x = r/\delta_e$.

175

Fig. 6.7. Variation of magnetic field profile function
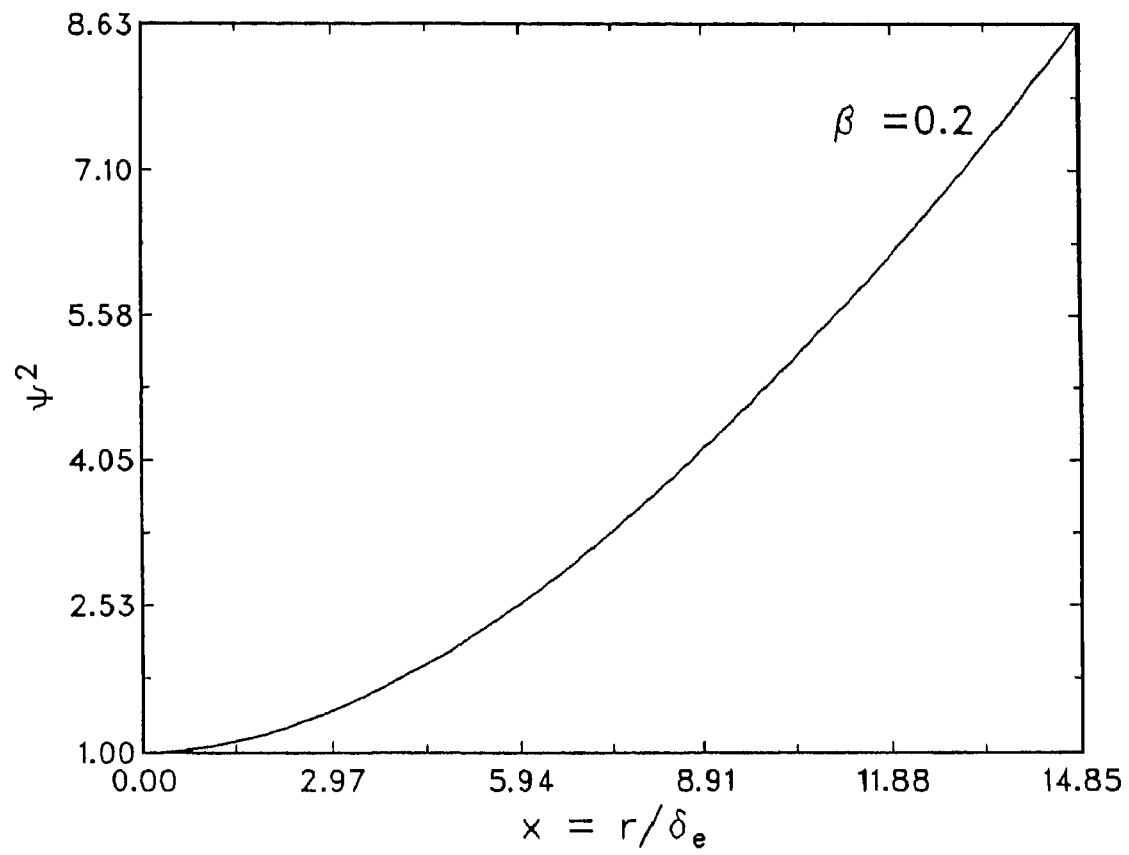$(b\delta_e)$ vs $x = r/\delta_e$.

176

Fig.6.8. Variation of temperature profile function ψ^2 vs $x = r/\delta_e$.

Fig.6.9. Variation of density profile function g(r) vs x = r/δ_e.

$\beta = 0.2$

Fig.6.10. Variation of magnetic field profile function $(b\delta_e)$ vs $x = r/\delta_e$.

Fig.6.11. Variation of temperature profile function ψ^2 vs $x = r/\delta_e$.

Whereas for $2/3 > \beta > 2/5$ the density increases and temperature decreases away from the axis as in Figure 6.6 and 6.8. For $\beta < 2/5$ the temperature increases towards the surface as in Figure 6.11. This is very much reminiscent of the cool core and hot sheath type loops observed by Foukal (1978) and Krieger, de Feiter & Vaiana (1976) and modelled through variational principle in MHD by Krishan (1983,1985). The parameter δ_e which characterises the spatial variations is related to the skin depth. The measure of δ_e determines the steepness and the extent of the current density profile. This satisfies the requirements laid down by the joule heating of the loop plasma.

6.5.4 VARIATION OF CURRENT DENSITY IN THE PRESENCE OF DENSITY AND DRIFT SPEED GRADIENTS:

In this case gradients in density and drift speeds are also allowed in addition to g. The drift speeds of the particles become a function of the radius r, i.e., $u_z \equiv u_{z0}\phi_e(r)$, where $\phi_e(r)$ is the profile of the electron, and u_{z0} is the drift speed at the center. The temperature T_e is kept independent of r. The Maxwellian of the form given by equation (6.35) with $u_{e,i}$ dependent on r will not allow a solution in the velocity space because $V_r(\partial f/\partial r)$ has additional terms, which are quadratic in the velocity

variables, which cannot be compensated by the force term. The compensating term is generated by introducing a temperature anisotropy: the particles have different temperatures in the direction along the current (T_z), and perpendicular to the current $(T$ not equal to $T_z)$. This allows the distribution function to be assumed as:

$$f_\alpha = \frac{n_0 g(r)}{\pi^{3/2} v_{e,\perp}^2 v_z^{e,\perp}} \; \text{Exp} \left[- \frac{v_r^2 + v_\theta^2}{v_e^2} - \frac{\left(v_z - u_{0z}^{e,\perp} \phi_e(r)\right)^2}{(v_z^{e,\perp})^2} \right] \qquad (6.73)$$

Equation (6.73) represents a neutral plasma $(g_e = g_i = g)$ carrying a current in the z direction. Here it has been assumed that $\phi_e = \phi_i = \phi$ with $\phi(r=0)=1$, and $g(r=0)=1$. Substituting equation (6.73) in the equilibrium Vlasov equation $(\partial/\partial t=0)$, and carrying out the usual algebra, the following set of coupled nonlinear ordinary differential equations in the variables g and ϕ are obtained.

$$\frac{1}{r} \frac{\partial}{\partial r} \left[r \frac{\partial \phi}{\partial r} \right] = - \frac{2\lambda}{\delta_e^2} \exp \left[\left(\frac{u_{0z}^e}{v_z^e} \right)^2 (\phi^2 - 1) \right] \qquad (6.74)$$

$$g(r) = \exp \left[\left(\frac{u_{0z}^e}{v_z^e} \right)^2 (\phi^2 - 1) \right] \qquad (6.75)$$

182

where,

$$\lambda = (v_e^2 - v_z^2)/2(u_{0z}^e) \; = \; \frac{T_e - T_{ez}}{m_e(u_{0z}^e)^2} \; = \; \frac{\Delta T_e}{2T_e} \frac{v_e^2}{(u_{0z}^e)^2} \qquad (6.76)$$

The numerical solution of the equation (6.74) yields a rich variety of profiles as λ is varied. Since the spatial behavior of the density, the magnetic field and the current density are essentially a function of the dimensionless parameter λ, there is need only to provide appropriate normalization. For coronal loops, the anisotropy parameter

$$\frac{\Delta T_e}{2T_e} \frac{v_e^2}{(u_{0z}^e)^2} = 1.8 \times 10^3 \frac{\Delta T_e}{T_e} \quad ,$$

For $\lambda = 5 \quad \dfrac{\Delta T_e}{T_e} = 2.7 \times 10^{-3}$ which is reasonably small.

A plot of the variation of the density (Ref. Mahajan, 1989) profile function $g(r)$ versus $x = r/\delta_e$, indicates that indicates that g decreases monotonically with x, starting from zero, raises to a maximum at $x=2$ and then slowly goes to zero. For larger values of λ, g becomes oscillatory with the wavelength of the oscillations

183

decreasing with λ. The fact that density becomes less and less peaked indicates loss of confinement, a direct consequence of the fact that the confining magnetic field (oscillatory) becomes considerably smaller than its $\lambda = 0$ value.

A plot of the variation of the current profile function (gue) versus $x = r/\delta_c$. The profiles indicate that the current density appears in the form multisheaths for large values of the anisotropy parameter (for $\lambda=5$) while the corresponding density profile is almost flat. (Ref Mahajan,1989).

SUMMARY:

A Vlasov-Maxwell description of coronal loop plasma admits a variety of equilibrium spatial profiles of mass density, current density, the temperature, and the magnetic field depending upon the type of inhomogeneities allowed. The profiles vary from being flat to spiky and resemble the ones derived from EUV and X-ray coronal observations. The current frofile of small widths are the outcome of the exact solutions of Vlasov-Maxwell system. The multisheath current profiles derived in this chapter complement the magnetohydrodynamic study of current sheet formation well. Further

184

from the above discussion it is found that the Vlasov description allows the determination of density and temperature profiles individually unlike in the fluid description where equation of state is required to study the separate variations of density and temperature from the pressure profile.

7 SUMMARY OF THE RESEARCH

7.1.STEADY STATE STRUCTURE:

The loop or arch like configurations of the solar active regions have been seen in the emissions at UV,EUV and X-ray wavelengths,(Foukal,1978). The current carrying plasma in the loop supports a helical form of the magnetic fluid. The steady state pressure structure of a solar coronal loop was studied using the theory of MHD turbulence in cylindrical geometry. The magnetic and velocity fields were expanded in terms of C-K functions using the MHD equations assuming the plasma as a incompressible fluid. In chapter **4**, the study was confined to the steady state solutions to the pressure i.e., $\partial/\partial t(\eta,\xi) = 0$ and $\eta = \xi$, where η and ξ are the expansion coeffiecients. The pressure profile was discussed under two considerations:

1)Pump approximation; where one of the three modes was considered as the strongest, as compared to the other two, and

2)The mode strength varying in proportion to their spatial scales. The plasma was assumed to be a cylindrical column of length L and

radius R.

The analysis of the results indicate that the radial
variation of pressure is found to be maximum at the foot points of
the loop and is minimum at the apex (See fig. 4.1). This result is
in conformity with the results of Levine and Withbroe(1977),
wherein they have indicated that the coronal loops undergoing
dynamic changes are characterised by a temperature structure in
which there is a cool core relative to the substantially hot
surrounding sheath.

The axial variation of pressure indicates, that the
maximum values of pressure is attained near the apex for all radial
positions(see fig. 4.2). This is in agreement with the results of
Rosner et al (1978). The pressure is found to increase uniformly
for all values of the radial distance at different azimuthal
angles(see fig. 4.3). The azimuthal variation of pressure for
different radial distances indicate oscillatory behavior, which is
predominant near the surface.

The density plots fig 4.6a and 4.6b indicate that the
region of maximum pressure is not necessarily at the apex. Further
it is also an indication of the observed cool core and hot sheath
features of the coronal loops.

187

Even when the mode strengths is assumed to vary in proportion to their spatial scales, the results like an increase of pressure towards the surface and the existence of maximum somewhere along the length of the loop emerge as the general features of the loop. In all cases it was found that the representation of the velocity and magnetic fields by a three mode C-K functions bring out the three dimensional features of the pressure profile. The choice of the triads representing the variation of velocity and magnetic fields on the largest spatial scales permitted by the system, provides a fairly realistic description of the loop plasma.

7.2. TEMPORAL EVOLUTION OF PRESSURE:

In chapter 5, the velocity and magnetic fields were allowed time dependence to facilitate the study of their evolution. The complete dynamics was described by a set of infinite coupled and non linear ordinary differential equations which are of the first order in time for the expansion coefficients of velocity and magnetic fields. Since the evolution equations are coupled and nonlinear, the dependence of their solution on the initial condition was expected to reveal chaotic behavior. An important tool in the investigation of this was the study of power spectrum

188

of the data generated by the solution of the MHD equations and to evaluate the invariant dimensions especially the second order correlation dimension of the attractor D_2 of the system.

The analysis of the results indicate that when the values of velocity and magnetic field coefficients η's and ξ's are very nearly equal, the spectrum is discrete indicating that the pressure profile has a finite number of frequencies. The marginal stability exists only for the time scales for which the linearisation is valid. Though microwave and X-ray regions observation show a quasi periodic oscillations, the observed power spectrum of pulsations actually exhibits a more complex behavior if finer variations are ignored. The quasi periodic behavior is expected only near equilibrium.

Under large departures from the equilibrium, a loop shows a complex temporal structure which can only be described in terms of objects with fractal dimensions in the phase space of the velocity and magnetic field. Coronal loops being continuously subjected to external forcing through their foot points and through interaction with neighboring regions are likely to be in a chaotic state of pressure fluctuations. Hence, when there are large deviations from equilibrium the system and the time evolution of the pressure is non linear.

189

In the pump approximation case, since the variations of the strongest mode is negligible when compared with other modes the interaction is between less number of modes of oscillations and the system shows oscillatory behavior, unlike the non linear case where chaotic behavior was exhibited by the superposition of more than two modes of oscillations and due to strong nonlinear coupling between them. This fact is evident in the evaluation of D_2 (see fig.5.5). As one proceeds from the axis towards the surface, the dynamics shows the development of strange attractors ending up in complete randomness (see fig.5.6). This requires a finer analysis. Thus the time scale over which the system is stable or otherwise can be inferred only by evaluating the Lyapunov constants which are sensitive to the initial conditions. Inverting the problem, by specifying the Lyapunov constants, it may be possible to evaluate the class of initial states which can give the observed life time of the loops.

7.3. VLASOV-MAXWELL EQUILIBRIA:

Vlasov-Maxwell equilibria of solar coronal loops was discussed in Chapter 6. The results of the study indicate a complex type of radial variation profile of density, magnetic field

and temperature. Temperature profiles are found to increase towards the surface reminiscent of the cool core and hot sheath features in the coronal loops. The current profile of small widths are the outcome of the exact solutions of the Vlasov-Maxwell system as is evident from the discussion in chapter 6. Further, it is found that a Vlasov-Maxwell description of coronal loop plasma admits a variety of equilibrium spatial profiles of mass density, current density, temperature and magnetic field depending on the inhomogeneities allowed. Also this description allows the determination of the density and temperature profiles individually, in contrast to the fluid description where the equations of state is required to extract the separate variations of density and temperature from the pressure profile.

8 REFERENCES

Abraham,N.B..et al.(1986).Physics Letters,A114,217

Alissandrakis,C.E.(1981). Astronomy and Astrophysics,100,197-200.

Aschwanden,M.J (1987),Solar Physics,111,113.

Athay.R.G.,Gurman.J.B. & Henze.W.(1983). Astrophysical Journal.269 706-14.

Atmanspacher,H.and Scheingraber,H.(1986),Physical Review,A34,253.

Bernstein,B.,Greene,J.M. & Kruskal,M.D.(1957). Physical Review, 108,546.

Bray,R.J.,Cram,L.E.,Durrant,C.J. & Loughhead,R.E.(1991). Plasma loops in the Solar Corona.Cambridge University Press.

Bray,R.J. & Loughhead,R.E.(1983). Solar Physics,85, 131-40.

Brueckner,G.E. & Bartoe,J.D.F.(1974). Solar Physics,38,135-56.

Bumba.V. & Kleczek.J.(1961). Observatory, 81, 141-3.

Chandrasekhar,S. & Kendall,P.C.(1957).Astrophysical Journal,126, 457-60.

Chen,Z.C. & Chen,Y.(1989). Solar Physics,119,279-99.

Chen,H.,Shan,X.,and Montgomery,D.(1990),Physical Review.A42,6158.

Cheng,C.C.(1980). Solar physics,65,347-56.

Cheng,C.C.,Smith,J.B.,& Tandberg-Hanssen,E.(1980).Solar Physics,

67, 259-65.

Chiu, Y. T. & Hilton, H. H. (1977). Astrophysical Journal, 212, 873-75.

Dahlburg, J. P., Montgomery, D., Doolen, G. D., & Turner, L. (1986), Physical Review Letters, 57, 428.

Dahlburg, J. P., Montgomery, D., Doolen, G. D., & Turner, L. (1987), Journal of Plasma Physics, 37, 299.

Dahlburg, J. P., Montgomery, D., Doolen, G. D., & Turner, L. (1988), Journal of Plasma Physics, 40, 39.

Dere, K. P. (1982). Solar Physics, 75, 189-203.

Dunn. R. B. (1971). Coronal events observed in 5303 A in Physics of the Solar Corona. ed. C. J. Macris. pp. 114-29. Dordrecht: Reidel.

Ellison, M. A. (1944). Monthly notices of the Royal Astronomical Society, 104, 22-32.

Foukal, P. (1975). Solar Physics, 43, 327-36.

Foukal. P. (1978). Astrophysical Journal, 223. 1046-57.

Foukal, P. V. (1976). Astophysical Journal, 210, 575-81.

Grassberger, P. and Procaccia, I. (1983). Physical Review, Lett. 50, 346

Harris, (1962). Nuovo Cimento, 23, 1167.

Hollweg, J. V. (1981). In Solar active regions, p. 277, ed. Orrall. F. Q. Colorado Associated University Press.

Hood, A. W. & Priest, E. R. (1979), Astronomy & Astrophysics, 77, 233.

Karpen, J. T., Antiochos, S. K. & de Vove, C. R., (1990), Astrophysical Journal, 356, L7.

Kleczek. J. (1963). Rainy loops from october 22, 1956,. Bulletin of

the Astronomical Institutes of Czechoslovakia., 14.167-71.

Krieger,A.S.,de Feiter,L.D.& Vaiana,G.S.(1976). Solar Physics, 47,117.

Krishan,V.(1983a)in Proceedings of the Spring College on Radiation ir Plasmas,Trieste,Italy

Krishan,V.(1983b). Spatial profiles of lines in active region loops.Solar Physics,88,155-161.

Krishan,V.(1985). Statistical Mechanics of velocity and magnetic fields in solar active regions. Solar Physics,95,269-80.

Krishan.V.,Berger,M.and Priest,E.R.(1988),in R.C.Altrock(eds.) Solar and Stellar Coronal Structures and Dynamics, National Solar Observatory

Krishan,V.,Sreedharan,T.D.and Mahajan,M.(1991)Monthly Notices of Royal Astronomical Society,249,596-601.

Lategan.A.H. & Jarrett.A.H.(1982). Solar Physics. 76, 323-30.

Laval,G.,Pellat,R. & Vuillemin. In plasma Physica and controlled Nuclear Research,Vol.2,p.259.

Levine,R.H & Altschuler,M.D.(1974). Solar Physics,36,345.

Levine,R.H.and Withbroe,G.L.(1977). Solar Physics,51,83-101.

Louhhead,R.E. & Bray,R.J.(1984). Astronomical Journal, 283,392-7.

Loughhead,R.E.,Bray,R.J. & Wang,J.L.(1985). Astrophysical Journal, 294,697-701.

Low,B.C.,(1987),Astrophysical Journal,323,358.

Low,B.C. & Wolfson,R.,(1988).Astrophysical Journal,324,574.

Mahajan,S.M.,(1989).Physics of Fluids,B1,1,43.

Martin.S.F.(1973).Solar physics,31,3-21.

Marx,K.D.(1969). Physics of fluids,11,357.

Montgomery,D.,Turner,L. and Vahala,G.(1978). Physics of Fluids, 21,757-64.

Moore,R. & 15 co-authors (1980). The thermal X-ray flare plasma. Insolar flares,ed.P.A.Sturrock. pp.341-409.Boulder; Colarado Associated University Press.

Parker,E.N.(1983).Astrohysical Journal.264,635.

Parker,E.N.(1987).Astrohysical Journal.318,876.

Pfirsh,D.Naturforsch,Z.(1962). Teil A 17,861.

Poletto,G., Vaiana,G.S., Zomback,M.V., Krieger,A.S., & Timothy,A.F. (1975).Solar Physics,44,83.

Priest,E.R.(1978). Solar Physics,58,57.

Priest,E.R.(1981),E.R Priest(ed). Solar Flare Magnetohydrodynamics, Gordon and Breach,N.Y pp.2 and 139.

Roberts,B.,Edwin,P.M.and Benz,A.O.(1984) Astrophysical Journal, 279,857.

Rossener,R.& Golub,L.,Coppi,B.& Vaiana,G.S.(1978). Astrophysical Journal,222,317-332.

Rossener,R. & Tucker,W.H.& Vaiana,G.S.(1978). Astrophysical Journal,220,643-665.

Roussel-Dupre,R.,Wrathall,J.,Nicholas,K.R.,Bartoe,J.D.F. & Brueckner,G.E.(1984). Astrophysical Journal,278,428-40.

195

Sasidharan,K.,Sreedharan,T.D.,Pratap,R. & Krishan,V.(1995).Solar Physics,0(in press)1-13.

Shan,X.,Montgomery,D. & Chen,H.(1991),Physical Review,A44

Seechi.A.(1875-7). Le Soleil. 2nd Ed. Paris: Gauthier-Villars.

Sheely,N.R. & 5 co-authors. (1975). XUV observations of coronal magnetic fields, Solar Physics,40,103-21.

Sreedharan,T,D., Sasidharan,K., Sathyanarayanan,A. & Krishan,V. Solar Physics,142,249.

Svestka,Z.,1994,Solar Physics,152,505.

Tandberg-Hanssen,E. (1974). Solar prominences. Dordrecht:Reidel.

Tandberg-Hanssen,E. (1977). Prominences. In illustarted glossary of Solar and Solar-Terrestrial Physics,ed.A.Bruzek & C.J. Durrant,pp. 97-109.

Theobald,M.L., Montgomery,D., Doolen,G.D., & Dahlburrg,J.P.,(1989) Physics of Fluids,B1,766.

Tsinganos,K.C.(1982). Astrophysical Journal,259,820.

Vaiana,G.S.& Rosner,R.(1978).Astronomy & AstroPhysics,16,393-428.

Van Ballegooijen,A.A.,(1985). Astrophysical Journal,298,421.

Van Ballegooijen,A.A.,(1986). Astrophysical Journal,311,1001.

Vrsnak.B.(1984). Solar Physics,94.289-97.

Yoshida,Z. & Giga,Y.M.(1990). Math.Z.204,235.

Young.C.A.(1895). The Sun. London: Kegan Paul

196

APPENDIX

LIST OF PUBLICATIONS.

1.KRISHAN,V. ,SREEDHARAN,T.D. & MAHAJAN,M.(1991).Monthly Notices of
   Royal Astronomical Society,249,596-601.

2.SREEDHARAN,T.D. ,SASIDHARAN,K. ,SATHYANARAYANAN,A. & KRISHAN,V.
   (1992).Solar Physics,142,249-264.

3.SASIDHARAN,K. ,SREEDHARAN,T.D.,PRATAP,R. & KRISHAN,V.(1995).
   Solar Physics,(in Press).

Vlasov–Maxwell equilibria of solar coronal loops

V. Krishan and T. D. Sreedharan
Indian Institute of Astrophysics, Bangalore 560034, India

Swadesh M. Mahajan
Institute for Fusion Studies, The University of Texas at Austin, Austin, Texas 78712, USA

SUMMARY

A Vlasov–Maxwell description of the ubiquitous solar coronal structures is presented. It is found that an equilibrium plasma configuration can live with spatial gradients in density, temperature, current and drift speeds of the charged particles. Any stability study must be carried over this inhomogeneous equilibrium state. In addition, the Vlasov description admits the investigation of kinetic processes like heating and radiation and unlike a fluid description, it does not require an equation of state to determine the individual variations of temperature and density.

1 INTRODUCTION

Solar coronal loops have been studied conventionally through magnetohydrodynamic processes, since their shapes betray the underlying magnetic fields. Coronal loops are especially favoured for their ability to pick up energy from the convection zone and deposit it in the corona. The foot points of the loops suffer continuous turning and twisting, producing complex magnetic geometry in which current sheets have been shown to form. One believes that ohmic dissipation of current in these sheets can maintain a $\sim 10^6$ K corona. Attempts to show the formation of extremely small-scale current sheets have been carried out by Parker (1983, 1987), Low (1987), Low & Wolfson (1988), Van Ballegooijen (1985, 1986), Karpen, Antiochos & De Vove (1990) and many more. The MHD equilibria of coronal loops have been investigated by Priest (1981), Hood & Priest (1979), Vaiana & Rosner (1978), Tsinganos (1982), Krishan (1983, 1985) and Krishan, Berger & Priest (1988). In this paper, we explore a Vlasov–Maxwell treatment of a current-carrying cylindrical plasma. In this description, it is possible to derive the spatial profiles of equilibrium plasma parameters and the exact particle velocity distributions without invoking equations of state and the exact particle velocity distribution functions. It is found that the system develops strongly-peaked current density profiles under very commonly occurring conditions. It is perhaps the disturbance of these current density configurations that leads to the heating and acceleration of particles in coronal loops.

2 VLASOV–MAXWELL EQUILIBRIA

We will closely follow the recent work of Mahajan (1989) on Vlasov–Maxwell equilibria for several systems, the exemplary cases being Z pinches and Tokamaks. A coronal loop will be represented by a cylindrical column of plasma with current density J_Z along the axis of the cylinder and with no gravity. The actual geometry of a coronal loop consists of the two ends (the foot prints) of the cylindrical plasma embedded in a sub-photospheric region. A small twisting motion of the foot points may introduce a small amount of azimuthal current J_θ which we neglect at present. The sub-photospheric region contains a high-β plasma where β is the ratio of gas kinetic pressure to magnetic pressure. As a result the magnetic field lines move on a time-scale much longer than the coronal time-scales. This line tying reduces the region of unstable excitations, especially those of long wavelength. The neglect of gravity reduces the coronal loop to an essentially horizontal cylinder. Of course, while studying the stability of an equilibrium, the end effects, gravity and curvature must be properly taken into account. The particle density n, the temperature T, and the particle drift speeds u are in general, spatially varying quantities. Here we allow all spatial variations only in the radial direction since there is observational evidence for such variations. The plasma is embedded in a uniform axial magnetic field, B_0. The relevant equations for an equilibrium system (with $\partial/\partial t = 0$) are

$$V_r \frac{\partial f_e}{\partial r} - \frac{e}{m_e}\left[E + \frac{V}{c} \times (B + \hat{e}_z B_0) \right] \cdot \frac{\partial f_e}{\partial V} = 0 \tag{1}$$

$$V_r \frac{\partial f_i}{\partial r} + \frac{e}{m_i}\left[E + \frac{V}{c} \times (B + \hat{e}_z B_0) \right] \cdot \frac{\partial f_i}{\partial V} = 0 \tag{2}$$

$$\frac{1}{r}\frac{\partial}{\partial r}(rB_\theta) = \frac{4\pi}{c} J_z \tag{3}$$

$$\nabla \cdot E = 0 \tag{4}$$

$$\mathbf{V} \times \mathbf{E} = 0 \tag{5}$$

$$J = -e \int d^3V \, v (f_e - f_i) \tag{6}$$

where $f_{e,i}$ are the single particle distribution functions, $(\mathbf{E}, \mathbf{B})$ are the self consistent fields. Equations (1) and (2) are collisionless Boltzman equations for electrons and ions describing the conservation of particles in phase space of positions and momenta. These are also known as Vlasov equations which are valid at high temperatures when Coulomb collisions can be neglected. In addition the fully ionized plasma considered here experiences only electromagnetic forces. All non-electromagnetic forces, such as gravity, are neglected. Further, the axial dependence of particle density is neglected. This is valid for loops of length smaller than the density scale height. Equation (3) is the axial component of Ampere's law describing steady state fields. Equation (4) is Poisson's equation under the condition of zero charge separation which is justified for an equilibrium study since charge separation occurs over extremely short time-scales such as those of electron plasma oscillation. Equation (5) is Faraday's Law for steady fields. Equation (6) defines current in terms of the particle distribution function for electrons and ions. Let a displaced Maxwellian of the form

$$f_{e,i} = \frac{n_0}{\pi^{3/2} v_{e,i}^3} \exp\left[-(V - u_z^{e,i})^2 / v_{e,i}^2 \right] g(r) \tag{7}$$

provide a self-consistent solution for equations (1)–(6). Here n_0 is the ambient density, $v_{e,i}^2 = 2T_{e,i}/m_{e,i}$ and $u_z^{e,i}$ are, respectively, the thermal speed and the drift speed, $T_{e,i}$ and $m_{e,i}$ are the temperature and mass and $g(r)$ is the density profile factor which is same for electrons and ions under the assumption of no charge separation.

Case I

The self-consistent solutions of equations (1)–(7) for the case when $g(r)$, describing the entire spatial variation are found to be

$$g(r) = [1 + r^2/4\delta_e^2]^{-2}. \tag{8}$$

and

$$b\delta_e = -\left(\frac{r}{\delta_e}\right)[1 + r^2/4\delta_e^2]^{-1} \tag{9}$$

where

$$b = \frac{eu_z^i B_\theta}{cT_e}; \quad \delta_e^2 = \frac{2c^2}{\omega_{pe}^2} \frac{V_e^2(1-\mu)^{-1}}{2(u_z^i)^2} \tag{10}$$

and

$$\mu = (u_z^i/u_z^e)$$

Here e is the charge, c is the speed of light and $\omega_{pe} = (4\pi n e^2/m_e)^{1/2}$ is the electron plasma frequency. Thus one obtains a density profile peaked at the axis with a characteristic length scale δ, which will be estimated in a later section.

Case II

Here, in addition to density gradient, the spatial variation of temperature is also allowed. The drift speeds $u_z^{e,i}$ are still

homogeneous. It has been shown (Mahajan 1989) that a series representation for the distribution functions gives a valid solution of the inhomogeneous Vlasov–Maxwell system, the expansion parameter for the series being (u/v), the ratio of drift and thermal speeds. This is appropriate for the considerations in coronal loops as discussed later. Using the smallness of (u/v), we write for the distribution function as

$$f_{e,i} = \frac{n_0 g(r)}{\pi^{3/2} (v_0^{e,i} \psi_{e,i})^3} \exp\left[-\frac{v^2}{(v_0^{e,i} \psi_{e,i})^2} \right]$$
$$\times \left[1 + \frac{2u_z^{e,i}}{v_0^{e,i}} \sum_{n=1}^{\infty} \sum_{m=0}^{\infty} c_{nm} \left(\frac{v_z}{v_0^{e,i}}\right)^n \left(\frac{v}{v_0^{e,i} \psi_{e,i}}\right)^{2m} \right] \tag{11}$$

where ψ_e describes the spatial variation of electron temperature and $v_0^{e,i}$ is the thermal speed on the axis $(r=0)$. Since we are interested in equilibrium solutions, we assume $\psi_e = \psi_i = \psi$ and $\beta_e = \beta_i$, i.e. the electrons and ions have identical temperature profiles. With the assumption that density variation is generally steeper than temperature variation, one can take $\beta_e = \beta_i = -\beta$, where $C_{10} = 1$ and $C_{11} = \beta$.

Using equation (11), and retaining terms only up to (u/v), one finds the profile functions as

$$\psi = (1 + r^2/4\delta_{eff}^2)^{-2\beta/5\beta - 2} \tag{12}$$

$$g = (1 + r^2/4\delta_{eff}^2)^{-2(3\beta-2)/5\beta - 2} \tag{13}$$

$$b\delta_{eff} = \left(\frac{5\beta}{2} - 1\right)^{-1} \frac{(r/\delta_{eff})}{(1 + r^2/4\delta_{eff}^2)} \tag{14}$$

where

$$\delta_{eff}' = (2\delta_e/5\beta - 2).$$

The temperature

$$T \propto \psi^2 = (1 + r^2/4\delta_{eff}^2)^{-4\beta/5\beta - 2} \tag{15}$$

The current density

$$J_z \propto g\psi^2 = (1 + r^2/4\delta_{eff}^2)^{-2} \tag{16}$$

The pressure

$$p \propto g\psi^2 = (1 + r^2/4\delta_{eff}^2)^{-2} \tag{17}$$

One observes that, depending upon the value of β, the radial variation can be positive or negative. Thus for $\beta > \frac{2}{3}$, both density and temperature fall away from the axis, whereas for $\frac{2}{3} > \beta > \frac{2}{5}$, the density increases and temperature decreases away from the axis. For $\beta < \frac{2}{5}$ the temperature increases towards the surface and this is very much reminiscent of the cool-core- and hot-sheath-type loops observed by Foukal (1978) and Krieger, de Feiter & Vaiana (1976), and modelled through variational principle in MHD by Krishan (1983, 1985). The other parameter, δ_e, which characterizes the spatial variations, is related to the skin depth. We shall see in a later section that the measure of δ_e, which determines the steepness and extent of the current density profile is commensurate with the requirements laid down by the joule heating of the loop plasma.

Case III

Here, we allow gradients in density and drift speed. It is found that the presence of temperature anisotropy permits a

displaced Maxwellian solution of the system where the distribution functions are given by

$$f_{\alpha} = \frac{n_0 g(r)}{\pi^{3/2} v_e^2 v_z^2} \exp\left\{-\frac{v_x^2 + v_y^2}{v_{e\perp}^2} - \frac{[v_z - u_{0z}^{e,i}\phi_{e,i}(r)]^2}{(v_z^{e,i})^2}\right\}$$ (18)

Here, we have taken $\phi_e = \phi_i = \phi$ with $\phi(r=0)=1$, and $g(r=0)=1$. The equations relating the density profile, $g(r)$, and the drift speed profile, ϕ, are found to be

$$\frac{1}{r}\frac{\partial}{\partial r}\left(r\frac{\partial \phi}{\partial r}\right) = -\frac{2\lambda}{\delta_e^2}\exp\left[\left(\frac{u_{0z}^e}{v_z^e}\right)^2(\phi^2-1)\right]$$ (19)

and

$$g(r) = \exp\left[\left(\frac{u_{0z}^e}{v_z^e}\right)^2(\phi^2-1)\right]$$ (20)

where

$$\lambda = (v_e^2 - v_z^2)/2(u_{0z}^e)^2 = \frac{T_e - T_{ez}}{m_e(u_{0z}^e)^2} = \frac{\Delta T_e}{2T_e}\frac{v_e^2}{(u_{0z}^e)^2}$$ (21)

Equation (19) has been solved numerically and here we will reproduce some of the figures from Mahajan (1989), since the spatial behaviour of the density, the magnetic field and the current density are essentially a function of the dimensionless parameter λ.

Coronal loops

Coronal loop, a bipolar structure is characterized by an electron density $n_0 \sim 10^{10}$–10^{12} cm^{-3}; a temperature varying from a few tens of thousands to a couple of million K, a length of 10^9–10^{10} cm and a radius of 10^8–10^9 cm with an axial magnetic fields of a few Gauss. The current flows essentially along the axis of the cylindrical plasma column and produces an azimuthal component B_θ of the magnetic field. Observations in EUV has shown that loops of different temperatures are coaxial and this has led to the identification of cool-core and hot-sheath-type loops, (Foukal 1978; Krishan 1983, 1985). The X-ray observations further reinforce the inhomogeneous nature of the underlying heating mechanisms. Resonance absorption of surface MHD waves, as well as the joule dissipation of high-density current sheets (in addition to the ubiquitous mini magnetic reconnections) are some of the favoured candidates for heating of the solar corona in general, and coronal loops in particular (Hollweg 1981). Here we find that the exact solution of a Vlasov–Maxwell system naturally admits the peaked spatial profiles of current density and magnetic field, and we believe it is this equilibrium configuration, which when disturbed, gives rise to sporadic flaring phenomena, acceleration and heating. It has been shown by Rosner et al. (1978) and Hollweg (1981) that for the joule dissipation to provide enough heating to balance the radiation losses for the typical conditions of electron density, magnetic field and temperature, the current sheath must have a thickness of a few hundred to a thousand cm, and anomalous instead of the collisional resistivity must be operative. The latter gives us a clue to the relative electron–ion drift velocity that must exist to excite ion–acoustic turbulence which may be responsible for anomalous resis-

tivity. The typical parameters in this scenario are chosen from Hollweg (1981):

electron density in the sheath–$n_0 = 10^9$ cm^{-3};
electron temperature in the sheath–$T_e = 2.5 \times 10^7$ K;
electron thermal speed–$V_e = 2.7 \times 10^9$ cm s^{-1};
electron drift velocity $u_e >$ sound speed– $= 4.5 \times 10^7$ cm s^{-1};

The magnetic field B_θ produced by the current density J, is 10 G, and the thickness (ΔR) of the current sheet turns out to be $\sim 10^3$ cm. We recall from the previous section that δ_e is the characteristic length-scale in the solutions of the Vlasov–Maxwell system. Let us estimate it:

$$\delta_e = \frac{c}{\omega_{pe}}\frac{V_e}{u_e}(1 + \sqrt{T_i/T_e})^{-1/2}$$

$$= 1.04 \times 10^3 \text{ cm for } T_e \gg T_i,$$
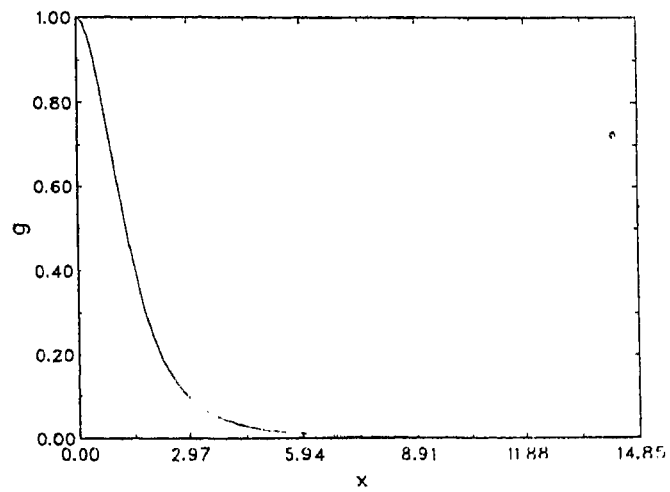$$= 0.9 \times 10^3 \text{ cm for } T_e = 9\ T_i.$$

Figure 1. Variation of density profile function $g(r)$ versus $x = r/\delta_e$ for case I (equation 8).
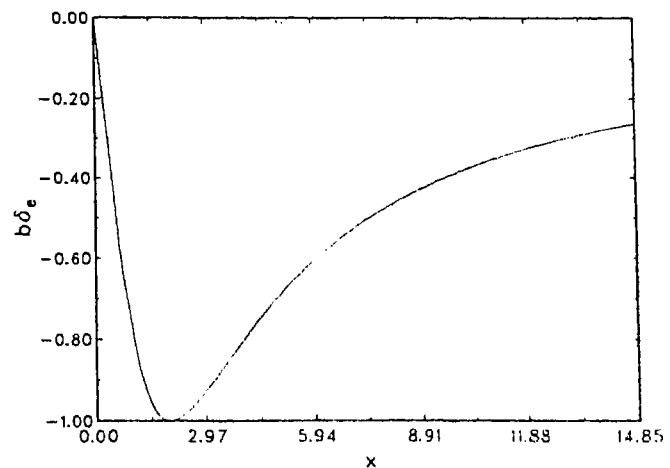

Figure 2. Variation of magnetic-field profile function ($b\ \delta_e$) versus $x = r/\delta_e$ for case I (equation 9).
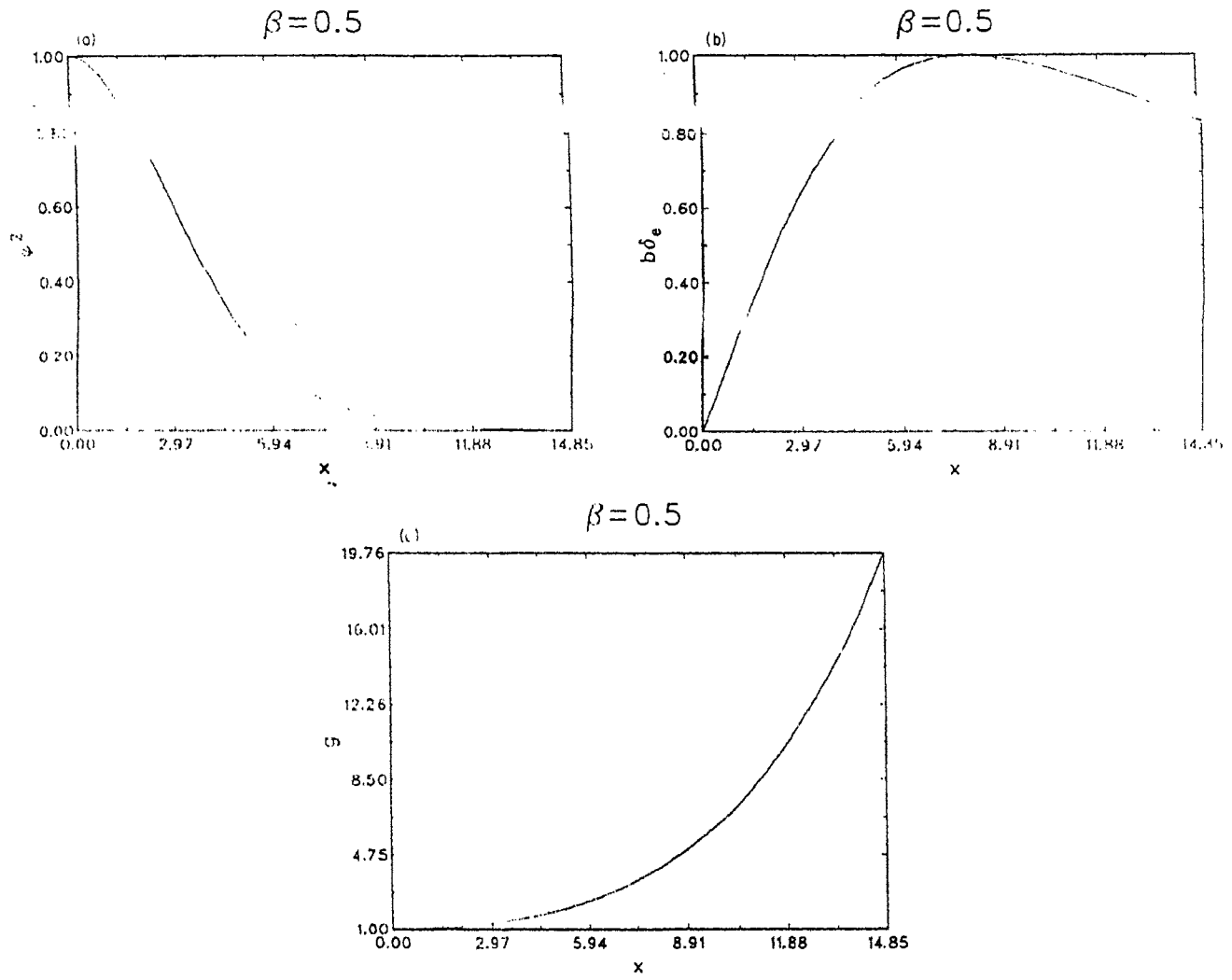
Figure 3. (a) Variation of temperature profile function ψ^2 versus $x = r/\delta_e$ for $\beta = 0.5$ (equation 15). (b) Variation of magnetic-field profile function $(b\delta_e)$ versus $x = r/\delta_e$ for $\beta = 0.5$ (equation 14). (c) Variation of density profile function $g(r)$ versus $x = r/\delta_e$ for $\beta = 0.5$ (equation 13).
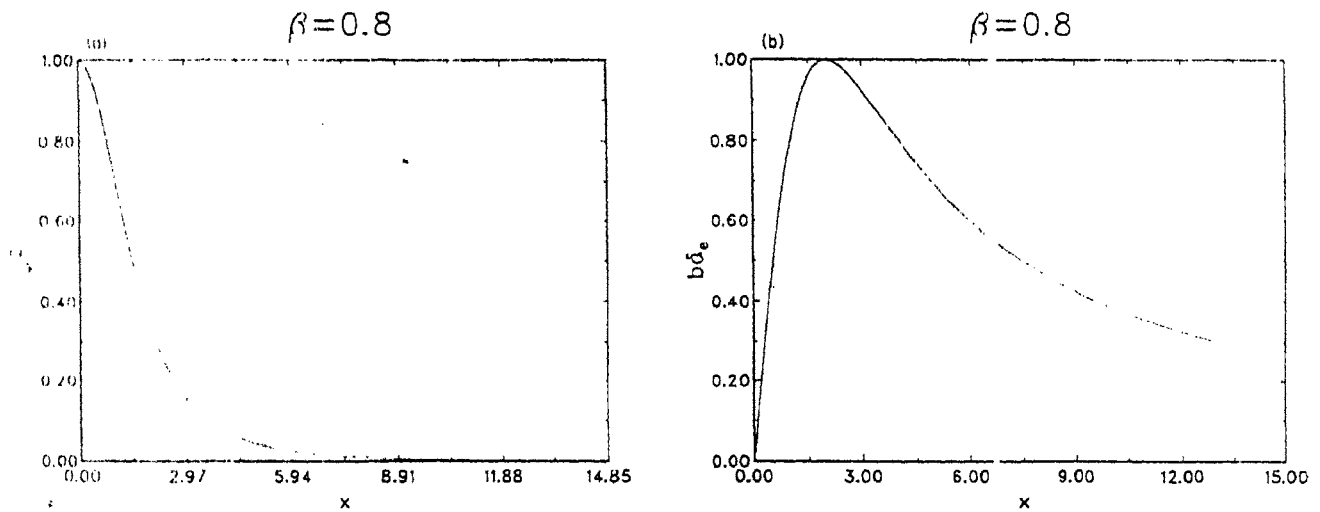

Figure 4. (a) Variation of temperature profile function ψ^2 versus $x = r/\delta_e$ for $\beta = 0.8$. (b) Variation of magnetic-field profile function $(b\delta_e)$ versus $x = r/\delta_e$ for $\beta = 0.8$. (c) Variation of density profile function $g(r)$ versus $x = r/\delta_e$ for $\beta = 0.8$.
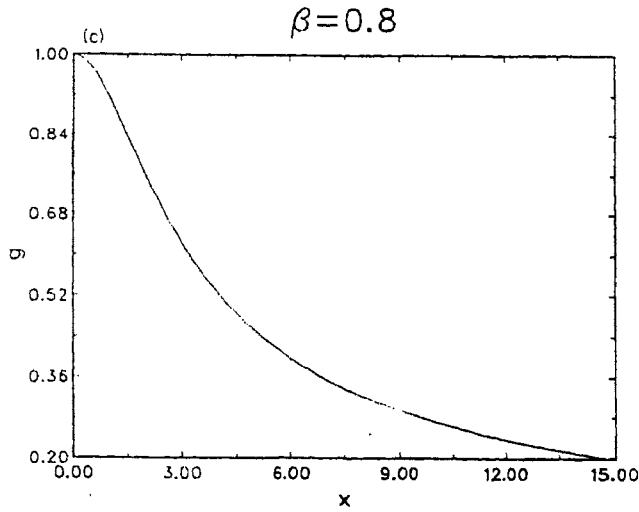
$$\beta = 0.8$$

Figure 4 – *continued*

Thus we find that current profile of small widths are the outcome of the exact solutions of the Vlasov-Maxwell system. Here we present a few examples of spatial variations of plasma parameters. The variations of density and magnetic-field profile factors (g and b, respectively) for case I, where only the density is space dependent, are given by equations (8) and (9) and shown in Figs (1) and (2). A sharp fall in density away from the axis is obtained. This is reminiscent of the condensations often observed at the axis of a loop. The current density is therefore found to be maximum on the axis. The spatial profiles for case II allowing temperature variation are given by equations (12), (13) and (14), and are shown in Figs (3), (4) and (5) for three values of the parameter β. In this case the temperature increase (equation 15) away from the axis for $\beta < 2/5$. Case III gives very interesting profiles where the current density appears in the form of multisheaths (Fig. 6) for large values of the anisotropy parameter; the corresponding density profile (Fig. 7) is almost flat. These profiles are reproduced from Mahajan (1989). Since all functions, as well as the variables, are
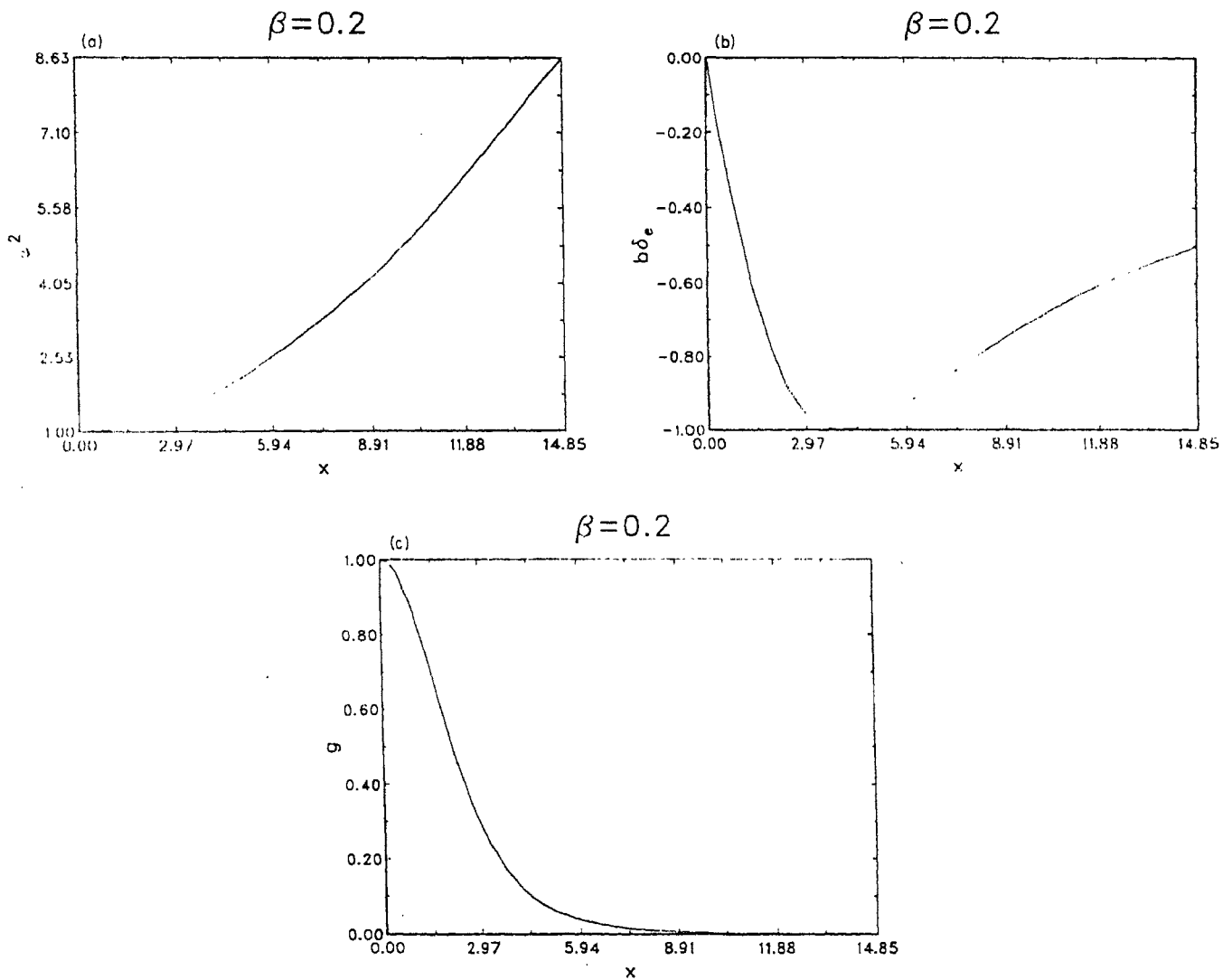

$$\beta = 0.2$$

$$\beta = 0.2$$

$$\beta = 0.2$$

Figure 5. Variation of temperature profile function ψ^2 versus $x = r/\delta_e$ for $\beta = 0.2$. (b) Variation of magnetic-field profile function $(b\delta_e)$ versus $x = r/\delta_e$ for $\beta = 0.2$. (c) Variation of density profile function $g(r)$ versus $x = r/\delta_e$ for $\beta = 0.2$.
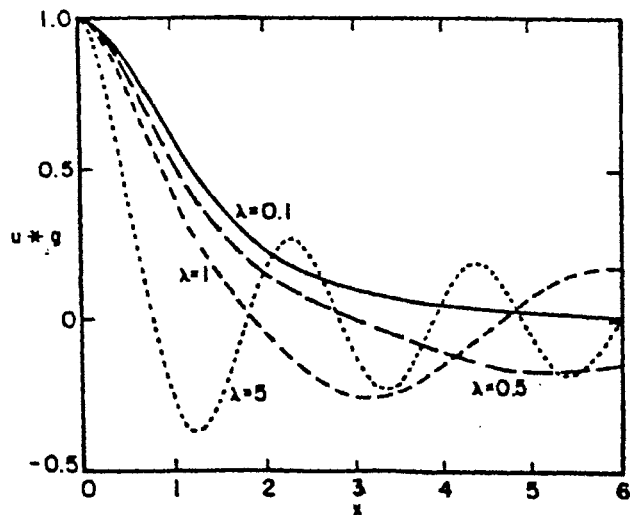
Figure 6. Variation of current profile function (gue) versus $x = r/\delta$, showing formation of multisheaths for large values of temperature anisotropy parameter λ (from Mahajan 1989).

Figure 7. Variation of density profile function $g(r)$ versus $x = r/\delta$, for several values of the temperature anisotropy parameter λ (from Mahajan 1989).

expressed in dimensionless forms, we only need to provide appropriate normalization. For coronal loops, the anisotropy parameter

$$\lambda = \frac{\Delta T_e}{T_e} \frac{V_s^2}{2u_e^2} = 1.8 \times 10^3 \frac{\Delta T_e}{T_e}$$

Thus for $\lambda \approx 5$ one finds $(\Delta T_e/T_e) \approx 2.7 \times 10^{-3}$, which is reasonably small.

CONCLUSIONS

A Vlasov–Maxwell description of coronal loop plasma admits a variety of equilibrium spatial profiles of mass density, current density, the temperature, and the magnetic field depending upon the type of inhomogeneities allowed. The profiles vary from being flat to spiky and resemble the ones derived from EUV and X-ray coronal observations. The multisheath current profiles derived here complement the magnetohydrodynamic study of current sheet formation especially well. In addition, the Vlasov description allows the determination of density and temperature profiles individually, in contrast to the fluid description where equation of state is required to extract the separate variations of density and temperature from the pressure profile.
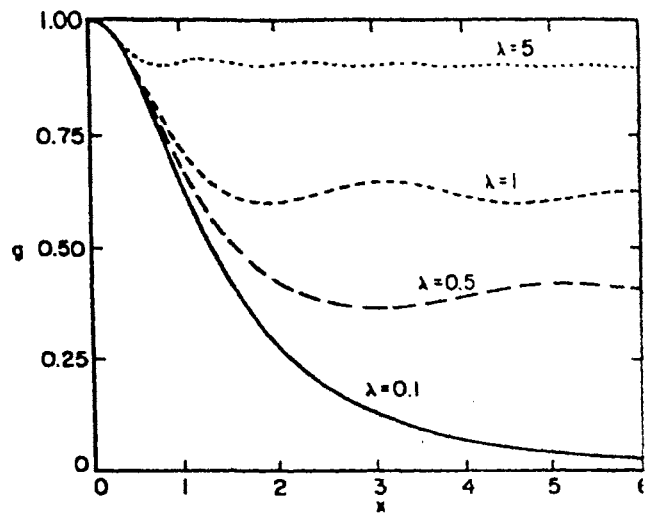
REFERENCES

Foukal, P. V., 1978. *Astrophys. J.* **223**, 1046.
Hollweg, J. V., 1981. In: *Solar Active Regions*, p. 277, ed. Orrall, F. Q., Colorado Associated University Press.
Hood, A. W. & Priest, E. R., 1979. *Astr. Astrophys.*, **77**, 233.
Karpen, J. T., Antiochos, S. K. & De Vove, C. R., 1990. *Astrophys. J.*, **356**, L67.
Krieger, A. S., de Feiter, L. D. & Vaiana, G. S., 1976. *Solar Phys.*, **47**, 117.
Krishan, V., 1983. *Solar Phys.*, **88**, 155.
Krishan, V., 1985. *Solar Phys.*, **97**, 183.
Krishan, V., Berger, M. & Priest, E. R., 1988. In: *Solar and Stellar Coronal Structures and Dynamics*, p. 256, ed. Altrock, R. C., National Solar Observatory, Sunspot, New Mexico.
Low, B. C., 1987. *Astrophys. J.*, **323**, 358.
Low, B. C. & Wolfson, R., 1988. *Astrophys. J.*, **324**, 574.
Mahajan, S. M., 1989. *Phys. Fluids B1*, **1**, 43.
Parker, E. N., 1983. *Astrophys. J.*, **264**, 635.
Parker, E. N., 1987. *Astrophys. J.*, **318**, 876.
Priest, E. R., 1981. In: *Solar Flare Magnetohydrodynamics*, p. 2 and 139, ed. Priest, E. R., Gordon and Breach.
Rosner, R., Golub, L., Coppi, B. & Vaiana, G. S., 1978. *Astrophys. J.*, **222**, 317.
Tsinganos, K. C., 1982. *Astrophys. J.*, **259**, 820.
Vaina, G. S. & Rosner, R., 1978. *Ann. Rev. Astr. Astrophys.*, **16**, 393.
Van Ballegooijen, A. A., 1985. *Astrophys. J.*, **298**, 421.
Van Ballegooijen, A. A., 1986. *Astrophys. J.*, **311**, 1001.

PRESSURE STRUCTURE OF SOLAR CORONAL LOOPS, III

T. D. SREEDHARAN*, K. SASIDHARAN, A. SATYA NARAYANAN,
and V. KRISHAN

Indian Institute of Astrophysics, Bangalore 560 034, India

Abstract. The theory of ideal magnetohydrodynamic turbulence in cylindrical geometry is used to study the steady-state structure of a coronal loop. The pressure profile is derived from MHD equations by representing the velocity and magnetic fields as the superposition of Chandrasekhar–Kendall functions. Such a representation brings out the three-dimensional structure of the pressure in the coronal loop. The radial, azimuthal, and axial variations of the pressure for a constant density loop are discussed in detail. The pressure has an oscillatory behavior for different azimuthal angles at some radial positions. This study predicts more features in pressure than can be compared with the presently available observations.

1. Introduction

It is well known that the solar corona is highly structured. The basic structural component of the solar corona is the coronal loop. These loops or arch-like structures of the active regions of the Sun have been observed in the emission at the UV, FUV, and X-ray wavelengths (Foukal, 1978; Levine and Withbroe, 1977; Vaiana and Rosner, 1978) The theory of radio pulsations in coronal loops has been discussed by Aschwanden (1987).

Coronal loop plasma is believed to carry currents which result in a helical form of the magnetic field (Levine and Altschuler, 1974; Poletto *et al.*, 1975; Krieger, de Feiter, and Vaiana, 1976; Priest, 1978, Hood and Priest, 1979). The MHD equilibria of coronal loops have been investigated by Priest (1981) and Tsinganos (1982).

In spite of the continuous pumping of magnetic and velocity field fluctuations into the coronal plasma, the loops exhibit a fairly stable and well configured geometry. The steady-state pressure structure is the result of the various manifestations of the balance of the inertial and magnetic forces. Krishan (1983a, b) discussed a steady-state model of active region coronal loops using the statistical theory of incompressible magneto-hydrodynamic turbulence described by Montgomery, Turner, and Vahala (1978). The main features of the theory consists of using the MHD equations for an incompressible fluid. The magnetic and velocity fields are expanded in terms of Chandrasekhar–Kendall (hereafter referred to as C–K) functions for which, the completeness has been proved by Yoshida and Giga (1990). The pressure profile is derived as a function of the velocity and magnetic fields in the form of Poisson equation. The spatial profiles of lines in active region loops were also studied. The statistical mechanics of velocity and magnetic fields in solar active regions was discussed by Krishan (1985). Krishan, Berger, and Priest

---

* Permanent address: Department of Physics, Mount Carmel College Bangalore, 560 052, India.

(1988) discussed the dynamics of velocity and magnetic fields in coronal loops. Recently Krishan, Sreedharan, and Mahajan (1991) have also presented a Vlasov–Maxwell description of coronal loops which is a preparation for the study of kinetic processes related to heating and acceleration of plasma particles.

The force-free magnetic fields ($\overline{\nabla} \times \overline{B} = \alpha\overline{B}$) and the Beltrami flows ($\overline{\nabla} \times \overline{V} = \alpha\overline{V}$) represent the minimum energy state of a magnetofluid. A single C–K function represents these configurations of the magnetic and velocity fields. The magnetofluid in the coronal loop is believed to be in an approximate state of the force-free fields with small departures from the current-free fields of the photospheric fluid. Now, it is quite reasonable to expect the coronal loop fields and flows to have departures from the strictly force-free configuration. By representing the fields by the superposition of the C–K functions we can manoeuvre these departures in a systematic and quantitative manner.

We extend the earlier work on the steady-state structure of the pressure in coronal loops, by representing the velocity and magnetic fields as the superposition of three Chandrasekar–Kendall functions. This brings in the three-dimensional spatial variation (r, θ, z) in the plasma pressure and the state is not force-free, although individually the C–K functions represent a force-free state. The motivation behind the choice of three (C–K) functions for velocity and magnetic fields is to extend this study to include the time-dependence of pressure in coronal loops. The three-mode representation admits the temporal behavioral of the fields in its most basic form. Besides a three-mode representation also in principle exhibits chaotic behavior. The evolution of the resistive magnetohydrodynamic equillibria is being studied in order to understand the emergence of preferred structures, if any, by Shan, Montgomery, and Chen (1991). A truncated three-mode configuration has been explored by Chen, Shan, and Montgomery (1990) and their results qualitatively agree with the predictions of the minimum dissipation theory (Montgomery, Phillips, and Theobald, 1989) as well as with the computations obtained using the numerical code (Dahlburg et al., 1986, 1987, 1988 and Theobald et al., 1989). We however plan to study the three-mode ideal system in order to qualify the variations of the velocity and magnetic fields in the solar atmosphere, in terms of nonlinear or stochastic fluctuations. In this paper we discuss only the three-dimensional spatial pressure structure of coronal loops.

In the next section, we present the MHD equations for an incompressible fluid and outline the pressure profile. Section 3 deals with a discussion of the results obtained in this study.

2. Derivation of the Pressure Profile

The coronal loop plasma is represented by a cylindrical column of length 'L' and radius 'R'. The mechanical pressure P is expressed as a function of velocity $\overline{V}$ and magnetic field $\overline{B}$ using the MHD equations

$$\frac{\overline{\nabla} P}{\rho} = \frac{(\overline{\nabla} \times \overline{B}) \times \overline{B}}{\rho} - (\overline{V} \cdot \overline{\nabla})\overline{V} - \frac{\partial \overline{V}}{\partial t} , \tag{1a}$$

$$V \times (\bar{V} \times B) - \frac{\partial B}{\partial t} = 0, \quad \text{See page 7 Cowling} \tag{1b}$$

where ρ is the mass density and the force due to gravity has been neglected.

Using the identity $(\bar{V} \cdot \bar{\nabla})\bar{V} = (\bar{\nabla} \times \bar{V}) \times \bar{V} + (1/2)\bar{\nabla}V^2$, Equation (1a) becomes

$$\nabla[P/\rho + (1/2)V^2] = \left[\frac{(\bar{\nabla} \times \bar{B}) \times \bar{B}}{\rho} - (\bar{\nabla} \times \bar{V}) \times \bar{V}\right] - \frac{\partial \bar{V}}{\partial t}. \tag{2}$$

Following Montgomery, Turner, and Vahala (1978), the velocity field V and magnetic field B in the loop plasma are represented by the superposition of Chandrasekhar–Kendall functions. The complete dynamics can be described by a set of infinite coupled nonlinear ordinary differential equations which are of first order in time for the expansion coefficients of velocity and magnetic fields and it is a formidable task to find solutions to these equations. Hence, here we choose to represent the fields by the superposition of the three lowest order C–K functions. Another justification for doing so is that these functions represent the largest spatial scales and therefore may be the most suitable states for comparison with observed phenomena.
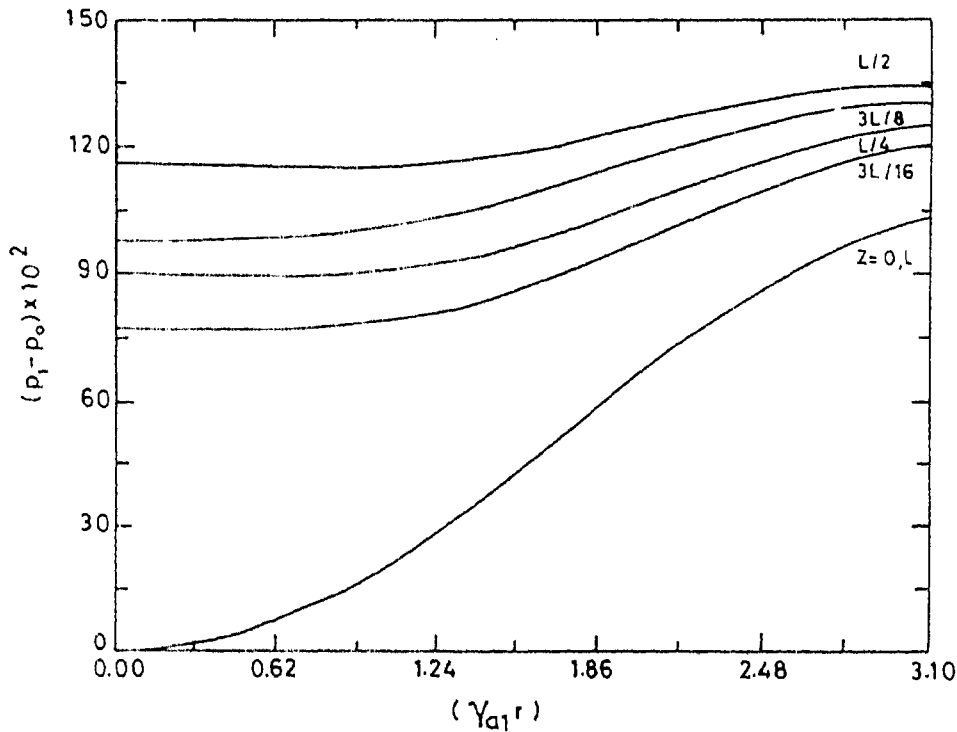

Fig. 1. Radial variation of the pressure P_i for different axial distances, Z.

In the triple-mode system,

$$\overline{V} = \lambda_a \eta_a(t)\overline{A}_a + \lambda_b \eta_b(t)\overline{A}_b + \lambda_c \eta_c(t)\overline{A}_c , \tag{3}$$

$$\overline{B} = \lambda_a \xi_a(t)\overline{A}_a + \lambda_b \xi_b(t)\overline{A}_b + \lambda_c \xi_c(t)\overline{A}_c , \tag{4}$$

$$\bar{a}_{nm}(r) = \hat{e}_r\left[\frac{im}{r} + \frac{ik_n}{\lambda_{nm}}\frac{\partial}{\partial r}\right]\psi_{nm} + \hat{e}_\theta\left[-\frac{\partial}{\partial r} - \frac{mk_n}{r\lambda_{nm}}\right]\psi_{nm} +$$

$$+ \hat{e}_z\left[\frac{\lambda_{nm}^2 - k_n^2}{\lambda_{nm}}\right]\psi_{nm} , \tag{5}$$

where

$$\psi_{nm} = J_m(\gamma_{nm}r)\exp\,(im\theta + i\,k_n z),$$

$$\lambda_{nm} = \mp\,(\gamma_{nm}^2 + k_n^2)^{1/2}, \qquad k_n = 2\pi n/L, \qquad \begin{array}{l} n = 0, \mp 1, \mp 2, \ldots, \\ m = 0, \mp 1, \mp 2, \ldots, \end{array}$$

$$\overline{A}_{nm} = C_{nm}\bar{a}_{nm}(r) ;$$

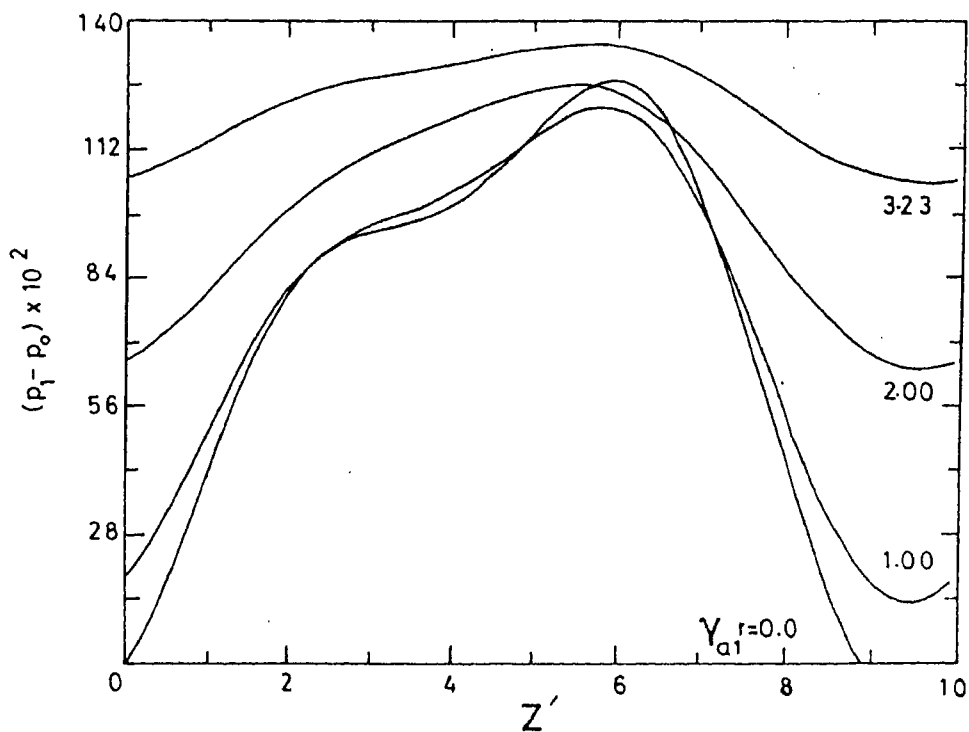η's and ξ's are in general complex.

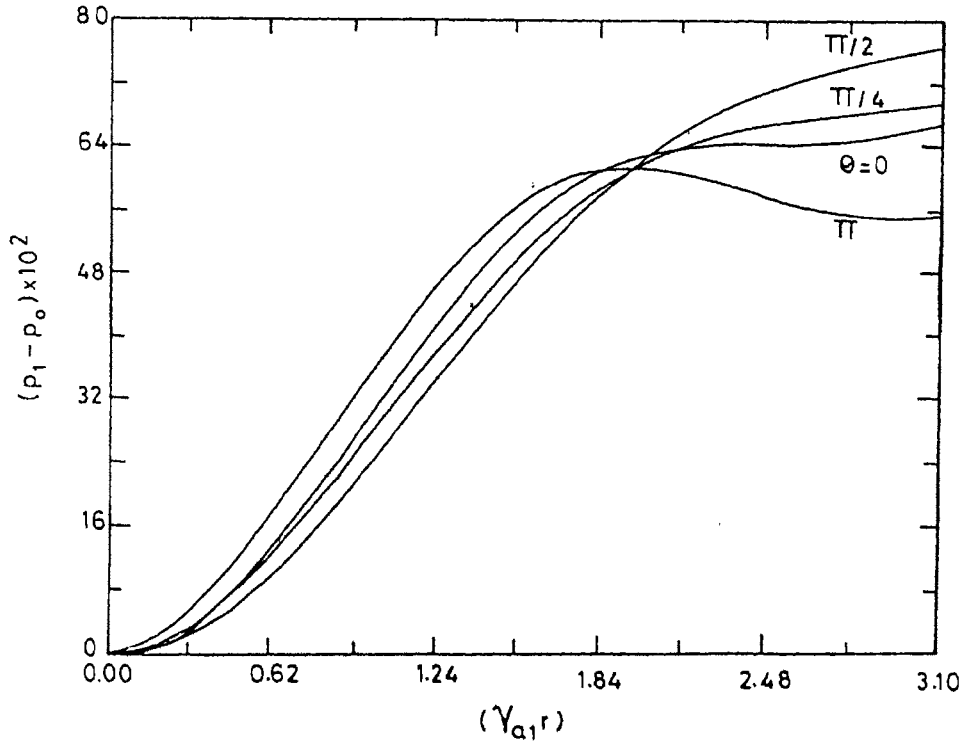Fig. 2. Axial variation of the pressure P_1 for different radial distances, r.

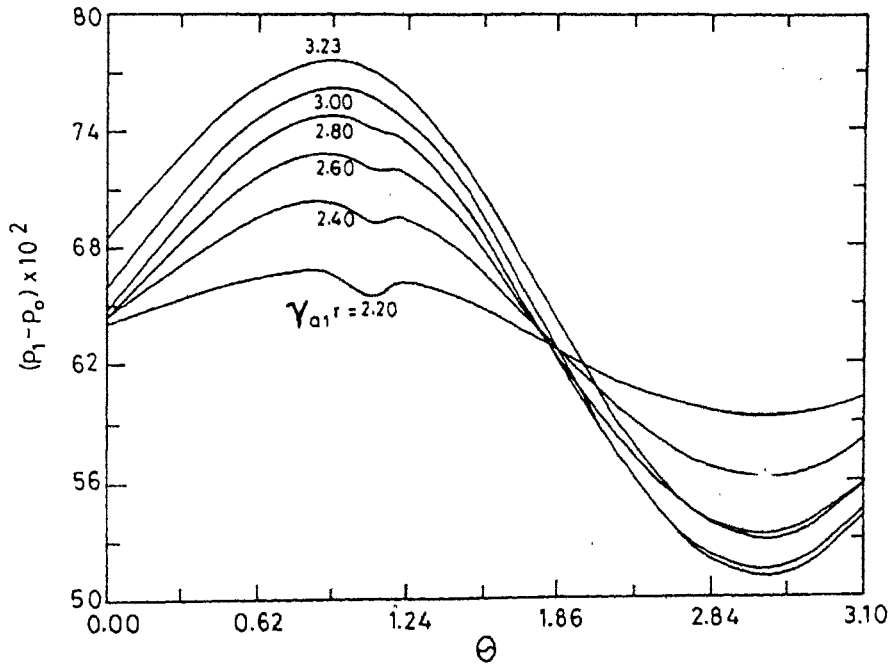Fig. 3. Radial variation of the pressure P_1 for different azimuthal angles, θ.

Fig. 4. Azimuthal variation of the pressure P_1 for $\gamma_{a1}r = 2.2$ to 3.23.

The functions a_{nm} satisfy $\nabla \times a_{nm} = \lambda_{nm} a_{nm}$. γ_{nm} can be determined from the boundary conditions for a perfectly conducting and rigid boundary since the observations do show very well-defined loop structures aligned with the magnetic field across which there is little or no transport. Thus the radial component of the velocity and the magnetic field vanish at the surface $r = R$, i.e.,

$$R\, k_n \gamma_{nm} J'_m(\gamma_{nm}R) + m\lambda_{nm} J_m(\gamma_{nm}R) = 0 \ . \tag{6}$$

However, for the $(n = 0 = m)$ mode, $V_r = B_r = 0$, and the γ_{00} is determined from the constancy of the ratio of the toroidal and poloidal magnetic fluxes as

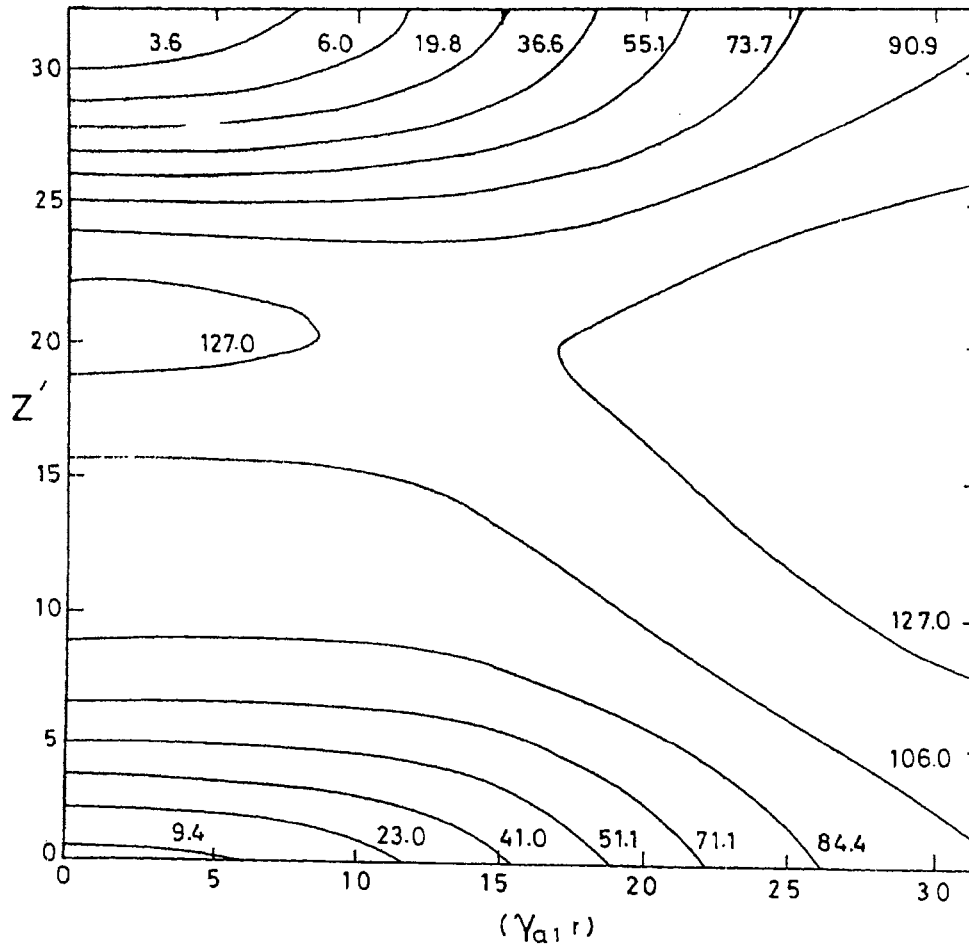$$\frac{\psi_t}{\psi_p} = -\frac{J'_0(\gamma_{00}R)\, R\, \gamma_{00}}{J_0(\gamma_{00}R)\, L\, \lambda_{00}} \ ; \tag{7}$$

Fig. 5. Contour plot of the pressure P_1 as a function of $\gamma_{a1} r$ and Z' when θ is averaged. Each unit of the axes corresponds to $\gamma_{a1} r = 0.1$ and $Z' = 0.3$, respectively.

C_{nm} is the normalizing constant which relates $\overline{A}_{nm}$ to $\overline{a}_{nm}$ by

$$A_{nm} = C_{nm}\overline{a}_{nm} \quad \text{and} \quad \int \overline{A}^*_{n'm'} \cdot \overline{A}_{nm} \, d^3r = \delta_{nn'} \delta_{mm'} \ .$$

The dynamics can be described by taking the inner products of the curl of Equations (1a) and (1b) with A^*_{nm} and integrating over the volume. The resulting six complex, coupled nonlinear ordinary differential equations are

$$\frac{\partial \eta_a}{\partial t} = \frac{\lambda_b \lambda_c}{\lambda_a} (\lambda_c - \lambda_b) I [\eta_b \eta_c - \xi_b \xi_c / \rho] \ , \tag{8}$$

$$\frac{\partial \eta_b}{\partial t} = \frac{\lambda_c \lambda_a}{\lambda_b} (\lambda_a - \lambda_c) I^* [\eta_c^* \eta_a - \xi_c^* \xi_a / \rho] \ , \tag{9}$$

$$\frac{\partial \eta_c}{\partial t} = \frac{\lambda_a \lambda_b}{\lambda_c} (\lambda_b - \lambda_a) I^* [\eta_a \eta_b^* - \xi_b^* \xi_a / \rho] \ , \tag{10}$$
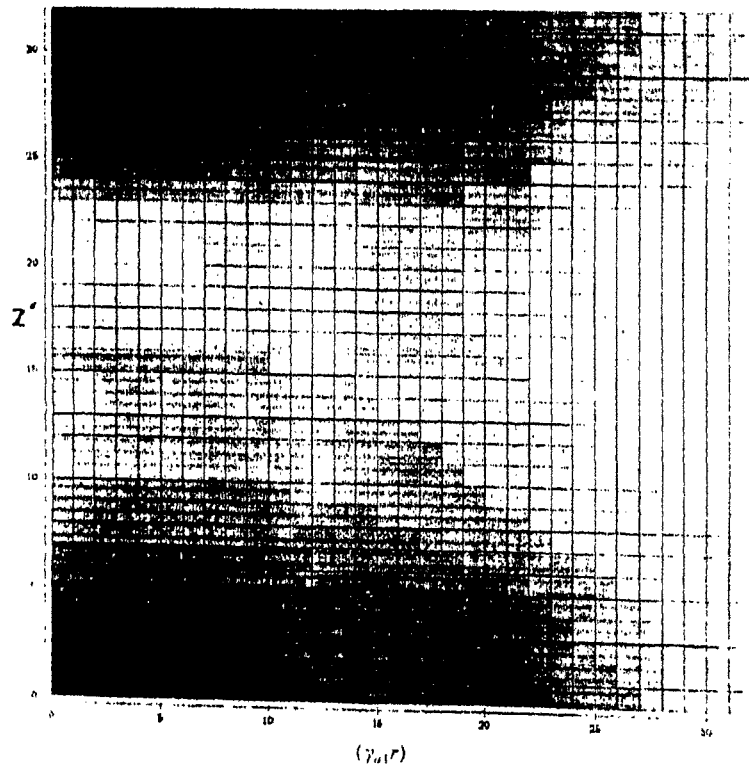

Fig. 6a. Density plot of the pressure P_1 as a function of $\gamma_{a1} r$ and Z'.
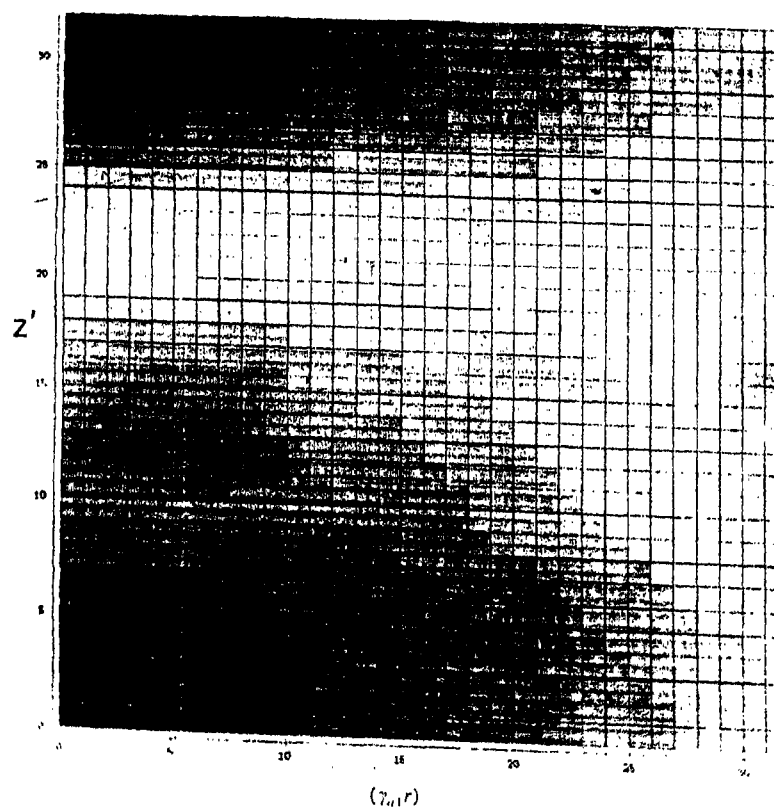
Fig. 6b.   Same as in Figure 6(a) for $\eta_{b1} > \eta_{c1}$.

$$\frac{\partial \xi_a}{\partial t} = \lambda_b \lambda_c I \left[\eta_b \xi_c - \eta_c \xi_b \right],$$ (11)

$$\frac{\partial \xi_b}{\partial t} = \lambda_c \lambda_a I^* \left[\eta_c^* \xi_a - \eta_a \xi_c^* \right],$$ (12)

$$\frac{\partial \xi_c}{\partial t} = \lambda_a \lambda_b I^* \left[\eta_a \xi_b^* - \eta_b^* \xi_a \right],$$ (13)

where $I = \int A_a^* \cdot (A_b \times A_c) \, d^3r$ and the (n, m) values of the modes (a, b, c) satisfy the conditions $n_a = n_b + n_c$ and $m_a = m_b + m_c$.
It can be shown that

$$(\nabla \times B) \times B = \sum_{\substack{i=a,b,c \\ l=b,c,a}} \lambda_i \lambda_l \xi_i \xi_l (\lambda_i - \lambda_l) A_i \times A_l,$$ (14)

$$(\nabla \times V) \times V = \sum_{\substack{i \ a, b, c \\ j \ b, c, a}} \lambda_i \lambda_j \eta_i \eta_j (\lambda_i - \lambda_j) \vec{A}_i \times \vec{A}_j , \tag{15}$$

so that

$$\nabla(P/\rho + (1/2)V^2) = \sum_{\substack{i \ a, b, c \\ j \ b, c, a}} \lambda_i \lambda_j (\lambda_i - \lambda_j) \left(\frac{\xi_i \xi_j}{\rho} - \eta_i \eta_j \right) \vec{A}_i \times A_j - \frac{\partial V}{\partial t} . \tag{16}$$

In this paper we confine our study to the steady-state solution to the pressure. For the steady-state $\partial/\partial t \ [\eta, \xi] = 0$, and hence, we find from Equations (8) to (13)

$$\eta_a = \xi_a/\rho^{1/2}, \quad \eta_b = \xi_b/\rho^{1/2} \quad \text{and} \quad \eta_c = \xi_c/\rho^{1/2} .$$

Equation (16) reduces to

$$\nabla(P/\rho + (1/2)V^2) = 0 .$$

i.e., $P/\rho + \tfrac{1}{2}V^2 =$ constant.

If the value of P at the origin $(r = 0, z = 0)$ is P_0, then

$$P/\rho = P_0/\rho + (1/2)V_0^2 - (1/2)V^2 , \tag{17}$$

where V_0 is the velocity at the origin $(r = 0, z = 0)$.

3. Discussion

The spatial variation of pressure is presented for a cylindrical column of plasma for which the ratio of the radius R to length L has been taken to be $R/L = \tfrac{1}{10}$ and the ratio of the toroidal to poloidal flux $\psi_t/\psi_p = 0.1$.

We have chosen two triads a, b, c such that they represent the largest possible spatial scales, as well as satisfy the condition $a = b + c$. These are:

$$a_1 = (1, 1), \quad b_1 = (1, 0), \quad \text{and} \quad c_1 = (0, 1);$$
$$a_2 = (0, 0), \quad b_2 = (1, 1), \quad \text{and} \quad c_2 = (-1, -1).$$

The corresponding values of γ's and λ's are found to be (from Equations (6) and (7))

$$\gamma_{a1}R = 3.23, \quad \gamma_{b1}R = 3.85, \quad \gamma_{c1}R = 3.85 ,$$
$$\lambda_{a1}R = 3.29, \quad \lambda_{b1}R = 3.90, \quad \lambda_{c1}R = 3.85 ,$$

and

$$\gamma_{a2}R = 1.44, \quad \gamma_{b2}R = 3.23, \quad \gamma_{c2}R = 3.23 ,$$
$$\lambda_{a2}R = 1.44, \quad \lambda_{b2}R = 3.29, \quad \lambda_{c2}R = 3.29 .$$

The total energy E of the loop plasma in a given configuration (a, b, c) is given by $E = 2 \sum_{i \ a, b, c} \lambda_i^2 \eta_i^2$. Though we have some estimate of the total energy of a typical loop there is no obvious way of fixing the relative magnitudes of the three modes. However, there are two physical considerations we can use to fix the relative strengths of the three modes, as is usually done whenever three mode interactions are involved.
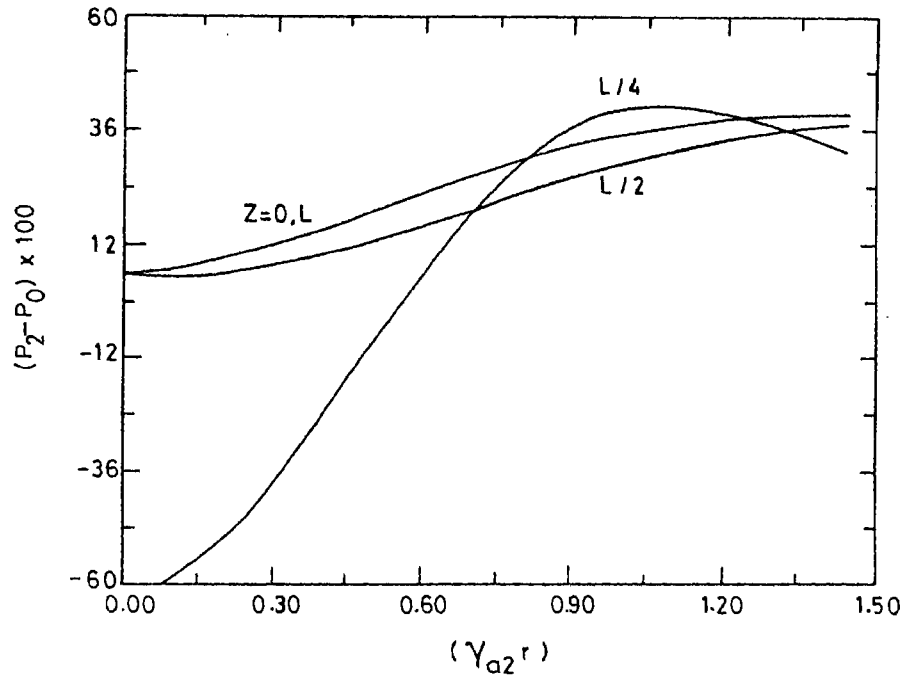
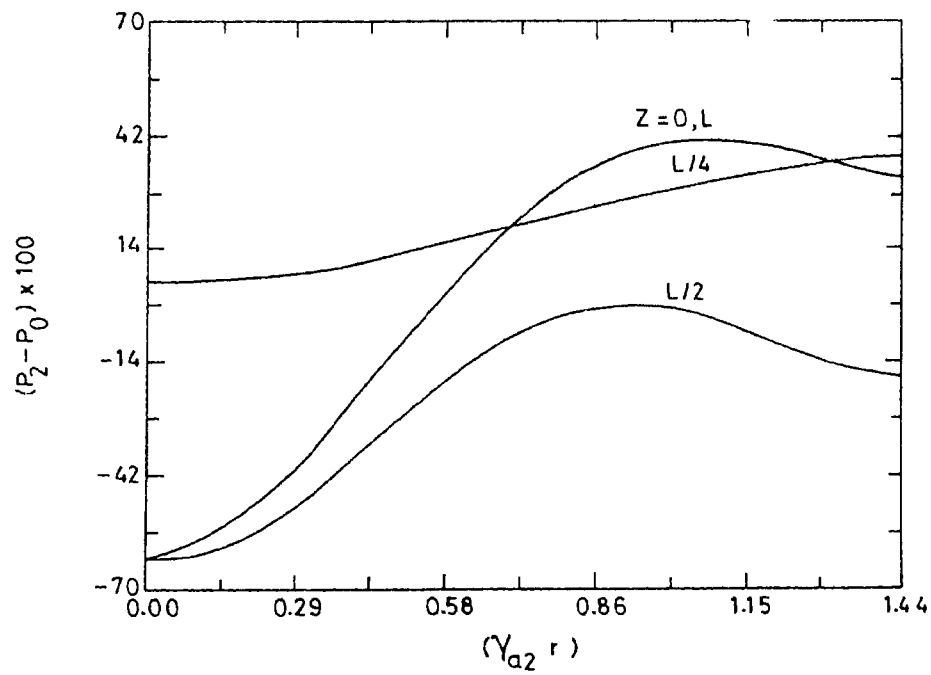Fig. 7a.   Radial variation of the pressure P_2 for $\theta = \pi/4$ and different axial distances.

Fig. 7b.   Radial variation of the pressure P_2 for $\theta = 3\pi/4$ and different axial distances.

3.1. CASE I

The first is the pump approximation under which one of the three modes is taken to be the strongest. For example, here since the conservation conditions give a = b + c, we can take 'a' to be the dominant mode and call it the pump which shares its energy with the other two modes. This will become evident in the time-dependent description. Therefore, let

$$\lambda_a^2 \eta_a^2 > \lambda_b^2 \eta_b^2 \quad \text{and} \quad \lambda_a^2 \eta_a^2 > \lambda_c^2 \eta_c^2 . \quad \text{(18)}$$

3.1.1. *Pressure* (P_1) *Structure in the Configuration* (a_1, b_1, c_1)

For the triad (a_1, b_1, c_1)

$$\eta_{b1}/\eta_{a1} < \lambda_{a1}/\lambda_{b1} \quad 0.8435 \quad \text{and} \quad \eta_{c1}/\eta_{a1} < \lambda_{a1}/\lambda_{c1} = 0.8658.$$

We choose

$$|\eta_{a1}| = 10^7, \qquad |\eta_{b1}| = 8 \times 10^6 = |\eta_{c1}|,$$

so that the pump approximation is valid. The expression on the right-hand side of Equation (17) has been averaged over a full cycle of θ and pressure $(P_1 - P_0)$ is plotted as a function of $\gamma_{a1}r$ for different values of z' ($z' = (z/L) \times 10$) in Figure 1. It can be seen that the pressure (or temperature) at any height increases along the radius towards the surface. The radial variation of pressure is the maximum at the foot points of the loop and it is minimum at the apex. This is in confirmation with the result of Levine and Withbroe (1977) who showed that the coronal loops undergoing dynamic changes are
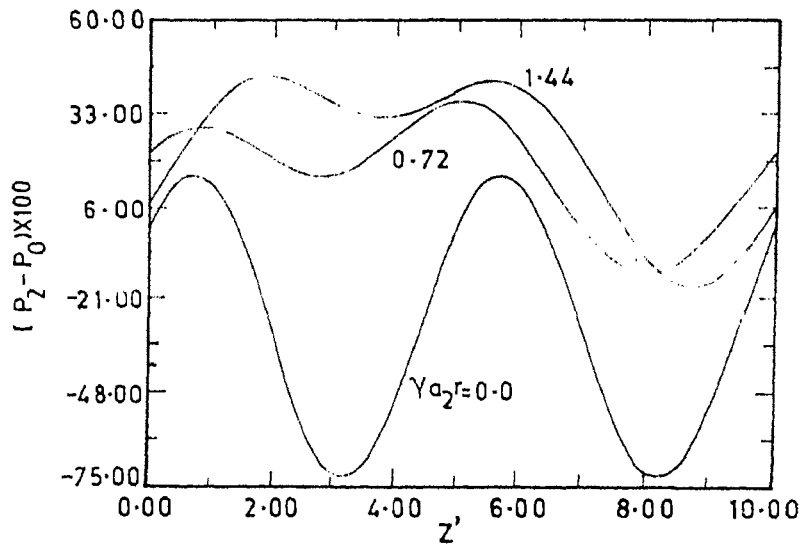

Fig. 8. Axial variation of the pressure P_2 for $\theta = \pi/4$ and different radial distances.

characterized by a temperature structure in which there is a cool core relative to the substantially hot surrounding sheath.

In Figure 2, $(P_1 - P_0)$ is plotted against z' for various values of $(\gamma_{a1}r)$. The axial variation of the pressure is maximum at the axis and minimum at the surface. The maximum value of the pressure is attained near the apex for all values of $(\gamma_{a1}r)$. This is in agreement with the results of Rosner, Tucker, and Vaiana (1978).

Figure 3 presents the radial variation of the pressure for $\theta = 0$, $\pi/4$, $\pi/2$, and π when the pressure is averaged over z. The pressure increases uniformly for all values of $\gamma_{a1}r \leq 2.0$. However, for $\gamma_{a1}r > 2$ the dependence of the pressure on the azimuthal angle is significant.

Figure 4 shows the azimuthal variation of the pressure for different values of $\gamma_{a1}r > 2.0$. The pressure exhibits an oscillatory behavior predominantly near the surface.

Figure 5 depicts the contour plot of pressure as functions of $\gamma_{a1}r$ and z' when the pressure is averaged over θ.

Figure 6(a) is the density plot of the pressure. The darkest region corresponds to the minimum pressure. As we proceed towards the apex, the shades become lighter and the region of maximum pressure is reached. Figure 6(b) is the density plot of the pressure when $\eta_{b1} > \eta_{c1}$. It is seen that the region of the maximum pressure has moved up. However, when $\eta_{c1} > \eta_{b1}$, the region of the maximum pressure has shifted down. Thus the region of maximum pressure need not necessarily be at the apex.
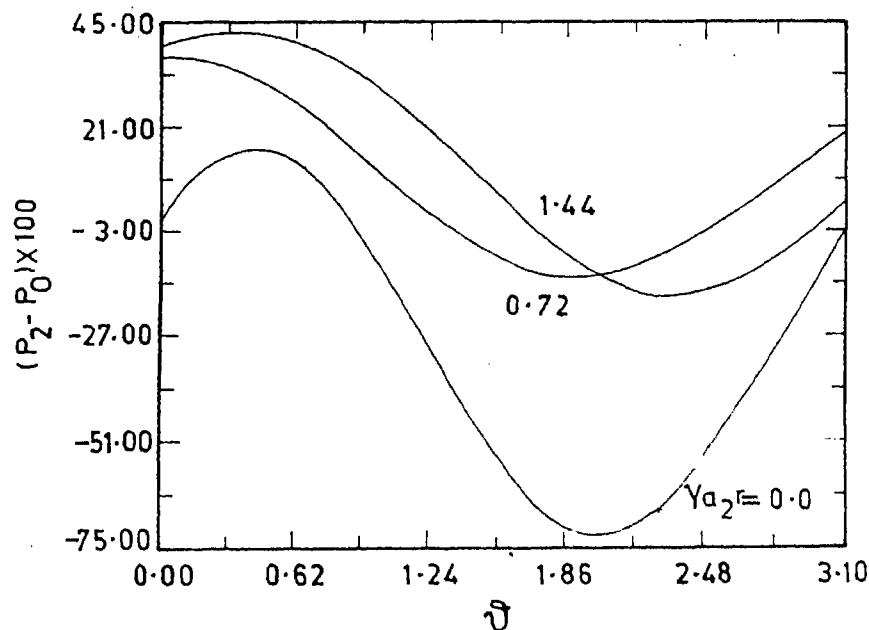

Fig. 9.   Azimuthal variation of the pressure P, for $Z = L/2$ and different radial distances.

3.1.2. Pressure (P_2) Structure in the Configuration (a_2, b_2, c_2)

For the triad $a_2 \equiv (0, 0)$, $b_2 \equiv (1, 1)$, $c_2 \equiv (-1, -1)$, using the inequality (18) and the values $|\eta_{a2}| = 2 \times 10^7$, $|\eta_{b2}| = 8 \times 10^6 = |\eta_{c2}|$, we arrive at the following results:

Figure 7(a) presents the radial variation of the pressure for $\theta = \pi/4$ and for different axial positions. In this case the maximum pressure as well as the maximum variation in pressure is found at $z = L/4$.

Figure 7(b) shows the radial variation of pressure for $\theta = 3\pi/4$ and for $z = 0, L/4, L/2$, and L. Here, the maximum pressure as well as the maximum variation in pressure is at the foot points, in contrast to the case for $\theta = \pi/4$.

The axial variation of pressure for $\theta = \pi/4$ and $\gamma_{a2}r = 0$, 0.72, and 1.44 is given in Figure (8). The pressure shows an oscillatory behavior at the axis of the loop more predominantly than towards the surface.

Figure 9 depicts the azimuthal variation of the pressure at the apex of the loop for different radial distance from the axis. In this case also the oscillatory nature of pressure is evident. The maximum value is attained at the boundary.

3.2. CASE II

3.2.1. Pressure (P_1) Structure in the Configuration (a_1, b_1, c_1)

The second physical consideration that can guide us is that the mode strengths vary in proportion to their spatial scales. The mode with the largest spatial scale may be the
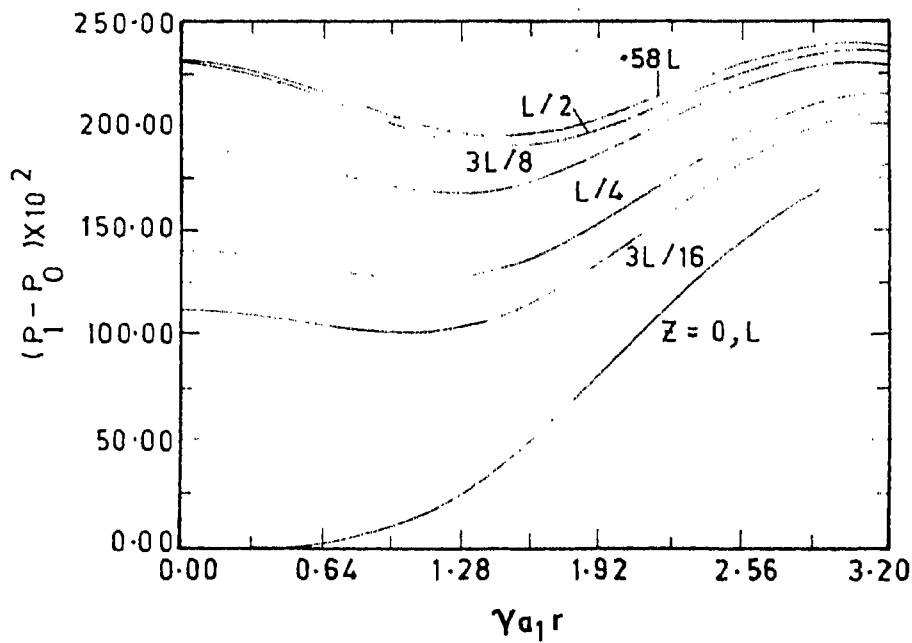

Fig. 10.   Same as in Figure 1 for $\eta_{c1} > \eta_{a1}$.
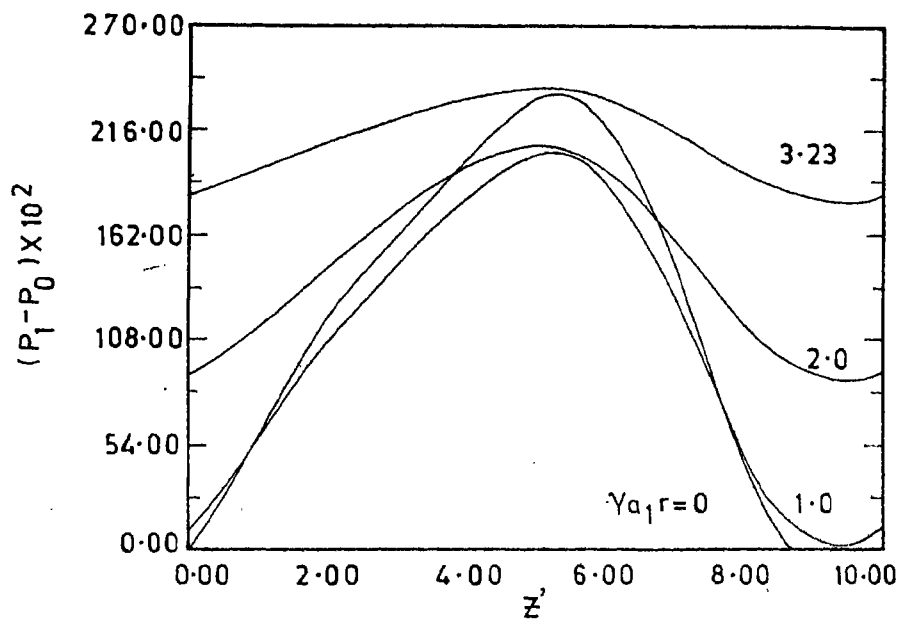
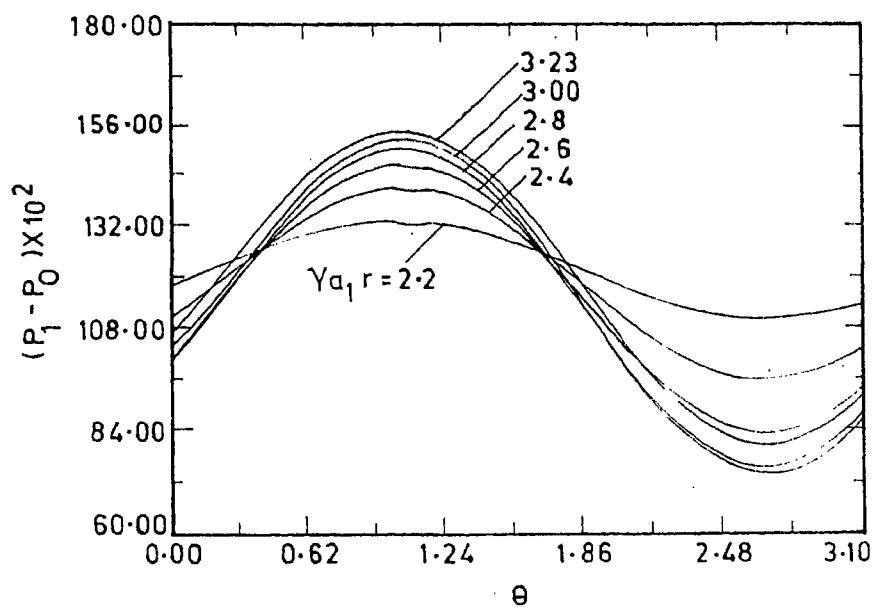Fig. 11.   Same as in Figure 2 for $\eta_{c1} > \eta_{a1}$.

Fig. 12.   Same as in Figure 4 for $\eta_{c1} > \eta_{a1}$.

strongest. Here since $a_1 \equiv (1, 1)$ and $b_1 \equiv (1, 0)$ have the same spatial scale in the z'-direction and this spatial scale is smaller than that of the mode $c_1 \equiv (0, 1)$, we can assume 'a_1' and 'b_1' to be of equal strength and less than the strength of 'c_1', i.e.,

$$\lambda_{a1}^2 \eta_{a1}^2 = \lambda_{b1}^2 \eta_{b1}^2, \quad \lambda_{a1}^2 \eta_{a1}^2 < \lambda_{c1}^2 \eta_{c1}^2;$$

we chose $|\eta_{a1}| = 10^7$, $|\eta_{b1}| = 8.4 \times 10^6$, and $|\eta_{c1}| = 1.6 \times 10^7$ so that the above conditions are satisfied. The radial pressure variation is presented in Figure 10 for different axial positions. The maximum variation of the pressure is at the foot points as in Figure 1. However, for other values of Z', the pressure tends to decrease initially and then increases monotonically after a certain radial distance, contrary to the pressure profile given in Figure 1, where one sees a monotonically increasing pressure for all values of Z'.

The axial and azimuthal variations of the pressure are given in Figures 11 and 12, respectively. The trend is very similar to that presented in Figures 2 and 3.

3.2.2. *Pressure (P_2) Structure in the Configuration (a_2, b_2, c_2)*

In this case the mode $a_2 \equiv (0, 0)$ corresponds to the largest spatial scale and therefore if this is stronger than the other two we arrive at the conditions $\lambda_{a2}^2 \eta_{a2}^2 > \lambda_{b2}^2 \eta_{b2}^2$ and $\lambda_{a2}^2 \eta_{a2}^2 > \lambda_{c2}^2 \eta_{c2}^2$ which are identical to the pump case for the triad (a_2, b_2, c_2) and the pressure profiles have already been discussed.

3.3 CONCLUSION

In conclusion, the representation of velocity and magnetic fields by a three-mode Chandrasekhar–Kendall functions brings out the three-dimensional features of the pressure profile. We believe that the choice of the triads representing the variations of velocity and magnetic fields on the largest spatial scales permitted by the system, provides a fairly realistic description of the loop plasma. Though the pressure structure is a strong function of the relative amplitudes of the modes, the trends, like an increase of pressure towards the surface and the existence of maximum somewhere along the length of the loop, emerge as the general features. The temporal evolution of the pressure is being considered and will be reported shortly.

References

Aschwanden, M. J.: 1987, *Solar Phys.*, **111**, 113.
Chen, H., Shan, X., and Montgomery, D.: 1990, *Phys. Rev.* **A42**, 6158.
Dahlburg, J. P., Montgomery, D., Doolen, G. D., and Turner, L.: 1986, *Phys. Rev. Letters* **57**, 428.
Dahlburg, J. P., Montgomery, D., Doolen, G. D., and Turner, L.: 1987, *J. Plasma Phys.* **37**, 299.
Dahlburg, J. P., Montgomery, D., Doolen, G. D., and Turner, L.: 1988, *J. Plasma Phys.* **40**, 39.
Foukal, P. V.: 1978, *Astrophys. J.* **223**, 1046.
Hood, A. W. and Priest, E. R.: 1979, *Astron. Astrophys.* **77**, 233.
Krieger, A. S., de Feiter, L.D., and Vaiana, G. S.: 1976, *Solar Phys.* **47**, 117.
Krishan, V.: 1983a, in *Proceedings of the Spring College on Radiation in Plasmas*, Trieste, Italy.
Krishan, V.: 1983b, *Solar Phys.* **88**, 155.
Krishan, V.: 1985, *Solar Phys.* **95**, 269.

Krishan, V., Berger, M. and Priest, E. R.: 1988, in R. C. Altrock (eds.), *Solar and Stellar Coronal Structures and Dynamics*, National Solar Observatory.

Krishan, V., Sreedharan, T. D., and Mahajan, S. M.: 1991, *Monthly Notices Roy. Astron. Soc.* **249**, 596.

Levine, R. H. and Altschuler, M. D.: 1974, *Solar Phys.* **36**, 345.

Levine, R. H. and Withbroe, G. L.: 1977, *Solar Phys.* **51**, 83.

Montgomery, D., Philips, L., and Theobald, M. L.: 1989, *Phys. Rev.* **A40**, 1515.

Montgomery, D., Turner, L. and Vahala, G.: 1978, *Phys. Fluids* **21**, 757.

Poletto, G., Vaiana, G. S., Zomback, M.V. Krieger, A. S., and Timothy, A. F.: 1975, *Solar Phys.* **44**, 83.

Priest, E. R.: 1978, Solar Phys. **58**, 57.

Priest, E. R.: 1981, in E. R. Priest (ed.), *Solar Flare Magnetohydrodynamics*, Gordon and Breach, New York, pp. 2 and 139.

Rosner, R., Tucker, W. H. and Vaiana, G. S.: 1978. *Astrophys. J.* **220**, 643.

Shan, X., Montgomery, D., and Chen, H.: 1991, *Phys. Rev.* **A44**, No. 10, 6800.

Theobald, M. L., Montgomery, D., Doolen, G.D., and Dahlburg, J. P.: 1989, *Phys. Fluids.* **B1**, 766.

Tsinganos, K. C.: 1982, *Astrophys. J.* **259**, 820.

Vaiana, G. S. and Rosner, R.: 1978, *Ann. Rev. Astrophys.* **16**, 393.

Yoshida, Z. and Giga, Y. M.: 1990, *Math. Z.* **204**, 235.

TEMPORAL BEHAVIOUR OF PRESSURE IN SOLAR CORONAL LOOPS

K. SASIDHARAN, T. D. SREEDHARAN,* R. PRATAP** and V. KRISHAN

Indian Institute of Astrophysics, Bangalore 560 034, India

Abstract. The temporal evolution of pressure in solar coronal loops is studied using the ideal theory of magnetohydrodynamic turbulence in cylindrical geometry. The velocity and the magnetic fields are expanded in terms of the Chandrasekhar–Kendall (C–K) functions. The three mode representation of the velocity and the magnetic fields submits to the investigation of chaos. When the initial values of the velocity and the magnetic field coefficients are very nearly equal ,the system shows periodicities. For randomly chosen initial value of these parameters the evolution of the velocity and the magnetic fields is nonlinear and chaotic. The consequent plasma pressure is determined in the linear and nonlinear regimes. The evidence for the existence of chaos is established by evaluating the invariant correlation dimension of the attractor-D_2, a fractal value of which indicates the existence of deterministic chaos.

1. Introduction

It is well known that loops are the dominant structures in the higher levels of the solar atmosphere. Even though our knowledge of loops has greatly enhanced in recent years as a result of observations in UV, EUV, and X-ray wavelengths (Foukal, 1978; Levine and Withbroe, 1977; Vaiana and Rosner, 1978), we have little empirical knowledge of the nature of the coronal magnetic field. Therefore a discussion of the relationship between coronal loops and coronal magnetic fields depend heavily on theoretical models.

Coronal loops exhibit a fairly stable and well-configured geometry in spite of the magnetic and velocity field fluctuations in the plasma. Such a steady state is the result of various manifestations of the balance of inertial and magnetic forces. Using statistical theory of incompressible magnetohydrodynamic turbulence discussed by Montgomery, Turner, and Vahala (1978), a steady-state model of active region coronal loops was discussed by Krishan (1983a, b), Krishan (1985), Krishan, Sreedharan, and Mahajan (1988) discussed the dynamics of velocity and magnetic fields in coronal loops. A Vlasov–Maxwell description of coronal loops deriving particle velocity distribution functions in an inhomogeneous plasma has been given by Krishan, Shreedharan, and Mahajan (1991).

Recently Sreedharan *et al.* (1992) have studied the steady state structure of the pressure in coronal loops, by representing the velocity and magnetic fields as

---

* Permanent address: Department of Physics, Mount Carmel College, Bangalore, 560 052, India.
** Cochin University of Science and Technology, Cochin, 682 022, India.

the superposition of three (C–K) functions. They discussed in detail the three-dimensional spatial variation (r, θ, z) of the plasma pressure in coronal loops.

In this paper we extend the results obtained by Sreedharan *et al.* (1992) to include the time dependence of velocity, magnetic field and pressure and study their evolution. Since the evolution equations are coupled and nonlinear, the dependence of their solutions on the initial conditions is expected to reveal chaotic behavior. Towards this end,we investigate in this paper the existence of chaos in the evolution of pressure in coronal loops by studying the power spectrum of the data generated by the solution of the MHD equations and by evaluating the invariant-dimension, especially the second order correlation dimension of the attractor D_2 of the system.

In the next section we derive the pressure profile for an incompressible fluid using MHD equations. In Section 3 we give a discussion of the various aspects of dynamics of the system by taking (i) the linear case, (ii) the pump approximation, and (iii) the full set of nonlinear coupled equations and the existence of deterministic chaos by evaluating the second-order correlation dimension which is an invariant parameter of the chaotic system. In this evaluation, we obtain the following informations: (a) Is there an attractor and if there exists one,is it regular or strange? (b) Is there only a single attractor or are there more than one? (c) What is the embedding dimension so that in describing nonlinear processes characterized by the set of given equations, what should be the dimensions of the phase space to describe the dynamics of the system. We follow the algorithm that has been proposed by Grassberger and Proccacia (1983). Section 4 deals with the discussion of results of the temporal variations and chaotic behavior of the pressure profile.

2. The Pressure Profile

The pressure profile for an incompressible fluid can be expressed as a function of velocity $\overline{V}$ and magnetic field $\overline{B}$ using MHD equations

$$\frac{\overline{\nabla}P}{\rho} = \frac{(\overline{\nabla} \times \overline{B}) \times \overline{B}}{\rho} - (\overline{V} \cdot \overline{\nabla})\overline{V} - \frac{\partial \overline{V}}{\partial t} , \tag{1a}$$

$$\overline{\nabla} \times (\overline{V} \times \overline{B}) - \frac{\partial \overline{B}}{\partial t} = 0 , \tag{1b}$$

$$\overline{\nabla} \cdot \overline{V} = 0 \quad \text{and} \quad P = nkT , \tag{1c}$$

where P is the mechanical pressure, n is the number density of particles, k is Boltzmann's constant, and T is the temperature. The loop plasma is represented by a cylindrical column of length L and radius R. ρ is the mass density and the force due to gravity is neglected. The set of Eequations (1a), (1b), and (1c) form a closed set of equations in the variables (V, B, ρ, and T).

Equation (1a) can be manipulated to yield

$$\overline{\nabla}\left(\frac{P}{\rho} + \frac{1}{2}V^2\right) = \left[\frac{(\overline{\nabla} \times \overline{B}) \times \overline{B}}{\rho} - (\overline{\nabla} \times \overline{V}) \times \overline{V}\right] - \frac{\partial \overline{V}}{\partial t} . \tag{2}$$

The velocity field $\overline{V}$ and magnetic field $\overline{B}$ can be represented as a superposition of the Chandrasekhar–Kendall functions following Montgomery, Turner, and Vahala (1978). In this study we consider a triple-mode system for the velocity $\overline{V}$ and magnetic field $\overline{B}$ written as

$$\overline{V} = \sum_{i=a,b,c,} \lambda_i \eta_i(t) \overline{A}_i , \tag{3}$$

$$\overline{B} = \sum_{i=a,b,c,} \lambda_i \xi_i(t) \overline{A}_i , \tag{4}$$

$$\overline{A}_{nm} = C_{nm} \overline{a}_{nm} r) , \tag{4a}$$

C_{nm} is the normalizing constant $\int \overline{A}_{nm}^* \cdot \overline{A}_{n,m} \, \mathrm{d}^3 r = \delta_{nn}, \delta_{mm}$, where

$$\overline{a}_{nm}(r) = \hat{e}_r \left[\frac{im}{r} + \frac{ik_n}{\lambda_{nm}}\frac{\partial}{\partial r}\right]\psi_{nm} = \hat{e}_\theta\left[\frac{\partial}{\partial r} - \frac{mk_n}{r\lambda_{nm}}\right]\psi_{nm} +$$

$$+\hat{e}_z\left[\frac{\lambda_{nm}^2 - k_n^2}{\lambda_{nm}}\right]\psi_{nm} , \tag{4b}$$

$$\psi_{nm} = J_m(\gamma_{nm}r)\exp(im\theta + ik_n z) ,$$

$$\lambda_{nm} = \pm(\gamma_{nm}^2 + k_n^2)^{1/2} , \qquad k_n = 2\pi n/L ,$$

$$n = 0, \mp 1, \mp 2, \dots , \qquad m = 0, \mp 1, \mp 2, \dots .$$

The functions $\overline{a}_{nm}$ satisfy $\overline{\nabla} \times \overline{a} = \lambda_{nm}\overline{a}_{nm} \cdot \gamma_{nm}$ can be determined from the boundary conditions (Sreedharan *et al.*, 1992). η_i and ξ_i are in general complex.

The dynamics can be described by taking the inner products of curl of Equations (1a) and 1(b) with $\overline{A}_{nm}^*$ and integrating over the volume. The resulting six complex, coupled, nonlinear ordinary differential equations are

$$\frac{\mathrm{d}\eta_a}{\mathrm{d}t} = \frac{\lambda_b\lambda_c}{\lambda_a}(\lambda_c - \lambda_b)I[\eta_b\eta_c - \xi_b\xi_c/\rho] , \tag{5}$$

$$\frac{\mathrm{d}\eta_b}{\mathrm{d}t} = \frac{\lambda_c\lambda_a}{\lambda_b}(\lambda_a - \lambda_c)I^*[\eta_c^*\eta_a - \xi_c^*\xi_a/\rho] , \tag{6}$$

$$\frac{\mathrm{d}\eta_c}{\mathrm{d}t} = \frac{\lambda_a\lambda_b}{\lambda_c}(\lambda_b - \lambda_a)I^*[\eta_a^*\eta_b^* - \xi_b^*\xi_a/\rho] , \tag{7}$$

$$\frac{d\xi_a}{dt} = \lambda_b - \lambda_c I [\eta_b \xi_c - \eta_c \xi_b] , \tag{8}$$

$$\frac{d\xi_b}{dt} = \lambda_c - \lambda_a I^* [\eta_c^* \xi_a - \eta_a \xi_c^*] , \tag{9}$$

$$\frac{d\xi_c}{dt} = \lambda_a - \lambda_b I^* [\eta_a^* \xi_b^* - \eta_b^* \xi_a] , \tag{10}$$

where $I = \int \overline{A}_a^* \cdot (\overline{A}_b \times \overline{A}_c) \, d^3 r$ and the (n, m) values of the modes (a, b, c) satisfy the condition $n_a = n_b + n_c$ and $m_a = m_b + m_c$. Equation (2) with the representation of $\overline{V}$ and $\overline{B}$ given in Equations (3) and (4) can be manipulated to yield

$$\overline{\nabla} \left(\frac{P}{\rho} + \frac{1}{2} \sum_{i=a,b,c} \sum_{j=a,b,c} \lambda_i \lambda_j \eta_i \eta_j \overline{A}_i \cdot \overline{A}_j \right) = \sum_{\substack{i=a,b,c \\ j=b,c,a}} (\lambda_- - \lambda_j) \times$$

$$\times \left(\frac{\xi_i \xi_j}{\rho} - \eta_i \eta_j \right) (\overline{A}_i \times \overline{A}_j) + \sum_{i=a,b,c} \frac{\partial \eta_i}{\partial t} \lambda_i \overline{A}_i . \tag{11}$$

The expansion coefficients η_i and ξ_i can be solved numerically from the dynamical equations (5)–(10) which when substituted in Equation (11) determine pressure as a function of space and time.

3. Dynamical Aspects

The temporal evolution of the pressure is presented for a cylindrical plasma column of length 'L' and radius 'R'. The ratio of the toroidal to poloidal magnetic flux, $\psi(t)/\psi(p)$ is taken as $\frac{1}{10}$. We have chosen the triads a, b, c to represent the largest possible spatial scales and also satisfy the condition $a = b + c$, as $a = (1, 1)$, $b = (1, 0)$, $c = (0, 1)$. Corresponding values of γ_i and λ_i are found to be $\gamma_a R = 3.23$, $\gamma_b R = 3.85$, $\gamma_c R = 3.85$, $\gamma_a R = 3.29$, $\lambda_b R = 3.90$, $\lambda_c R = 3.85$ for rigid boundary as described in Sreedharan et al. (1992). The total energy E of the loop plasma in a given configuration (a, b, c) is given by

$$E = 2 \sum_{i=a,b,c} \lambda_i (\eta_i^2 + \xi_i^2) .$$

There is no obvious way of fixing the relative magnitudes of the three modes even though we have some estimates of the total energy of a typical loop.

There are two physical situations under which Equations (5)–(10) can be solved analytically. (i) The linear case, (ii) the pump approximation.
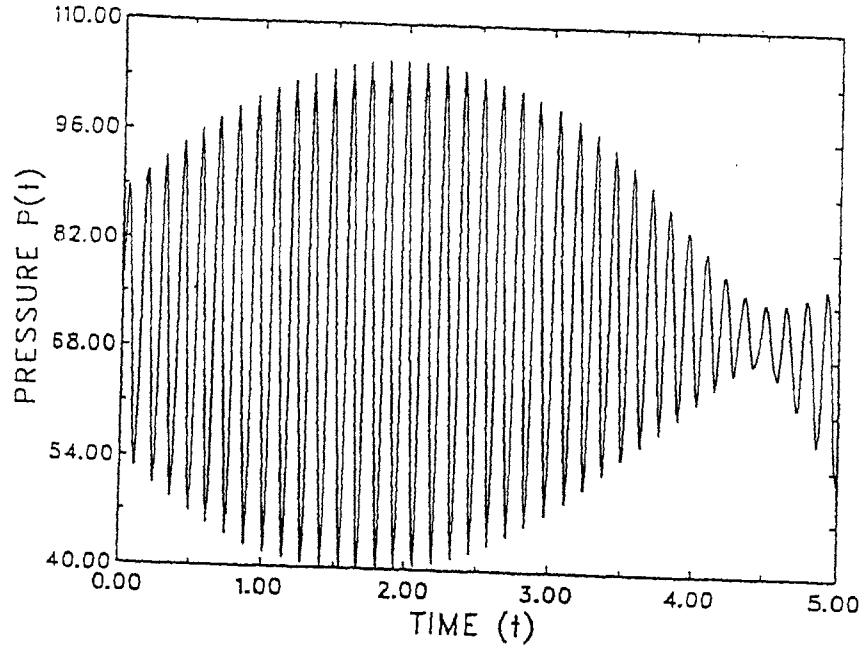
Fig. 1. Temporal evolution of pressure $[P(t)]$ at an axial point of the coronal loop when the initial values of the velocity and magnetic field coefficients are very nearly equal.

(i) THE LINEAR CASE

Here we study the time evolution of the small deviations of the velocity and magnetic fields from their equilibrium values, i.e., we assume $\eta = \eta_0 + \eta_1$, $\zeta = \zeta_0 + \zeta_1$ and that $\eta_0 = \zeta_0$ and $\eta_1 \approx \eta_0$, $\zeta_1 \approx \zeta_0$ for all modes. Assuming both $\eta_1(t)$ and $\zeta_1(t)$ have time dependence through e^{st}, we can obtain a dispersion relation whose solution is

$$s = \mp i\,|I|\,[\lambda_b^2(\lambda_b - \lambda_c - \lambda_a)^2\,|\eta_{b0}|^2 + \lambda_c^2(\lambda_c - \lambda_a - \lambda_b)^2\,|\eta_{c0}|^2 - \\ -\lambda_a^2(\lambda_a - \lambda_b - \lambda_c)^2\,|\eta_{a0}|^2]^{1/2}\,.$$

Thus the system exhibits marginal stability since the perturbed quantities have sinusoidal oscillations with a period which depends upon the equilibrium values of the fields.

Figure 1 shows time variation of pressure for the initial values of η_i as follows

$$|\eta_a| = 1.0\,, \qquad |\eta_b| = 2.0\,, \qquad |\eta_c| = 3.0\,,$$
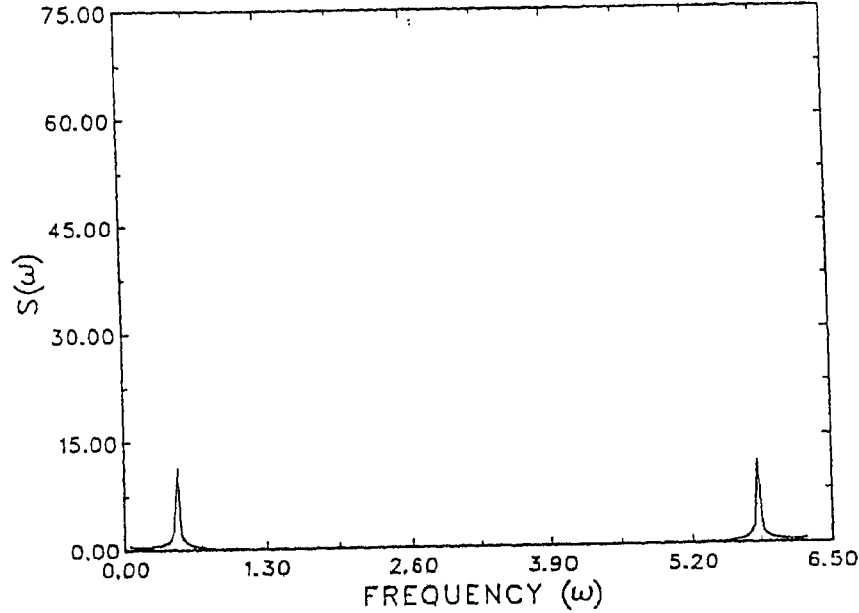
$$|\xi_a| = 1.1\,, \qquad |\xi_b| = 2.1\,, \qquad |\xi_c| = 3.1\,,$$

Fig. 2. The power spectrum $[S(\omega) - (\text{constant}) \lim_{T \to \infty} T^{-1} | \int_0^T e^{i\omega t} P(t) \, dt|^2]$ corresponding to the time variation of pressure shown in Figure 1.

The corres... ...nding power spectrum is shown in Figure 2. This discrete spectrum clearly indicates that the pressure profile has a finite number of frequencies when the magnitude of the velocity and magnetic fields are approximately equal initially. This marginal stability exists only for the time scales for which the linearisation is valid. The Skylab, UV and microwave observations do indicate that the loops are in a state of quasi periodic pulsations (Aschwanden, 1987).

(ii) THE PUMP APPROXIMATION

In the pump approximation one of the three modes is taken to be the strongest. For example here since the conservation condition gives $a = b + c$, we can take 'a' to be the dominant mode and call it the pump which shares its energy with the other two modes. The time evolution of the two modes does not produce any significant change in the pump mode and hence we can neglect all time variations in (η_a, ξ_a). The system of six equations ((5)–(10)) therefore reduces to four (Equations (5) and (8) are automatically satisfied under the pump approximation since both sides of the equations are vanishingly small) with the additional assumption $\eta_a = \xi_a$ and takes the following simplified form which can be solved analytically

$$\frac{d\eta_b}{dt} = \frac{\lambda_c \lambda_a}{\lambda_b} (\lambda_a - \lambda_c) I^* [\eta_c^* - \xi_c^*] \eta_a \,, \tag{12}$$

$$\frac{d\eta_c}{dt} = \frac{\lambda_a \lambda_b}{\lambda_c}(\lambda_b - \lambda_a)I^*[\eta_b^* - \xi_b^*]\eta_a \;, \tag{13}$$

$$\frac{d\xi_b}{dt} = \lambda_a \lambda_c I^*[\eta_c^* - \xi_c^*]\eta_a \;, \tag{14}$$

$$\frac{d\xi_c}{dt} = \lambda_a \lambda_c I^*[\xi_b^* - \eta_b^*]\eta_a \;. \tag{15}$$

Complex conjugates of Equation (13) and (15) gives

$$\frac{d\eta_c^*}{dt} = \frac{\lambda_a \lambda_b}{\lambda_c}(\lambda_b - \lambda_a)I[\eta_b - \xi_b]\eta_a^* \;, \tag{16}$$

$$\frac{d\xi_c^*}{dt} = \lambda_a \lambda_b I[\xi_b - \eta_b]\eta_a^* \tag{17}$$

and the difference of Equations (16) and (17) gives

$$\frac{d\eta_c^*}{dt} - \frac{d\xi_c^*}{dt} = \frac{\lambda_a \lambda_b}{\lambda_c} I\eta_a^*[\lambda_b - \lambda_a + \lambda_c]\,(\eta_b - \xi_b) \;. \tag{18}$$

A time derivation of Equation (12) can be written as

$$\frac{d^2\eta_b}{dt^2} = \lambda_a^2 |I|^2 |\eta_a|^2 (\lambda_a - \lambda_c)(\lambda_b - \lambda_a + \lambda_c)(\eta_b - \xi_b) \;. \tag{19}$$

We have used Equation (18) in writing (19). In a similar manner we can write the equation for $d^2\eta_c/dt^2$.

One can therefore write these equations as

$$\frac{d^2\eta_b}{dt^2} = P_1 \eta_b + P_2 \;, \tag{20}$$

$$\frac{d^2\eta_c}{dt^2} = P_1' \eta_c + P_2' \;, \tag{21}$$

where

$$\xi_b = \frac{\lambda_b}{\lambda_a - \lambda_c}(\eta_b - O_b) \;, \qquad I_b = \eta_{b0} - \frac{(\lambda_a - \lambda_c)}{\lambda_b}\xi_{b0} \;,$$

$$\xi_c = \frac{\lambda_c}{(\lambda_a - \lambda_b)}(\eta_c - I_c) \;, \qquad I_c = \eta_{c0} + \frac{(\lambda_b - \lambda_a)}{\lambda_c}\xi_{c0} \;,$$

$$P_1 = \lambda_a^2(\lambda_a - \lambda_b - \lambda_c)^2 |I|^2 |\eta_a|^2 \;,$$

$$P_2 = \lambda_a^2 \lambda_b(\lambda_a - \lambda_b - \lambda_c)|I|^2 |\eta_a|^2 I_b \;,$$

$$P_1' = P_1 \,,$$

$$P_2' = \lambda_a^2 \lambda_c (\lambda_a - \lambda_b - \lambda_c) |I|^1 |\eta_a|^2 I_c \,.$$

Integrating Equations (20) and (21) we get

$$\eta_b = A \, e^{\sqrt{p_1}t} + B \, e^{\sqrt{p_1}t} - \frac{p_2}{p_1} \,, \qquad C^{-\sqrt{P_1}\,t}$$

$$\eta_c = Q \, e^{\sqrt{p_1}t} + R \, e^{\sqrt{p_1}t} - \frac{p_2'}{p_1} \,, \qquad C^{-\sqrt{P_1}\,t}$$

where A, B, Q, R are to be determined by the initial conditions. This shows that all the four field coefficients, η_b, ξ_b, η_c, ξ_c, exhibit growing and decaying modes. This is understandable since there is an infinite capacity pump mode η_a, ξ_a in the system at the expense of which η_b, ξ_b, η_c, ξ_c are growing. Thus in the case of pump approximation analytical solutions to the system can be found.

(iii)CHAOS IN THE SYSTEM

Equations (5)–(10) are a set of six ordinary first-order differential equations which are highly nonlinear. It may further be realized that the velocity (η_i) and magnetic field (ξ_i) components are both coupled which adds to the inherent nonlinearity of the equations of motion – characteristic of MHD equations. These equations in principle can be seen as equivalent to one ordinary sixth order differential equation which will manifest all the nonlinearities and therefore may lead to chaotic dynamics. To investigate this aspect we first determine the power spectrum of the system.A broad band power spectrum is a sure indication of the existence of chaos in the dynamics. An insight into chaotic system can be obtained by determining the invariant parameters such as correlation dimensions D_i, Kolmogorov entropies K_i, Lyapunov exponents etc which are all infinite in number. However it has been shown that of the infinite number of the correlation dimensions and Kolmogorov information entropies, the second-order quantities are the most significant ones and hence we shall determine D_2 in the present analysis. We shall postpone the determination of K_i and Lyapunov exponents for a later occasion. We follow in this the algorithm which was first proposed by Grassberger and Proccacia (1983) and later developed by Atmanspacher and Schinegraber (1986) and Abraham *et al.* (1986).

Let $\{X_0(t)\}$ be the original time series with the data being taken at constant interval. These data set can be rearranged so as to get $(d - 1)$ additional data sets as

$$X_0(t_1), \ldots, X_0(t_N) \,,$$

$$X_0(t_1 + \Delta t), \ldots, X_0(t_N + \Delta t) \,,$$

$$X_0(t_1 + d\Delta t), \ldots, n\, X_0(t_N + d\Delta t) ,$$

we can consider the transpose of the above matrix as consisting of N vectors having d components in a d dimensional space. The general vector can be written as

$$\overline{X}_i = (X_0(t_1), \ldots, X_0(t_i + d\Delta t)) ,$$

where $i = 1, \ldots, N$ and $\overline{X}_i$ is a point in the constructed d-dimensional space. We now evaluate the correlation function

$$C_d(r) = \lim_{N \to \infty} \frac{1}{N^2} \sum_{i,j=1,N} \theta(r - |\overline{X}_i - \overline{X}_j|) ,$$

where θ is the Heaviside function defined as $\theta(x) = 0$ for $x < 0$ and unity for $x > 0$. This implies that if the absolute value of the vector difference $|\overline{X}_i - \overline{X}_j|$ is less than r, we count it as unity and is zero if it is greater than r. We then construct the small boxes of side r in the phase space and count the vector tips that lie in this box. This counting. It is shown that as r becomes smaller $C_d(r) \sim r^\nu$ so that

$$\log C_d(r) \sim \nu \log r .$$

As $r \to 0$ and $d \to \infty$, ν takes a definite value which is called the second-order correlation dimension and we get

$$D_2 = \lim_{\substack{r \to 0 \\ d \to \infty}} \frac{\log C_d(r)}{\log(r)} .$$

The correlation integral $C(r)$ has to be calculated for several values of r with respect to each particular dimension d of the constructed phase space. For each dimension d one obtains $\log C_d(r)$ vs $\log(r)$ curve and the slope ν of the linear part of the curve can be obtained using least-ssquare fit. If the slope ν converges towards a finite value for higher values of d, this value is denoted by D_2. When D_2 is an integer, the system is regular and when it is a fractal the system is chaotic.

We have numerically solved Equations (5)–(10) for arbitrary initial values of the field coefficients. The time evolution of pressure at an axial point of the loop for initial values ($|\eta_a| = 4.0$, $|\eta_b| = 7.0$, $|\eta_c| = 10.0$, $|\xi_a| = 8.0|$, $|\xi_b| = 11.0$, $|\xi_c| = 14.0$) is shown in Figure 3. The time variation is highly complex. The corresponding power spectrum is shown in Figure 4. The spectrum is fluctuating and broad band indicating the presence of chaos. A data set of 500 points corresponding to this chaotic evolution of pressure is used to evaluate the information dimension- D_2-by the method described above. In Figure 5, we illustrate the converging slope and the value of D_2 is found to be 1.732. With the same initial conditions D_2 was evaluated at a surface point and the slope does not seem to converge to a limiting value. This is shown in Figure 6. The fractal value of D_2 evidences the existence
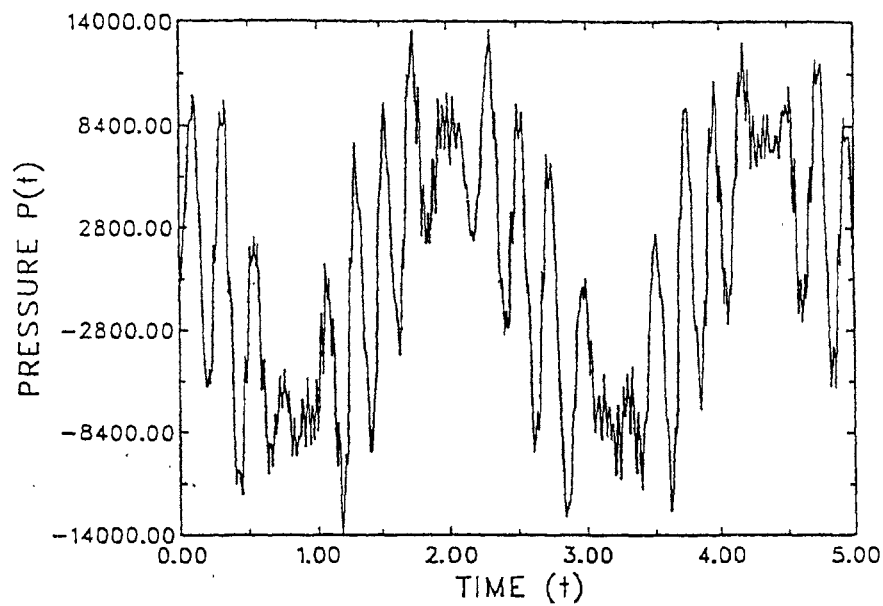
Fig. 3. Time variation of pressure at an axial point of the loop when the initial values of the field coefficients η_a, η_b, η_c are much different from those of ξ_a, ξ_b, ξ_c, respectively.
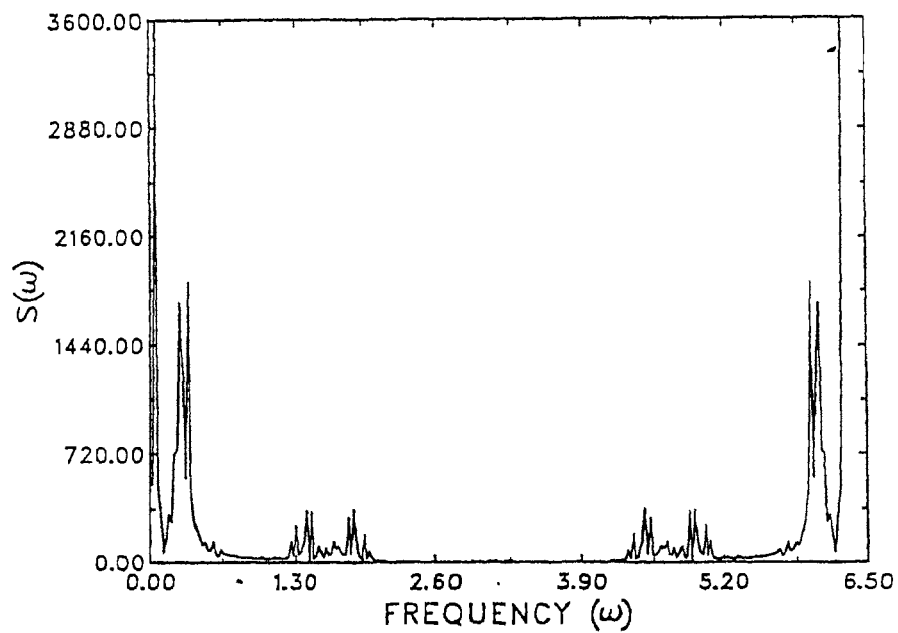

Fig. 4. Power spectrum $[S(\omega)]$ corresponding to the time variation of pressure shown in Figure 3.

of deterministic chaos. In a chaotic regime the system can either dissipate to an attractor stage or can follow a stochastic (random) flow. As the dimension d of the constructed phase space increases the slope ν may converge to a limiting value. In this case the flow will be confined to a geometrical object called attractor. The converging value of the slope is the dimension D_2 of the attractor. The dimension of the attractor measures the minimum number of independent parameters needed to describe the system dynamics. In other words if D_2 exists, there is a properly defined dynamical system. The steady increase of slope ν with d (Figure 6) evidently shows that it cannot converge and consequently the number of degrees of freedom of the system is increasing. Then the complexity of the system increases and it tends to a more disordered state indicating that system behavior is stochastic.

4. Conclusion

In the equilibrium state $\eta_a = \xi_a$, $\eta_b = \xi_b$, $\eta_c = \xi_c$. We disturb the system slightly from the equilibrium state and study the time evolution for small departure from equilibrium. In this case the system is shown to exhibit sinusoidal oscillation with a period which depends upon the initial values of the field coefficients. In other words, when the system is perturbed from a state where the magnetic energy $B^2/4\pi$ and the kinetic energy $(\frac{1}{2})mv^2$ are nearly equal, it exhibits marginal stability. The microwave and X-ray observations of coronal loops show quasi-periodic oscillations with time scales ranging from a fraction of a second to tens of minutes (Aschwanden, 1987; Švestka, 1994, and references therein). These oscillations are usually interpreted in terms of magnetohydrodynamic waves in loop plasma (Roberts, Edwin, and Benz, 1984). The observed power spectrum of pulsations actually exhibits a more complex behaviour (e.g., Figure 1(d) of Švestka, 1994) which appears quasi-periodic only if we ignore finer variations. Thus quasi-periodic behaviour is expected only near equilibrium as is shown in our studies and the linear wave analysis studies. Under large departures from the equilibrium, a loop will show a complex temporal structure which can only be described in terms of objects with fractal dimensions in the phase space of the velocity and magnetic field. Coronal loops being continuously subjected to external forcing through their foot points and through their interaction with neighbouring regions are most likely to be in a chaotic state of pressure fluctuations. Therefore, when there are large deviations from equilibrium, i.e., for initial values of η_a, η_b, η_c, much different from those of ξ_a, ξ_b, ξ_c, respectively, the system is nonlinear and so is corresponding time evolution of the pressure. In this case each individual mode becomes distinct, stronger and mode-mode interaction can take place. In the pump approximation case since the variation of the strongest mode is negligible when compared with other modes, the interaction is between less number of modes of oscillations and the system showed oscillatory behavior,whereas the chaotic behaviour is caused by the superposition of more than two modes of oscillation and due to strong
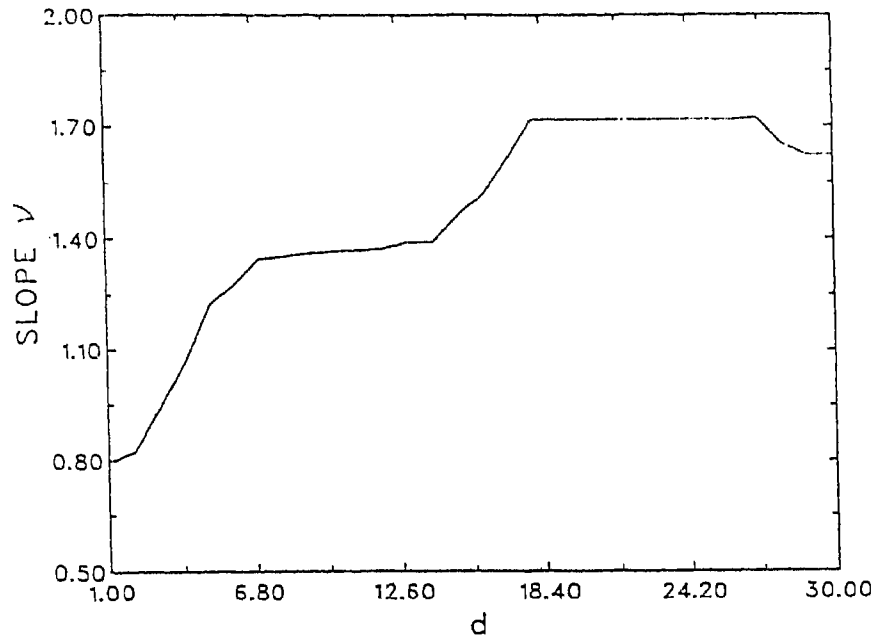
Fig. 5. The slopes (ν) of the linear part of the log $C_d(r)$ vs log(r) curves,obtained using least-squares fits are plotted against the dimension d of the constructed phase space. The two asymptotic values of the slopes are 1.39 and 1.73. This is corresponding to the chaotic evolution of pressure at an axial point of the loop.

nonlinear coupling between them as is indicated in the nonlinear case above. This fact is evident in the evaluation of D_2. Figure 5 shows the determination of D_2 at an axial point. It is interesting to note that we get two asymptotic values one at 1.39 and the other at 1.73. It could be interpreted as the existence of two strange attractors with embedding space of dimension 7 and 18 and the trajectory can land up on either of these attractors. The fact that these are strange attractors (because of fractal dimension) the trajectories could jump from one to the other. This clearly shows the complexity of the situation. The curve of slope ν vs dimension d at $r = R$ does not show any saturation and that the curve is more or less centered on the 45° line showing the presence of randomness or white noise as shown in Figure 6. Thus as we proceed from the axis towards the surface the dynamics show the development of strange attractors ending up in complete randomness.

In Figures 5 and 6 even though the initial values of ξ_s and η_s are the same,those of pressure P at $(r = 0, t = 0)$ and at $(r = R, t = 0)$ are not same. This difference in Figures 5 and 6 is due to the different initial values of pressure at axial and surface points. The transition from a strange attractor state to randomness requires a much finer analysis which will be investigated on a future occasion. In conclusion the time scale over which the system is stable or otherwise can be inferred only by evaluating the Lyapunov constants which are sensitive to the initial conditions.
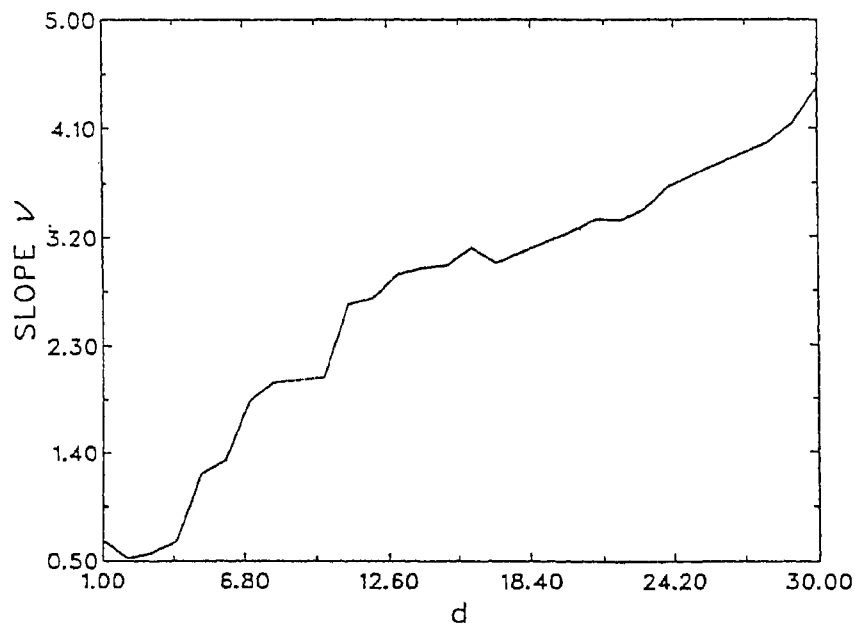
Fig. 6. Corresponding to the chaotic time evolution of pressure at a surface point of the loop, the slopes (ν) of the linear part of the $\log C_d(r)$ vs $\log(r)$ curves are plotted against the dimension d. The slopes do not converge to any limiting values.

Inverting the problem, by specifying the Lyapunov constants, one can possibly evaluate the class of initial states which can give the observed life time of the loops.

References

Abraham, N. B. *et al.*: 1986, *Phys. Letters* A114, 217.
Aschwanden, M. J.: 1987, *Solar Phys.* 111, 113.
Atmanspacher, H. and Scheingraber, H.: 1986, *Phys. Rev.* A34, 253.
Foukal, P. V.: 1978, *Astrophys. J.* 223, 1046.
Grassberger, P. and Procaccia, I.: 1983, *Phys. Rev. Letters* 50, 346.
Krishan, V.: 1983a, *Proceedings of the Spring College on Radiation in Plasmas*, Trieste, Italy.
Krishan, V.: 1983b, *Solar Phys.* 88, 155.
Krishan, V.: 1985, *Solar Phys.* 95, 269.
Krishan, V., Berger, M., and Priest, E. R.: 1988, in R. C. Altrock (ed.), *Solar and Stellar Coronal Structures and Dynamics*, National Solar Observatory.
Krishan, V., Sreedharan, T. D., and Mahajan, M.: 1991, *Monthly Notices Roy. Astron. Soc.* 249, 596.
Levine, R. H. and Withbroe, G. L.: 1977, *Solar Phys.* 51, 83.
Montgomery, D., Turner, L., and Vahala, G.: 1978, *Phys. Fluids* 21, 757.
Roberts, B., Edwin, P. M., and Benz, A. O.: 1984, *Astrophys. J.* 279, 857.
Sreedharan, T. D., Sasidharan, K., Satyanarayanan, A., and Krishan, V.: 1992, *Solar Phys.* 142, 249.
Švestka, Z.: 1994, *Solar Phys.* 152, 505.
Vaiana, G. S. and Rosner, R.: 1978, *Ann. Rev. Astrophys.* 16, 393.